Article

Spatial dynamics of brain development and neuroinflammation

https://doi.org/10.1038/s41586-025-09663-y

Received: 27 July 2024

Accepted: 22 September 2025

Published online: 5 November 2025

Open access

Check for updates

Di Zhang[1,16], Leslie A. Rubio Rodríguez-Kirby[2,16], Yingxin Lin[3], Wenqi Wang[2], Mengyi Song[4,5], Li Wang[4,5], Lijun Wang[3], Shigeaki Kanatani[2], Tony Jimenez-Beristain[2], Yonglong Dang[2], Mei Zhong[1,6,7], Petra Kukanja[2], Shuozhen Bao[1], Shaohui Wang[4,5], Xinyi Lisa Chen[3], Fu Gao[1,8], Dejiang Wang[8,9], Hang Xu[10,11], Cong Ma[12], Xing Lou[1], Yang Liu[8,9], Jinmiao Chen[10,11], Nenad Sestan[13], Per Uhlén[2], Arnold Kriegstein[4,5], Hongyu Zhao[3,14], Gonçalo Castelo-Branco[2] ✉ & Rong Fan[1,6,8,15] ✉

The ability to spatially map multiple layers of omics information across developmental timepoints enables exploration of the mechanisms driving brain development[1], differentiation, arealization and disease-related alterations. Here we used spatial tri-omic sequencing, including spatial ATAC–RNA–protein sequencing and spatial CUT&Tag–RNA–protein sequencing, alongside multiplexed immunofluorescence imaging (co-detection by indexinng (CODEX)) to map dynamic spatial remodelling during brain development and neuroinflammation. We generated a spatiotemporal tri-omic atlas of the mouse brain from postnatal day 0 (P0) to P21 and compared corresponding regions with the human developing brain. In the cortex, we identified temporal persistence and spatial spreading of chromatin accessibility for a subset of layer-defining transcription factors. In the corpus callosum, we observed dynamic chromatin priming of myelin genes across subregions and identified a role for layer-specific projection neurons in coordinating axonogenesis and myelination. In a lysolecithin neuroinflammation mouse model, we detected molecular programs shared with developmental processes. Microglia exhibited both conserved and distinct programs for inflammation and resolution, with transient activation observed not only at the lesion core but also at distal locations. Overall, this study reveals common and differential mechanisms underlying brain development and neuroinflammation, providing a rich resource for investigating brain development, function and disease.

Development and neuroinflammation in the mammalian brain are meticulously regulated; for example, mouse corticogenesis proceeds through an inside-out mechanism. Cells of the deeper cortical layers V and VI, such as corticothalamic projection neurons (PNs; layer VI CThPNs, embryonic day 12.5 (E12.5)), subcerebral projection neurons (layer V SCPNs, E13.5) and some callosal PNs (CPNs; E12.5–13.5) that populate deeper layers are defined earlier than those that populate the outer layers (IV and II/III), including granular (spiny stellate) neurons (E14.5) in layer IV and CPNs (E15.5) in layer II/III[2,3]. Oligodendrocyte and astrocyte genesis occurs simultaneously, populating the cerebral cortex (CTX) and the underlying corpus callosum (CC)[4,5]. Neurodegeneration reactivates many of the developmental programs.

In recent years, disease-associated glial states have been a primary focus, driven by large-scale sequencing strategies to delineate cell states by examining RNA, protein expression and chromatin accessibility[6–13]. Spatial omics analyses offer an important view of the molecular architecture of biological systems. One spatial proteomics approach, CODEX, provides single-cell-resolution cell type and morphological information[14]. We developed a platform, deterministic barcoding in tissue (DBiT), that enables spatial co-profiling of transcriptome and epigenome[1], as well as transcriptome and proteome[15]. Extending this approach to spatially map the epigenome, transcriptome and proteome within the same tissue section would enable a comprehensive investigation of the molecular mechanisms across all layers of the central dogma[16]. Here, we developed and applied DBiT-based spatial tri-omic technologies, including spatial assay for transposase-accessible chromatin (ATAC)–RNA–protein-seq (spatial ARP-seq) and CUT&Tag–RNA–protein-seq (spatial CTRP-seq), to simultaneous profile genome-wide

[1]Department of Biomedical Engineering, Yale University, New Haven, CT, USA. [2]Laboratory of Molecular Neurobiology, Department of Medical Biochemistry and Biophysics, Karolinska Institutet, Stockholm, Sweden. [3]Department of Biostatistics, Yale School of Public Health, New Haven, CT, USA. [4]The Eli and Edythe Broad Center of Regeneration Medicine and Stem Cell Research, University of California San Francisco, San Francisco, CA, USA. [5]Department of Neurology, University of California San Francisco, San Francisco, CA, USA. [6]Yale Stem Cell Center, Yale School of Medicine, New Haven, CT, USA. [7]Department of Cell Biology, Yale University School of Medicine, New Haven, CT, USA. [8]Department of Pathology, Yale University School of Medicine, New Haven, CT, USA. [9]Department of Neurology, Yale School of Medicine, New Haven, CT, USA. [10]Institute of Molecular and Cell Biology (IMCB), Agency for Science, Technology and Research (A*STAR), Singapore, Singapore. [11]Binformatics Institute (BII), Agency for Science, Technology and Research (A*STAR), Singapore, Singapore. [12]Gilbert S. Omenn Department of Computational Medicine & Bioinformatics, University of Michigan, Ann Arbor, MI, USA. [13]Department of Neuroscience, Yale School of Medicine, Yale University, New Haven, CT, USA. [14]Program of Computational Biology and Bioinformatics, Yale University, New Haven, CT, USA. [15]Human Center for Research on Aging (Yale-Age), Yale School of Medicine, New Haven, CT, USA. [16]These authors contributed equally: Di Zhang, Leslie A. Rubio Rodríguez-Kirby. ✉e-mail: goncalo.castelo-branco@ki.se; rong.fan@yale.edu

chromatin accessibility or histone modifications (H3K27me3), the whole transcriptome and the proteome (around 150 proteins) within the same tissue section at the cellular level. To elucidate the cellular and molecular processes during brain development and neuroinflammation, we applied these technologies to mouse brains from newborn to juvenile stages (benchmarking to the developing human brain), and to a focal demyelination mouse model induced by lysolecithin (LPC) (Fig. 1a, Supplementary Fig. 1a,b and Supplementary Tables 7–9; online resource: https://spatial-omics.yale.edu/).

Multiplex CODEX imaging of the developing brain

We designed a 23-plex CODEX antibody panel for mouse (Fig. 1a) and a 19-plex panel for human (Supplementary Fig. 1c), including markers for major cell types in brain development and neuroinflammation. We imaged the mouse brain coronal sections (0.5 mm relative to bregma for P21, and closely analogous positions for P0–10), and the human brain primary visual (V1) cortical regions[17] at the second trimester (estimated 154 days after conception), third trimester (224 days after conception) and at infancy (year 0–1, 507 days after conception). Segmentation, Seurat clustering and cell typing of the CODEX data revealed the arealization of the mouse brain with expected marker distribution, specificity and morphology (Fig. 1b,c, Extended Data Fig. 1 and Supplementary Figs. 2–9 and 11–13).

The ramified astrocytic/neural progenitor marker GFAP was expressed in the mouse glial limitans and medial ventricular zones at P0, and began to expand at P5 to specific areas in the parenchyma and CC, a region where it was particularly abundant at P21 (Fig. 1b and Supplementary Figs. 2–7). We found Ki-67$^+$ proliferating cells densely concentrated in the ventricular region, where neuroblasts, precursor cells and glia reside[18,19]. The Ki-67$^+$ periventricular and white-matter (WM) density contracted during later development, as progenitor cells became terminally differentiated (Fig. 1b, Extended Data Fig. 1 and Supplementary Figs. 2–9).

Neuronal markers populated mostly the grey matter regions. Each marker showed cortical layer specificity with CUX1/2 (layers II/III/IV) in the upper layers and TBR1 (IV/V/VI) and CTIP2 (V/VI and striatum) in deeper cortical layers (Figs. 1b and 2a,b, Extended Data Fig. 1 and Supplementary Figs. 2–7). While these layer-defining transcription factors (TFs) (CUX1/2, CTIP2 and SATB2) were expressed at P21, their protein expression and the density of cells expressing these markers was reduced compared with at early postnatal stages (Figs. 1b and 2a,b and Supplementary Figs. 2–7 and 10), consistent with the Allen Brain Atlas profiling[20] (Supplementary Fig. 10).

OLIG2, a pan oligodendrocyte marker was expressed in cells mainly in the CC but also throughout the brain (Figs. 1b and 3a,b and Supplementary Figs. 2–9). We found MBP and MOG (markers of mature oligodendrocytes, MOLs) were absent between P0 and P5, with expression starting at P7 and P10, respectively, as previously reported[4] (Figs. 1b and 3a and Supplementary Figs. 2–9). Notably, the expression of MBP and MOG was initially limited to the lateral part of the CC (P7–10), beneath the primary somatosensory area and only spread throughout the entire CC at P21, suggesting a lateral-to-medial progression of myelination. Myelin in the CTX was also identified at P21 (Figs. 1b and 3a and Supplementary Fig. 8).

We included markers for immune cells: granulocytes/neutrophils (Ly6G$^+$), monocytes/macrophages (IBA1$^+$, CD11b$^+$, CD169$^+$), dendritic cells (CD11c$^+$, MHC class II$^+$), T cells (CD3$^+$, CD4$^+$C, CD8$^+$) and B cells (CD19$^+$, CD45R$^+$) (Fig. 1a). As expected, most of the immune subtypes were sparse and primarily localized to the meningeal compartment. However, CD169 was abundant in the meninges and present in the choroid plexus, identifying a developmental border-associated macrophage counterpart to central nervous system (CNS)-resident CD169$^+$ cells that increase after ischaemia[21,22] (Fig. 1b and Supplementary Figs. 2–7).

Imaging with the human CODEX panel revealed distinct arealization (Fig. 1c and Supplementary Fig. 1c). Although SATB2, CTIP2 and TBR1 protein levels appeared to be reduced in infancy compared with at earlier stages, adjusting for cellular density indicates a domain expansion aligning with increased brain volume during development (Supplementary Figs. 11–14). Myelination marked by MOG expression intensified during infancy, consistent with previous reports[23] (Fig. 1c and Supplementary Figs. 12 and 13). Overall, our CODEX profiling provides a comprehensive single-cell protein benchmark and spatial cell typing across mouse and human brain development.

DBiT-based spatial tri-omics profiling

To further investigate the molecular mechanisms across all levels of the central dogma, we developed an all-encompassing spatial assay for co-profiling of the epigenome, transcriptome and a large protein panel simultaneously within the same tissue section—spatial ARP-seq (Fig. 1a and Supplementary Fig. 1a). A frozen tissue section was fixed with formaldehyde, incubated with a cocktail of antibody-derived DNA tags (ADTs) for mouse (Supplementary Table 4) or human (Supplementary Table 5), and treated with Tn5 transposase loaded with a universal ligation linker to insert the adapter at transposase accessible genomic loci. The tissue was then incubated with a biotinylated poly(T) adapter to bind to the poly(A) tail of mRNAs and ADTs for in-tissue reverse transcription. Next, two microfluidic channel array chips with perpendicular channels were applied to introduce spatial barcodes A_i (i = 1–100 or 220) and B_j (j = 1–100 or 220) into the tissue, forming a 2D grid of spatially barcoded tissue pixels. Each pixel, defined by a unique combination of A_i and B_j barcodes, measured 20 μm (100 barcodes; data S1) or 15 μm (220 barcodes; data S2), resulting in a total of 10,000 or 48,400 barcoded pixels. After releasing the barcoded cDNAs (from both mRNAs and ADTs) and genomic DNA (gDNA) fragments, separate libraries for gDNA and cDNA were constructed for next-generation sequencing (Supplementary Fig. 1a). We also developed spatial tri-omic profiling method that simultaneously measures genome-wide histone modifications, the transcriptome and proteins—termed spatial CTRP-seq. The procedure followed a workflow similar to that described above, except that an antibody against H3K27me3 was applied to the tissue section, followed by a protein-A-tethered Tn5–DNA complex to perform cleavage under targets and tagmentation (CUT&Tag)[24,25] (Fig. 1a and Supplementary Fig. 1b; details of quality control and metrics are provided in the Methods).

Spatial deconvolution of the brain around birth

To investigate the spatial molecular dynamics of mammalian cortical and WM development, we used spatial ARP-seq on tissue sections that were either adjacent to or from regions anatomically matched to those processed with CODEX. We clustered RNA and ATAC data from postnatal mouse brains separately, integrating across all timepoints with the same pixel size (Supplementary Table 7). For the coronal mouse brains from P0–21 processed with spatial ARP-seq (replicate S1), we identified 22 major RNA (R0–21) and 15 major ATAC clusters (A0–14) (Fig. 1e–h). We further integrated our RNA and ATAC data using SpatialGlue, leading to 18 refined spatial domains (D1–18) (Fig. 1i and Supplementary Fig. 18a,b). The spatial distribution of these domains aligned with tissue histology from the Allen Brain Atlas[20] and provided better arealization when compared to CODEX (Fig. 1b, Extended Data Fig. 1 and Supplementary Figs. 2–7), with the division of cortical layers II/III and V, subdivision between primary and secondary motor cortical areas and eventually the anterior cingulate at each layer. Medial D4 and D14 clusters segregated from clusters D9 (layer II/III) and D2 (layer V), respectively (Fig. 1i). Similar spatial domains were observed in the replicate (S2) (Extended Data Fig. 2a–e).

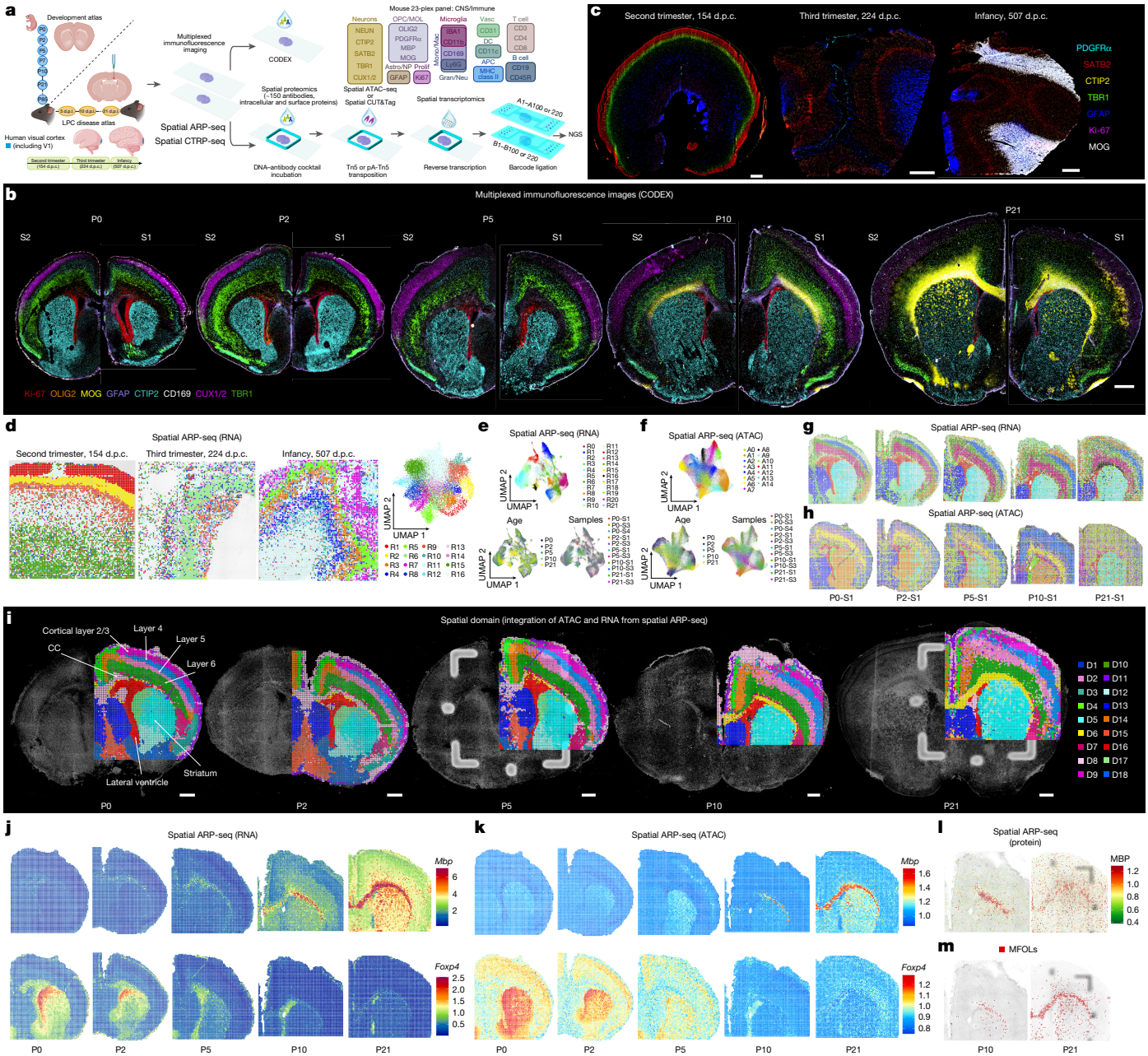

Fig. 1 | Spatial tri-omics mapping of the developing mouse and human brains at the onset of myelination. a, Schematic of the workflow. Some elements of the diagram were generated using BioRender and adapted from ref. 1, Springer Nature Limited, under a Creative Commons Attribution 4.0 licence. APC, antigen-presenting cells; astro, astrocytes; Gran/Neu, granulocytes and neutrophils; Mono/mac, monocytes and macrophages; NP, neural progenitors; prolif, proliferating cells; vasc, vasculature. **b**, CODEX images of the mouse brain coronal sections from P0 to P21 with two replicates (S1 and S2). Scale bar, 500 µm. **c**, CODEX images of the human brain V1 region at the second trimester (154 days after conception (d.p.c.)), the third trimester (224 days after conception) and infancy (507 days after conception). Scale bars, 1 mm. **d**, Uniform manifold approximation and projection (UMAP) and spatial distribution of spatial RNA clusters of the human brain samples at different stages. **e**, UMAPs of the mouse brain spatial RNA clusters at different ages from P0 to P21, with sample information. **f**, UMAPs of the mouse brain spatial ATAC clusters at different ages from P0 to P21, with sample information. **g**, The spatial distribution of RNA clusters in **e**. **h**, The spatial distribution of ATAC clusters in **g**. **i**, The spatial domain of the mouse brains generated by the integration of RNA and ATAC data in spatial ARP-seq (S1). Scale bars, 500 µm. **j**,**k**, Spatial mapping of gene expression (**j**) and the GAS (**k**) of *Mbp* and *Foxp4* for RNA and ATAC in spatial ARP-seq. **l**, MBP expression from ADT protein data in spatial ARP-seq (S1). **m**, Label transfer of MFOLs from scRNA-seq[28–30] to P10 and P21 mouse brains.

Consistent with CODEX, chromatin accessibility and RNA expression of *Mbp* and *Mog* in the CC were not present at P0–5 but were rather induced at P7–10 (Fig. 1j,k, Extended Data Fig. 2f,g and Supplementary Fig. 18c–e). Moreover, spatial ARP-seq data revealed that MBP and MOG proteins arose also at later stages (Fig. 1l and Extended Data Fig. 3c). While the striatum was characterized by markers of medium spiny neurons such as *Bcl11b* (clusters D5, D12 and D17) (Fig. 1i and Supplementary Fig. 19), the expression and ATAC gene activity score (GAS) of *Foxp4*, a TF that is known to regulate morphogenesis, disappeared gradually, while *Foxp1* and *Foxp2* retained dominance in the postnatal striatum, consistent with previous studies[24–27] (Fig. 1j,k, Extended Data Fig. 2f,g and Supplementary Fig. 18c–e). Spiked-in spatial ARP-seq TF ADTs also showed general concordance in the positional signal for CTIP2, CUX1/2, NEUN, SATB2 and TBR1 as compared to RNA expression, ATAC

GAS and the CODEX imaging at P0 (Extended Data Fig. 5). Most of the antibodies in the ADT panel target immune proteins that were not detectable during development. Nevertheless, we were able to detect markers for monocytes, macrophages and microglia (CD11b, CD68 and CD86), dendritic cells (CD11c) and natural killer cells (CD49b) at P0 (Extended Data Fig. 5a).

After mapping cell states defined by previous scRNA-seq studies[28–30] to our RNA data (Extended Data Figs. 3a and 4), we identified that the cluster localized to the CC corresponds to myelin-forming oligodendrocytes (MFOLs) (Fig. 1m and Extended Data Fig. 3b) and is represented only in the P10 and P21 samples, consistent with our CODEX data. Integrating single-cell ATAC-seq mouse brain atlas data[31] with our P10 ATAC-seq data also identified all major cell types (Extended Data Fig. 3e,g). Furthermore, label transfer based on epigenetic states showed consistent identification of dominant cell types between ATAC-seq and RNA-seq (Extended Data Fig. 3d–g).

Spatial ARP-seq analysis of three human brain V1 region tissue sections, adjacent to those analysed using CODEX, identified 16 RNA and 9 ATAC clusters (Fig. 1d, Supplementary Fig. 20a and Supplementary Table 9). These data suggest that transcriptional profiles strongly define cell types during prenatal and neonatal brain development, with spatial patterns closely matching MERFISH data from adjacent tissue sections[17] (Supplementary Fig. 20d). RNA clusters R1, R2 and R9 (second trimester), R6 and R9 (third trimester) and R5, R3, R4 and R10 (infancy) represent cortical layers. Moreover, the ADT protein expression of CD56 (encoded by *NCAM1*) correlated with *NCAM1* RNA expression and chromatin accessibility mainly in the second trimester, but to a lesser extent later in development (Supplementary Fig. 20b,c). RNA expression and ATAC GAS for *RBFOX3*, primarily in the cortical layers, and *MBP*, which began to dominate WM starting from the third trimester, were consistent with observations from CODEX (Fig. 1c and Supplementary Figs. 11–14 and 20b,c). Thus, our spatial ARP-seq and CODEX analyses in mouse and human brains provide a comprehensive dataset, capturing spatial conservation and temporal evolution across all three layers of the central dogma of molecular biology.

Cortical chromatin accessibility persistence

We developed a computational framework to systematically examine RNA and ATAC patterns crossing three dimensions, that is, space, time and modality (Fig. 2c and Methods). The framework starts with applying generalized additive regression to model the spatial (cortical layers II/III, IV, V and VI) and temporal (P0–21) effects, and their interaction on GAS for ATAC and gene expression for RNA. We undertook a two-step procedure to categorize patterns of genes that exhibit significant spatial/temporal changes in either RNA or ATAC. First, we performed joint clustering on concatenated RNA and ATAC data to simultaneously capture the spatiotemporal patterns across both modalities. Subsequently, we combined patterns that exhibited similar RNA and ATAC profiles. Using this framework, applied to two postnatal datasets separately (S1 and S2), we identified 13–15 distinct RNA and 7–10 ATAC patterns, resulting in 27–30 unique combinatorial gene sets that display varied patterns of changes across time and space (Fig. 2e,f, Extended Data Fig. 6, Supplementary Fig. 21 and Supplementary Table 7). Although each cortical dataset (S1 and S2) has robust similarity (Supplementary Fig. 17), subtle variation does occur, probably due to the pixel size difference and the addition of P7 timepoint in the second dataset.

Previous single-cell RNA-seq and ATAC–seq mapping of PNs through development from embryonic (E10.5) to early postnatal (P4) has identified gene expression programs that define progenitors (*Eomes*, *Hes1*, *Hmgb2*, *Id4*, *Jun* and *Neurog2*) and lineage-spanning signatures (*Mn1*, *Mef2c*, *Neurod6*, *Nfib*, *Sox4*, *Sox11* and *Zeb2*)[3]. We verified the expression of expected genes and confirmed that early progenitor-restricted genes were not detected in any of our postnatal gene sets. We then categorized the 15 RNA clusters identified in the S2 datasets into three major groups based on shared spatial and/or temporal expression patterns. Layer-specific markers were generally found within the spatial and/or temporal categories, but also in the binary cluster exhibiting both temporal and spatial similarities (Fig. 2e and Supplementary Fig. 21).

We next investigated the distribution of the different PN subtypes. Expression profiles were also previously defined for PN subclasses, including CThPNs (*Chgb*, *Elavl2*, *Ndn*, *Tbr1*, *Tcf4*, *Tle4*, *Zfp428*), SCPNs (*Bcl11b*, *Crym*, *Etv1*, *Fezf2*, *Ldb2*, *Pex5l*, *Thy1*) and CPNs (*Cux1*, *Cux2*, *Dok5*, *Lhx2*, *Plxna4*, *Ptprk*, *Satb2*)[3]. We mapped these markers to determine whether their spatial segregation was accurate. Overall, we found that the upper cortical layer clusters (R1, R7, R8 and R13) were enriched for CPN markers. The deeper layers contained SCPN markers populating R2, R4/R5 and R15, and CThPNs that had a slightly broader cluster representation in R4/R5, R8, R12 and R13 (Supplementary Table 10). Each subclass of PNs had marker enrichment in RNA clusters related to space, in particular *Ptprk* (R1) for CPNs and *Rorb* (R2) for layer IV stellate neurons, *Etv1* (R5), *Fezf2* (R5) and *Ldb2* (R4) for SCPNs in layer V, and *Elavl2* (R5), *Ndn* (R4) and *Tbr1* (R5) for CThPNs in layer VI. By contrast, for R12–15 clusters, time was the main driver of RNA expression changes, with consistent temporal expression variation observed across a subset of layers. For example, *Satb2* (R13), *Plxna4* (R13) and *Bcl11b* (R13) presented such a pattern. The third group (R7–R11) exhibited a binary pattern influenced by both time and space; for example, *Cux1*, *Cux2*, *Dok5* and *Lhx2* were present in the binary RNA cluster R7 (Fig. 2e,g,h, Supplementary Figs. 22 and 23 (for S1) and Supplementary Table 10).

The ATAC GAS patterns exhibited a more diffuse spatial/temporal distribution, and the identified patterns did not always reflect the variations observed in the RNA clusters (Fig. 2e,f,h, Extended Data Fig. 6 and Supplementary Fig. 21). While RNA expression of many cortical layer-specific TFs (*Bcl11b*, *Cux1*, *Cux2*, *Lhx2*, *Satb2* and *Tle4*) aligned with chromatin accessibility, we observed a misalignment for a subset of key TFs (Fig. 2g–i and Supplementary Figs. 22–25). Specific subsets of genes presented chromatin accessibility trailing in time and/or more diffuse in space, when compared to their RNA expression. ATAC signal for lineage spanning genes like *Sox4, Sox11* and *Mef2c* and for layer-specific genes like *Sox5* and *Plxna4* trailed temporally when compared to RNA (Fig. 2g–i and Supplementary Figs. 22–25). We observed few instances where chromatin accessibility preceded gene expression, such as *Lmo4* (Fig. 2h and Supplementary Fig. 25 (for S1)). Notably, *Lmo4* has reported roles in astrocytes and may therefore also be relevant postnatally[3,32,33]. Thus, although epigenetic priming occurs during cortical layer development[3], in the postnatal development, we observe a decrease in the expression of a subset of cortical genes—at both the RNA and protein levels—that is not concurrent with the ATAC signals. Thus, these genes may retain an epigenetic memory of their previous transcriptional states of an earlier developmental stage.

Cortical open chromatin spatial spreading

Cortical-layer specific TFs/cofactors such as *Bhlhe22*, *Fezf2*, *Ldb2*, *Tshz2*, *Etv1*, *Foxp2* and *Tbr1* exhibited chromatin accessibility spreading across layers (Fig. 2g–i and Supplementary Figs. 22–25). For example, *Fezf2* and *Tbr1* were quite restricted at the RNA expression level to layer V and VI, respectively. However, their gene accessibility score extends to layer VI (for *Fezf2*) and IV (for *Tbr1*) (Fig. 2h). The dynamics between these two factors has been recently documented in which the CThPNs (*Tbr1*$^+$) in *Tbr1*-knockout mice are not distinct from their corticofugal counterpart, SCPN (*Fezf2*$^+$)[34]. The reduced ATAC coverage of *Tbr1* in layer V might be relevant, considering that *Tbr1* is a direct transcriptional repressor of *Fezf2*[34]. Conversely, *Fezf2* accessibility in layer VI may be permitting, as *Fezf2* is not a direct repressor of *Tbr1*[34]. We have previously shown that the repressive histone mark H3K27me3 is deposited at the TSS of genes that are not expressed in specific cortical layers, and

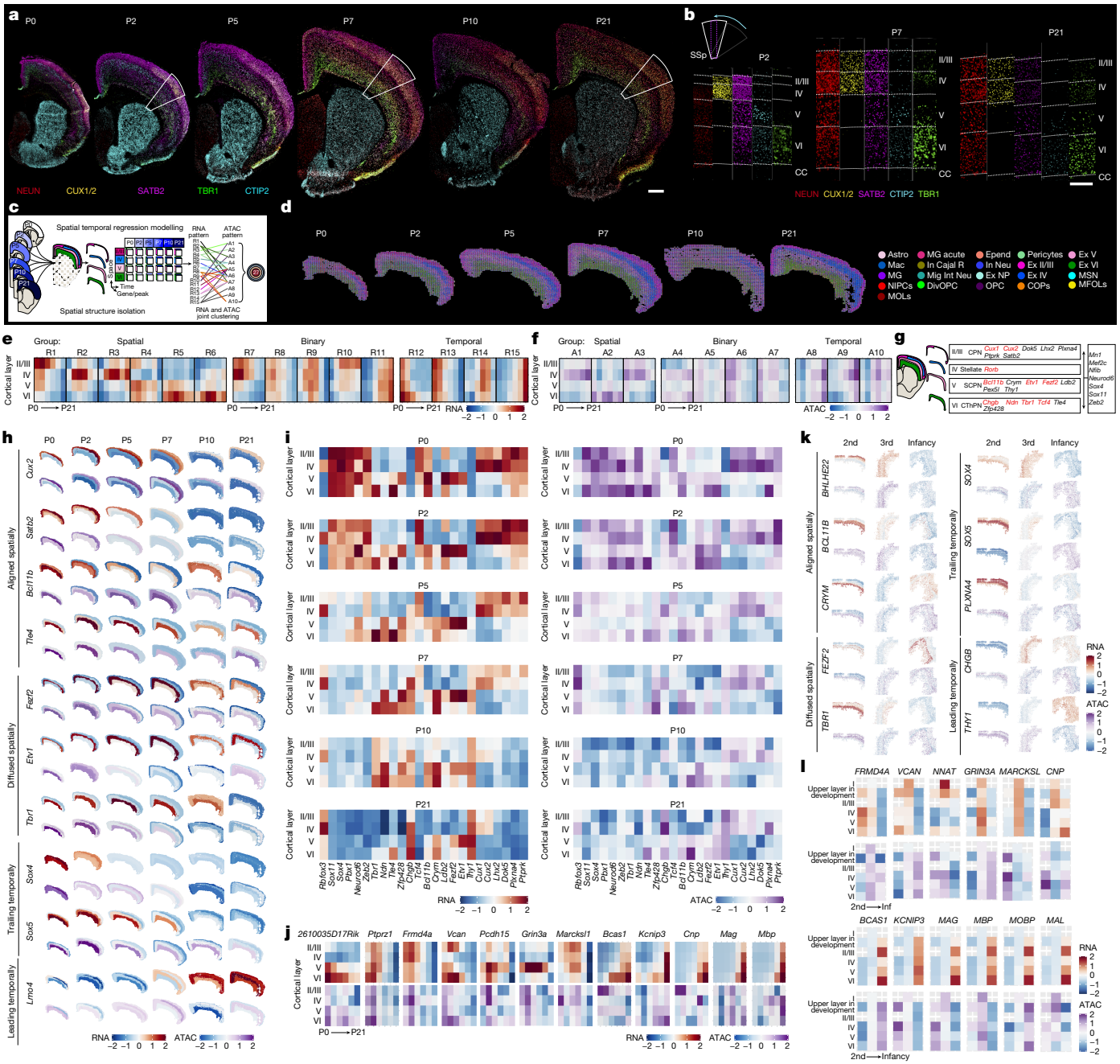

Fig. 2 | Spatiotemporal dynamics of transcriptome and chromatin accessibility of the mouse and human brain cortical layers. a, CODEX images of the mouse brain coronal sections from P0 to P21. Scale bar, 500 µm. **b**, CODEX staining of delineated cortical layers in the region of interest indicated by dashed rectangles in **a**. SSp, primary somatosensory area. Scale bar, 250 µm. **c**, Schematic of the spatiotemporal regression model on mouse brain cortical layers. **d**, Different cell types in cortical layers (S2) from the spatial RNA data. Epend, ependymal; Ex, excitatory; In, inhibitory; Mac, macrophages; MG, microglia; neu, neurons; NIPC, neuronal intermediate progenitor cell; MSN, medium spiny neurons; Cajal R, Cajal–Retzius cells; Mig Int Neu, migrating interneurons. **e**, The 15 RNA clusters generated from the regression model (S2). **f**, The 10 ATAC clusters generated from the regression model (S2). **g**, Representative genes in the cortical layers. **h**, RNA gene expression (top) and the ATAC GAS (bottom) calculated on the basis of the regression model for specific genes in mouse brains, segregated into groups based on variance of ATAC GAS in comparison to RNA expression. **i**, RNA gene expression (left) and the ATAC GAS (right) calculated on the basis of the regression model for specific genes in mouse brains. **j**, RNA gene expression (top) and the ATAC GAS (bottom) for myelination-related genes from the regression model. **k**, Representative gene expression (top) and ATAC GAS (bottom) for human brains, segregated into groups based on variance of ATAC GAS (bottom) in comparison to RNA expression (top). 2nd, second trimester; 3rd, third trimester. **l**, Representative RNA gene expression (top) and ATAC GAS (bottom) for oligodendrocyte-lineage-associated and myelination-associated genes through human V1 cortical development.

absent from genes that are expressed in those layers[1,35]. Thus, despite the spatially diffuse chromatin accessibility observed in postnatal cortical layers, Polycomb-mediated repression mechanisms may prevent ectopic expression of layer-specific genes.

Spatiotemporal RNA–ATAC cluster GO analysis

We also performed Gene Ontology (GO) analysis on each of the 27 combined RNA/ATAC patterns. General GO terms affiliated with neuronal

biology were described across the patterns associated with CPNs, CThPNs and SCPNs. However, other terms were more specific to PN subtype associated patterns. Glutamatergic synaptic transmission, including NMDA and AMPA receptor activity terms, were found in four clusters of R2-A3/A5/A7 (IV stellate neuron and SCPN-associated) and R5-A2 (CThPN and SCPN-associated) (Supplementary Fig. 26). Moreover, other neurotransmission terms (calcium-ion-regulated exocytosis of neurotransmitter, neurotransmitter secretion and positive regulation of synaptic transmission) were also identified in the CThPN and SCPN-associated R5-A2/A5 and R15-A5/A8 clusters. CPN-associated clusters (R7-A3, R8-A5 and R13-A6/A7) had the terms integrin signalling, axonogenesis, dendrite morphogenesis and neuron migration. Thus, all clusters included biological processes involved in general developmental changes, with CPNs being less mature due to the ongoing axonal guidance programs, while CThPNs and SCPNs were more mature with features of exocytosis, and glutamatergic synaptic transmission already underway. The maturity regarding postnatal development is consistent with embryonic development order[3].

Notably, we also identified clusters exhibiting GOs related to oligodendrogenesis[13,36,37] in R4/R5 (OPCs/committed oligodendrocyte precursors (COPs)/newly formed oligodendrocytes (NFOLs): *Fxyd6, Grin3a*, *Spon1*, *Pcdh15*, *2610035D17Rik*), R8 (OPCs/COPs/NFOLs: *Ptprz1, Sox6*, *Frmd4a*), R9 (OPCs/COPs/NFOLs: *Lhfpl3*, *Sdc3*; MOLs: *Marcksl1*), R13 (OPCs/COPs/NFOLs: *Nnat*, *Midn*, *Vcan*) and R15 (OPCs/COPs: *Bcas1*, *Tnr*, *Kcnip3*; MOLs: *Cnp*, *Nrgn*, *S100b*). NMDA receptor subunits indicating primed OPCs[38] were also segregated to R4 (*Grin3a*) and R9 (*Grin2d*) (Fig. 2j, Supplementary Figs. 26–28 and Supplementary Table 10). As clusters R4 and R9 are CThPN and SCPN-related, our data suggest an overlap between the time and space of OPCs and corticofugal PN maturation. Myelin-associated genes identified across the gene sets were exclusively clustered to R15 (*Mbp*, *Mag*, *Mobp*, *Plp1* and *Mal*), which is the final temporal program to arise beginning at P10, increasing at P21, and is associated with CThPNs and SCPNs (Fig. 2e,j and Supplementary Figs. 22 and 23).

There was a greater intensity of the spatial segregation of myelin-associated gene expression, where layer VI, but also V, had the highest levels for all the myelin genes such as *Cnp*, *Mag* and *Mbp* at P10 and P21. Chromatin accessibility for these myelination-related genes was already increased in several cortical layers as early as P5, suggesting chromatin priming for myelination during postnatal cortical development. Layer II/III was delayed in OPC differentiation and myelination programs (Fig. 2j and Supplementary Figs. 22 and 23), suggesting that myelination of upper-layer CPN neurons occurs later than for CThPN and SCPN neurons. Thus, our data indicate that OPCs and MOLs follow a similar spatial and temporal trajectory to that of CThPNs and SCPNs in early postnatal development while, at P10 and P21, the spatial myelination takes over, which is seen more profoundly in the deep layers where the SCPNs and CThPNs heavily populate.

Human cortical development benchmarking

We used our human V1 cortical maps as an exploratory benchmark for the mouse cortical dataset. As in mice, human neurogenesis initiates embryonically. Most patterning factors indeed exhibited similar layer distributions in mouse and human, with a notable reduction in expression at later development stages, for example, *BCL11B*, *SOX5*, *PLXNA4* and *TBR1* (Fig. 2h,k, Extended Data Fig. 7 and Supplementary Figs. 29 and 30), which is most probably due to cortical area expansion and lower cell density. Moreover, *FEZF2* was maintained through infancy, as observed in the mouse postnatal cortex (Fig. 2h,k). In a few cases, differences were observed between mouse and human expression patterns. *CUX2* expression in our mouse data were restricted to the upper layers during postnatal development (Fig. 2h). However, in the human second trimester sample, its expression was found in both the upper layers and VI/subplate (Supplementary Fig. 29). Recently, transient expression of *CUX2* in the human cortical developmental subplate was reported, which coincides with our results, as we detected deeper *CUX2* expression only in our second trimester sample[39]. As expected, the ATAC dynamics in the human visual cortex were more varied but, for many genes, RNA/ATAC patterns were conserved. The subset of *SOX4*, *SOX5* and *SOX11* has a prolonged ATAC signal after expression in the mouse cortex (Fig. 2h and Supplementary Figs. 24 and 25) and temporal persistence in the human cortex data (Fig. 2k and Supplementary Figs. 29 and 30). As in mice, the two largest categories of the genes that we interrogated fell into the subgroups of aligned chromatin accessibility (for example, *BCL11B*) and spatially spread (for example, *FEZF2*, *ETV1* and *TBR1*) chromatin accessibility.

Oligodendrogenesis and myelination initiate at P10 in mice and during the second trimester in humans[40,41]. We observed that most early OPC/COP/NFOL genes were expressed during the second (*NNAT*, *SPON1*, *FRMD4A*, *VCAN*, *TNR* and *LHFPL3*) and third (*SDC3*, *PCHD15*, *MARCKSL1*, *CNP*, *S100B* and *GRIN3A*) trimester, whereas all MOL or myelination genes were expressed at infancy (*MBP*, *MAG*, *MOBP*, *PLP1* and *MAL*) (Fig. 2l, Extended Data Fig. 7 and Supplementary Fig. 31). Notably, the temporal patterns of RNA expression in humans aligned well with the mouse data. Most genes expressed in the human second trimester showed high expression at P0 in mice, while human third-trimester genes were higher from P2 and P5 to P10 in mice, and all myelin-related genes were expressed during human infancy and mouse P7–21. We also observed more incidents of ATAC signals preceding RNA expression for genes related to oligodendrogenesis compared with those associated with neurogenesis (Fig. 2l, Extended Data Fig. 7 and Supplementary Fig. 31). This was observed for a subset of myelin-associated genes (*MAG*, *MBP* and *MAL*), consistent with findings in the mouse cortex (Fig. 2j and Supplementary Figs. 22 and 23). Notably, their gene activity was already detectable in the human second trimester. Thus, these human brain data provide an exploratory demonstration of the applicability of spatial ARP-seq to human tissue, establishing the technical feasibility and cross-species consistency of in situ epigenome, transcriptome and protein mapping, while further investigation is needed to draw more definitive biological conclusions.

Chromatin priming of CC myelin genes

In the developing mouse brain, myelination initiates around P10 (ref. 4). A lateral-to-medial progression of oligodendrocyte differentiation at these stages was previously observed by microscopy[42,43] and recently by in situ sequencing[44]. Protein expression of MBP and MOG, as assessed by CODEX, was initially restricted to the lateral part of the CC at P10 and spread throughout by P21, suggesting a lateral-to-medial progression of myelination (Fig. 3a,b, Extended Data Fig. 8a,b and Supplementary Figs. 2–9). We used the spatial ARP-seq developmental dataset (P0–21) to further investigate postnatal myelination at the spatial and multi-omic level (Fig. 3c and Extended Data Figs. 8c and 9a). Protein expression of MBP and MOG was detected at P10 and P21 but not at P0 (Fig. 1l and Extended Data Fig. 3b). *Mbp* and *Mog* presented chromatin accessibility and expression at the lateral part of the CC between P7 and P10 and became abundant in the whole CC at P21 (Fig. 1j,k, Extended Data Fig. 2f,g and Supplementary Fig. 18c–e). Before P7–10, the CC was characterized by markers of OPC such as *Olig2* and *Pdgfra* (Fig. 3a,b, Extended Data Fig. 2f,g and Supplementary Figs. 2–7 and 18c,d). Thus, our data are in general consistent with previous reports[37,45,46], as *Pdgfra*$^+$ OPCs (including COPs and dividing OPCs (DivOPCs)) populate the brain and we observed PDGFRα^+ cells throughout development (Fig. 3b and Extended Data Figs. 8a–c and 9a).

Notably, we observed not only concordance between the transcription of oligodendroglia genes and their chromatin accessibility, but also chromatin priming at P0–5 in regions of the CC where RNA expression emerged later, at P7–10 (Fig. 3g). By P21, although transcription persists for some myelin genes, chromatin accessibility has already

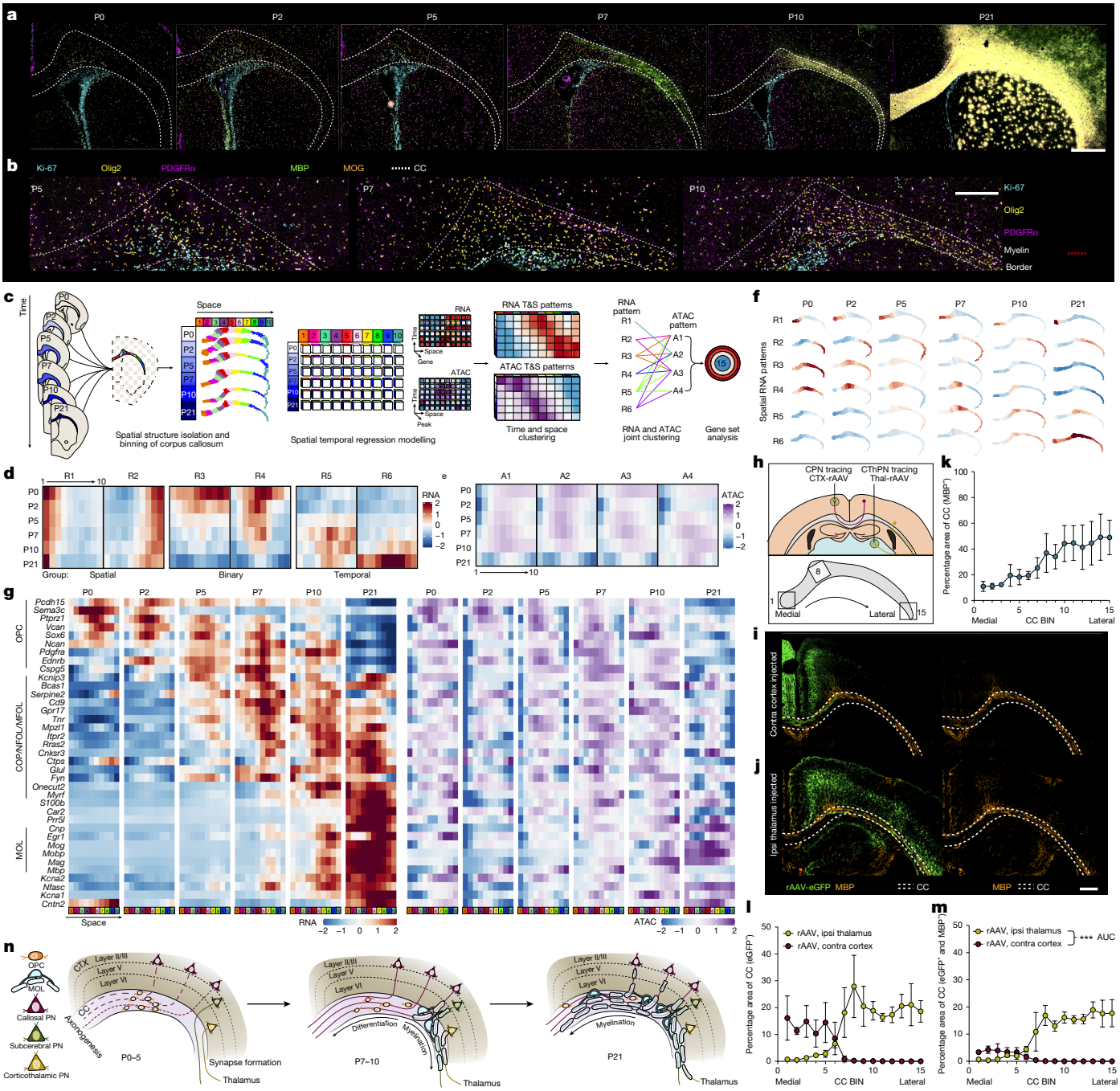

Fig. 3 | Spatiotemporal dynamics of the mouse CC during development and myelination. a, CODEX images of the mouse brain CC from P0 to P21. Scale bar, 500 µm. Individual channels are shown in Supplementary Figs. 2–9. **b**, Magnified CODEX images of the medial CC regions in **a** from P5, P7 and P10, showing staining for OLIG2, PDGFRα and Ki-67. Scale bar, 250 µm. **c**, Schematic of the spatiotemporal regression model on the mouse brain CC from P0 to P21. T&S, time and space. **d**, The six RNA clusters generated from the regression model. **e**, The 4 ATAC clusters generated from the regression model. **f**, Spatial RNA patterns for RNA clusters (R1–6) from the regression model. **g**, RNA gene expression calculated on the basis of the regression model for specific genes. **h**, Schematic of the injection sites and tracing pathways for CPNs and CThPNs (top) using retro-AAV-eGFP at the terminal location for both tracts separately. Bottom, the segmentation strategy using confocal imaging at high magnification (×40) for MBP staining and retro-AAV-eGFP labelling quantification throughout the CC. Thal, thalamus. **i**, Confocal images (×20) stitched together to capture the CC and overlying cortex of one hemisphere for CPN tracing in P10 mouse after retro-AAV-eGFP injection at P1. Representative retro-AAV-eGFP tracing from the contralateral cortical layer II/III injected terminal. **j**, Representative retro-AAV-eGFP tracing from the ipsilateral thalamic injected terminal. For **i** and **j**, scale bar, 250 µm. **k**, The percentage area of MBP staining per bin across the defined CC in each image moving medial to lateral ($n = 6$; 3 CPN traced + 3 CThPN traced). Data are mean ± s.d. for the region. **l**, The percentage area of retro-AAV-eGFP-labelled axons of the area of the CC defined per image. Data are mean ±s.d. for the binned region. $n = 3$ (CTX injected) and $n = 3$ (thalamus injected). **m**, The percentage area of co-labelled MBP and retro-AAV-eGFP-labelled axons of the area of the CC defined per image. Data are mean ± s.d. for the binned region. $n = 3$ (CTX injected) and $n = 3$ (thalamus injected). Significance was determined by calculating the area under the curve (AUC) formed by all the 15 datapoints per group, then running a two-tailed unpaired *t*-test ($P = 0.0001$) on the mean total area values (CTX, 18.79; thalamus, 143.2) with the standard error values (CTX, 2.770; thalamus, 7.942). ***$P < 0.001$. **n**, Summary of how myelination progresses in the CC and CTX.

declined (Fig. 3g). Thus, the spatial and temporal dynamics of chromatin accessibility during postnatal CC myelination differ from those of cortical layer–specific TFs, which show priming at embryonic stages[3], but exhibit some trailing postnatally.

Bidirectional myelination in postnatal CC

To determine whether there is indeed a lateral-to-medial progression in myelination, we isolated the CC (P0–21) and computationally partitioned it into ten separate regions spanning medial to lateral in their positional order (Fig. 3c). We took each segment separately to simultaneously determine the RNA expression and chromatin accessibility, and rebuilt the spatial architecture of the 10 segments to construct RNA and ATAC patterns and derive their respective gene set lists. This enabled us to analyse the CC development simultaneously across both time and space. We mapped 6 RNA and 4 ATAC patterns, and 15 combined from the integrated S1 and S2 datasets (Fig. 3d–f and Extended Data Figs. 8d and 9b,c). As in the cortical layers, RNA clusters could be broadly categorized into spatial, binary and temporal trends (Fig. 3d), and ATAC patterns were less defined and were influenced by both time and space (Fig. 3e). We observed clusters that exhibited high RNA expression early in either the medial (R1) or lateral (R2) region that was maintained from P0 to P21. Three other clusters had dynamic profiles in which early P0 expression shifted medially through time. R3 and R5 showed initially high lateral expression—at P0 for R3 and P5 for R5—which then shifted medially over time, with R3's central high expression also moving medially (Fig. 3d,f). Across all timepoints, the medial–lateral domain border corresponded with early MOG protein staining that we observed in CODEX and ADT at P10 (except for R1) (Fig. 3a,b and Extended Data Fig. 3b). Thus, while lateral-to-medial progression appears to contribute, it does not seem to be the main factor regulating axonal myelination.

The general landscape of the 15 concerted RNA/ATAC programs, along with their regional differences, were further characterized by GO term analysis (Supplementary Fig. 32). We found that only one group (R6) was identified with the terms strongly associated with myelination (*Cnp*, *Egr1*, *Mog*, *Mobp*, *Mag*, *Mbp* and *Plp1* among others)[37]. This cluster was not only producing myelin, but also probably undergoing myelination, as we identified genes associated with the node of Ranvier, including neurofascin, Kv1.1/1.2 and contactin (*Nfasc*, *Kcna1*, *Kcna2* and *Cntn2*)[47–50] (Fig. 3g, Supplementary Figs. 33 and 34 and Supplementary Table 11). We found markers across two main clusters R4 and R5 (Supplementary Figs. 32–34), with stronger associations to specific oligodendroglia progenitors cell types (R4, OPCs/COPs: *Ptprz1*, *Vcan*, *Sox6*, *Ednrb*; and R5, OPCs/COPs: *Pdgfra*, *Ncan*, *Cspg5*, *Kcnip3*, *Bcas1*, *Serpine2*, *Cd9*, *Gpr17*, *Pcdh15*). Shared genes among COPs, NFOLs and MFOLs were primarily in R5 (COPs/NFOLs/MFOLs: *Tnr*, *Sulf2*, *Fyn*, *Itpr2*; NFOLs: *Rras2*, *Cnksr3*, *Onecut2*; and MFOLs/MOLs: *Ctps*, *Glul*). Thus, R5 is likely to represent an overall more mature population of oligodendrocytes. Cluster R6-A1/A3 also contained a mix of COPs and MOL-specific subtype genes (*Mpzl1*, *Slk*, *Car2* and *Prr5l*), placing this population even more differentiated than R5 but less than R6-A4 (Fig. 3g, Supplementary Figs. 33 and 34 and Supplementary Table 11). Thus, in contrast to the CODEX protein and cell-type-only analysis, spatial ARP-seq indicates a medial-to-lateral maturation hierarchy: R4-A2/A3 ≫ R5-A2–A4 ≫ R6-A1/A3 and R6-A4.

R4, which is associated with an OPC/COP signature, showed initially high expression in the central CC (regional space bins 3–6) of each hemisphere, which decreased over time (Fig. 3d,f). By mapping this population to the cell types, we found that the cluster trend probably reflects the remnant neural progenitors like cells and OPCs (Extended Data Figs. 8c and 9a). There is a proportion of these cells in the P0 and P2 tissue sections that are co-labelled with OLIG2 and PDGFRα (Fig. 3b). Thus, our data suggest that an early response of OPCs/COPs begins at P0 that modestly favours the central CC (R4). Notably, at P5–10, the gene expression of NFOLs and MFOLs (associated with R5) can be seen with a lateral preference, indicating that, while there are OPCs populating the central CC, there is already a simultaneous oligodendrocyte differentiation process occurring at the lateral CC. At P10, the R6 myelination gene program is already active in the lateral CC (Fig. 3f,g and Extended Data Figs. 8d and 9b,c) and shifts medially by P21, suggesting that two concurrent myelination processes are occurring in the CC: one initiating laterally and another emerging centrally. In summary, myelination may follow a timed, sequential, bidirectional process, with OPCs/COPs from the postnatal wave first migrating and differentiating laterally, followed by a second phase of medial migration and differentiation (Fig. 3n).

PN myelination orchestration

We also found that the MOL and myelin-associated cluster (R6) was enriched for synaptic transmission terms, whereas the OPC/COP cluster (R4) was associated with earlier neuronal programs, including neuron migration and neuron/axonogenesis (Supplementary Fig. 32). The R5 cluster seems to represent an intermediate program between early R4 and late R6. We found GO terms that further supported this: negative regulation of axonogenesis, negative regulation of neuron projection development and synaptic-transmission-related terms. This was unexpected, as the CC is depleted of neuronal cell bodies, suggesting that these transcriptomic signatures might be derived from neuronal axons. Moreover, the neuronal programs were spatially segregated, with more mature programs expressed at the lateral end of the CC, and the developmental neuron programs expressed medially within the CC (Fig. 3f and Supplementary Fig. 32). Notably, we also found an array of cortical layer marker gene expression of *Elavl2*, *Tle4*, *Lmo3* and *Bcl11b* in R3 (SCPNs and CThPNs); *Cux1*, *Lhx2* and *Plxna4* (layer II/III, CPNs) in R4; *Thy1* and *Rorb* in R5 (layer IV, stellate; and layer V, SCPNs); and *Hpca, Gda, Ddn* and *Ptprn* in R6 (layer V, SCPNs; and layer VI, CThPNs) (Supplementary Fig. 36 and Supplementary Table 11). Although we observed chromatin accessibility at some of these genes in the CC (Supplementary Fig. 36), it was much lower than in the cortical layers (Supplementary Fig. 35). Thus, the expression of these markers was consistent with cortical layer data and may result from RNA transport into axonal tracts. Other genes with medial expression linked to CPNs include *Foxg1* and *Epha4*, which are both involved in the axonal guidance of this PN subtype[51,52] (Supplementary Fig. 36). Taken together, there are SCPN and CThPN marker expression signatures in the regions of the CC where myelination initiates, along with expression of genes associated with established neural transmission. In the medial region, which is myelinated later, we observed gene expression associated with CPN that is still undergoing axonogenesis. When considering the inside-out temporal development of PNs, SCPNs are specified after CThPNs. Furthermore, the establishment of their axons is also separated in time, in which corticofugal PNs begin projecting embryonically around E14.5, whereas CPNs project postnatally and continue refining through P8 (refs. 53–55).

Our analysis of the cortical layers suggested that layers II/III CPNs might undergo myelination after layers V/VI, where SCPNs and CThPNs are present (Fig. 2j). To trace the preference of myelination along these different PN tracts in the CC, we used a retrograde-AAV-eGFP tracing strategy (Fig. 3h). By injecting P1 mice with the retro-AAV-eGFP targeting the terminal portion of the tract (either a contralateral cortical or ipsilateral thalamic injection), we achieved selective labelling of CPNs and CThPNs, respectively, from their terminus to their cell body located in the developing cortex at P10 (Fig. 3i,j). We observed that the cingulum bundle is the interface between the CPN and CThPN tracts, and is also the stark myelin border at P10 (Fig. 3h–j). We first quantified the total MBP staining along the CC by taking successive medial to lateral confocal images and found an increase in MBP along this axis with a steep slope at CC bins 6–8 that aligns with the cingulum

bundle (Fig. 3k). Using the same strategy, we were able to map the area of rAAV-eGFP tract coverage and dual-labelled rAAV-eGFP/MBP within the CC for both PN groups (Fig. 3l,m). We observed that the labelled CPN signal decreases while the CThPN increases through the medial to lateral progression. Moreover, MBP staining in the lateral portion highly overlaps with the rAAV-eGFP-labelled CThPN axons. Thus, at P10, CThPN axons located in the lateral CC are already myelinated, while medially located CPN neurons are starting to be myelinated, indicating that cues from these neurons orchestrate the OPC migration and MOL myelination process in a lateral-to-medial manner, as suggested by the spatial ARP-seq data (Fig. 3n).

Spatial mapping of focal de- and remyelination

To study the process of demyelination and remyelination, we injected 1% LPC into the mouse CC (unilaterally and ventral to cingulum bundle) at P85 and conducted CODEX, spatial ARP-seq and spatial CTRP-seq (targeting H3K27me3) analysis of coronal sections (Supplementary Table 8). CODEX provided a detailed single-cell resolution and morphological visualization of the lesion evolution at 5 and 10 days post-lesion (d.p.l.), and during repair at 21 d.p.l. (Fig. 4a). We performed unsupervised clustering of protein expression across six coronal samples. Cell types were assigned to each cluster accordingly based on the marker expression and the Allen Brain Atlas[20] (Fig. 4b and Extended Data Fig. 10). Gross changes in cellular distribution were observed at 5, 10 and 21 d.p.l., with MOLs and myelin being lost at the lesion site. Astrocytosis ($GFAP^+$ cells) was prominent along the perilesion, and there was observable macrophage/microglial ($CD11b^+$) accumulation in the lesion at 5 d.p.l. with further evolution at 10 d.p.l. By contrast, by 21 d.p.l., the lesion site was much smaller, and successful remyelination was observed in the CC, with a significant reduction in the astrocytic and macrophage/microglial presence (Fig. 4a and Extended Data Fig. 10). At 5 d.p.l., there was already a response of OPCs to the insult (OLIG2 and PDGFRα) and increased proliferative activity (Ki-67) in the lesion area (Fig. 4a), highlighting inflammation and the beginning of the regenerative processes. MOLs remyelinated most of the lesion area (MBP staining) by 21 d.p.l. (Fig. 4a).

Spatial ARP-seq was performed on tissue sections adjacent to those used for CODEX. We identified 13 ATAC-specific and 25 RNA-specific clusters (Fig. 4c,d). All modalities (RNA and ATAC) delineated specific regions of mouse coronal brains showing agreement with the Allen Brain Atlas[20]. For the integrated ATAC and RNA data, we delineated major regions of the mouse brain at 5, 10 and 21 d.p.l. These include all six cortical layers (II/III, cluster J10; IV, cluster J5; V, cluster J3; and VI, cluster J4); fibre tracts (cluster J9) such as the CC, fimbria, internal capsule, stria medullaris (SM) and stria terminalis; the choroid plexus (cluster J7) of the lateral and third ventricles; the caudoputamen (cluster J12); the thalamus (clusters J11, J13 and J15); and, importantly, the clusters elicited by neuroinflammation (J2) (Fig. 4e). Marker genes for RNA and ATAC were calculated, including *Sox10* and *Neurod6* (Extended Data Fig. 11)—markers for oligodendrocytes and cortical layer neurons, respectively. We also applied spatial CTRP-seq (H3K27me3) to adjacent mouse brains at 5 and 21 d.p.l., identifying 14 H3K27me3 and 25 RNA-specific clusters (Fig. 4f and Extended Data Fig. 12a,b). Integration of H3K27me3 and RNA also yielded detailed spatial delineation at both timepoints, showing high concordance between our two methodologies (spatial tri-omic mapping and CODEX) (Fig. 4g and Extended Data Fig. 12c–f). Finally, the cell types in our mouse brain data were assigned using cell2location to map scRNA-seq[30,56] onto our RNA data in spatial ARP-seq and spatial CTPR-seq (Extended Data Fig. 12g). The presence of immune cells ($CD45^+$) was confirmed by spatial ARP-seq and spatial CTPR-seq in all three modalities, localized to the lesion core, the injection site, and in the meninges at the brain surface as previously described[57–60], but unexpectedly also in the SM, distant from the site of the primary lesion (Fig. 4h).

Microglial dynamics in focal de- and remyelination

We next evaluated gene expression, chromatin accessibility (by calculating the GAS), along with histone modification (by calculating the chromatin silencing score (CSS), for H3K27me3), for marker genes related to oligodendrocytes, neurons and neuroinflammation (Fig. 4h,i). At 5 and 10 d.p.l., *Olig2* and *Mog* expression was reduced in the lesion area at the levels of ATAC, RNA and protein, accompanied by an increased CSS for H3K27me3 (Fig. 4h,i). By 21 d.p.l., after remyelination, *Olig2* and *Mog* repopulated the lesion area in the CC, except for a remaining demyelinated region dorsal to the ventricles, and H3K27me3 exhibited low CSS (Fig. 4h,i). At 5 and 10 d.p.l., the expression of *Icam1* (CD54), typically expressed on endothelial and immune cells[61,62], was noted in both the lesion and ventricular areas across ATAC, RNA and protein modalities, with a low CSS for H3K27me3. By 21 d.p.l., *Icam1* remained localized to the periventricular regions across the ATAC, RNA and ADT modalities, with persistently low CSS for H3K27me3 (Supplementary Fig. 37). *Cd9*, a marker of immune cells and OPCs[63], had heightened RNA expression, chromatin accessibility and low CSS in both the lesion and CC, with differences in the levels (for RNA/ATAC, very high in the lesion, lower in the CC; for H3K27me3, very low in the lesion and reduced in the CC) (Extended Data Fig. 13).

Macrophage/microglial markers such as *Cx3cr1*, *Cd86* and *Csf1r* (encoding CD115)[64–70] were predominant in the lesion region in both ATAC and RNA profiles, with a consistently low CSS for H3K27me3 at 5 d.p.l. By 21 d.p.l., these markers were no longer present in the former core lesion area, but persisted in discrete periventricular demyelinated regions, where their H3K27me3 CSS remained low (Fig. 4h, Extended Data Fig. 13 and Supplementary Fig. 37). As $CD11c^+$ microglia have been described to be also transient in development, appearing postnatally (P0–7) in WM tracts like the CC, and diminishing in adolescent mice[71,72], we investigated these microglia (or potentially macrophages) population in our developing mouse brain CODEX and spatial ARP-seq datasets. Indeed, we were able to identify $CD11c^+$ (encoded by *Itgax*) microglia/macrophages at P0, residing mostly medial to the lateral ventricles until P5 and P7 when they localized to the CC, dorsal to the ventricles (Supplementary Figs. 38 and 39a). Importantly, our CODEX data for the LPC model identified a large cluster of $CD11b^+$ cells at the lesion core with minor $CD11c^+$ cellular contribution at 5 d.p.l. $CD11c^+$ cells expanded in number, filling the lesion core at 10 d.p.l., with a proportion being dual positive for $CD11b^+$. By 21 d.p.l., the $CD11c^+$ cells retreated but were still present in demyelinated areas (Supplementary Fig. 39b). A similar pattern was observed with spatial ARP-seq for both RNA and ATAC signal, as well as at the protein level, although the latter showed weaker but consistent signals, probably due to limited capture efficiency. An opposite pattern was observed for H3K27me3 in the corresponding regions from spatial CTRP-seq (Fig. 5a–d).

Distal microglia activation along WM tracts

Spatial ARP-seq revealed the presence of immune cells in regions distal from the primary lesion (Fig. 4h) accompanied by a spatially broad spatial distribution of CD68 protein expression and *Cd68* chromatin accessibility in the SM (a WM tract that carries afferent fibres to the habenular nuclei from several forebrain nuclei) (Fig. 5a–c). *Cd68*, a marker for phagocytotic activity, is associated with more mature and functional microglia, which may represent sparse microglial (or macrophage) activation. We also observed protein expression of *Cd44* and *Ptprc* (encoding CD45) in this region, and reduced *Olig2* and *Mog* protein levels in the ipsilateral SM (Fig. 4h and Supplementary Fig. 37). Global interrogation of our coronal LPC CODEX data also showed signals for $CD11b^+$ and $CD11c^+$ cells at 10 d.p.l. and 21 d.p.l. in regions distant from the lesion, such as the SM (Fig. 5e–h and Supplementary Fig. 39c–e).

To map the distal spread of microglia/macrophages along the anterior–posterior axis, we performed CODEX analysis of sagittal sections

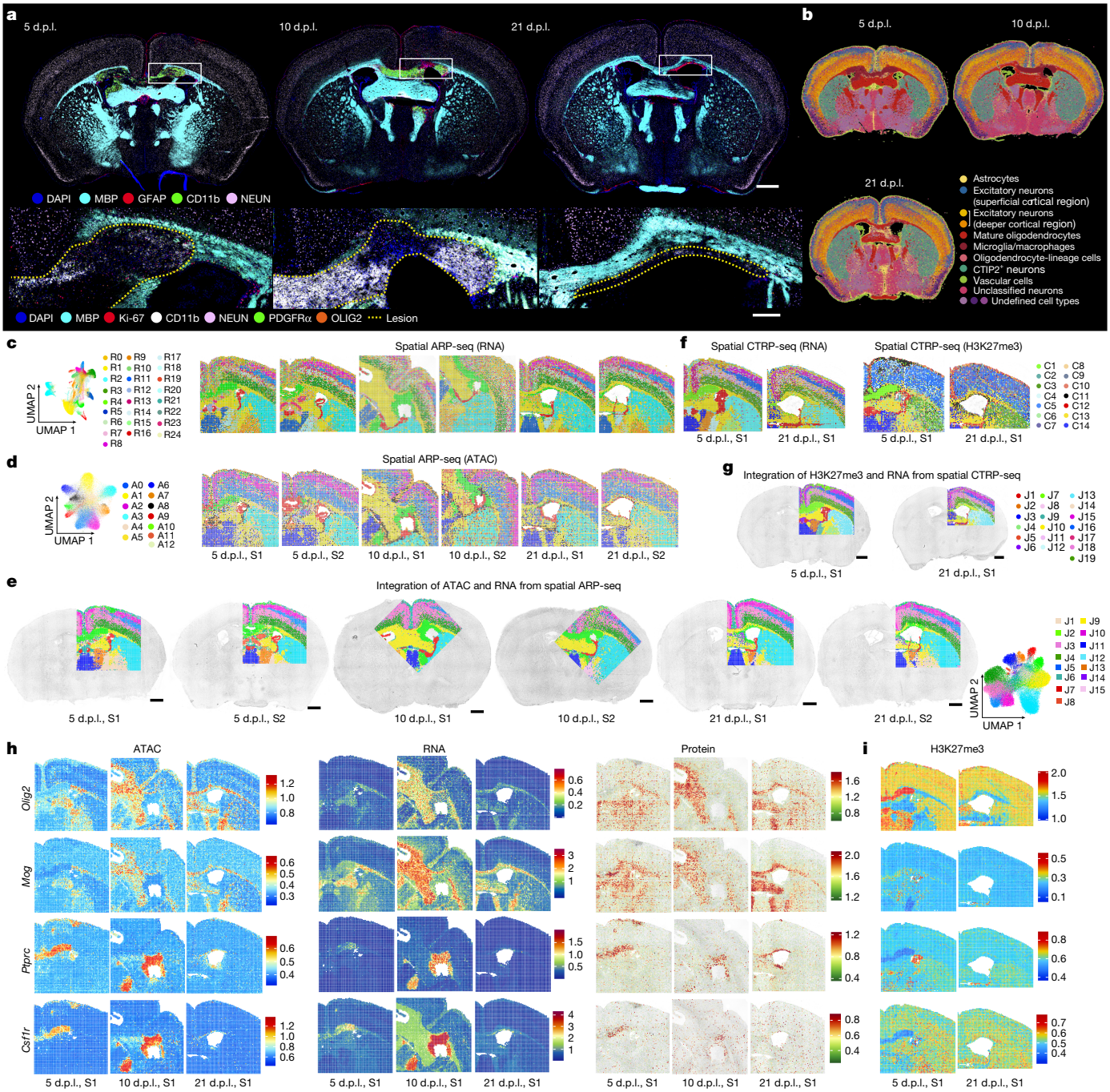

Fig. 4 | Spatial tri-omics mapping of the LPC mouse model brains at 5, 10 and 21 d.p.l. a, CODEX images of whole mouse brains at 5, 10 and 21 d.p.l. The images at the bottom are magnified views of the regions indicated by the white rectangles. Scale bars, 800 µm (top) and 200 µm (bottom). **b**, Seurat clustering of the CODEX images in **a**. **c**,**d**, UMAPs and spatial distribution of RNA (**c**) and ATAC (**d**) clusters in spatial ARP-seq (S1 and S2). **e**, Integration of RNA and ATAC data in spatial ARP-seq (S1 and S2). Scale bars, 800 µm. **f**, The spatial distribution of RNA (left) and H3K27me3 (right) clusters in spatial CTRP-seq (S1). **g**, Integration of H3K27me3 and RNA data in spatial CTRP-seq (S1). Scale bars, 800 µm. **h**,**i**, Spatial mapping of GAS, gene expression and ADT protein expression in spatial ARP-seq (**h**), and CSS for H3K27me3 in spatial CTRP-seq (**i**) for *Olig2*, *Mog*, *Ptprc* and *Csf1r*.

near the LPC injection site at 5 d.p.l. We found CD11b$^+$ cells located distally from the primary lesion, but also retained in the WM tracts (Fig. 5i–l). The distal spread occurred in the directions anterior, posterior and ventral (Fig. 5i (i and ii)) to the lesion (Fig. 5i–l), while mostly encompassing the distal parts of the WM tracts like the posterior part of the CC (splenium) and, notably, even further ventrally in the bottom of the fornix (a WM tract emerging from the hippocampus). We also observed CD11b$^+$ cells in the dorsal hippocampal commissure (DHC) (Fig. 5i).

We performed a more global brain analysis using Tris-mediated retention of in situ hybridization signal during clearing DISCO (TRIC-DISCO), a probe-based strategy for cleared brain 3D imaging of specific RNA transcripts[73]. Using the microglial/macrophage marker *Csf1r* on whole-brain tissue extracted from mice at 5 d.p.l. (Fig. 5m,n and Supplementary Videos 1–3) recapitulated and expanded our CODEX imaging, as we saw spreading of the microglial/macrophage population to both hemispheres with a higher signal intensity ipsilateral to the injection. This distribution was also seen in our coronal CODEX

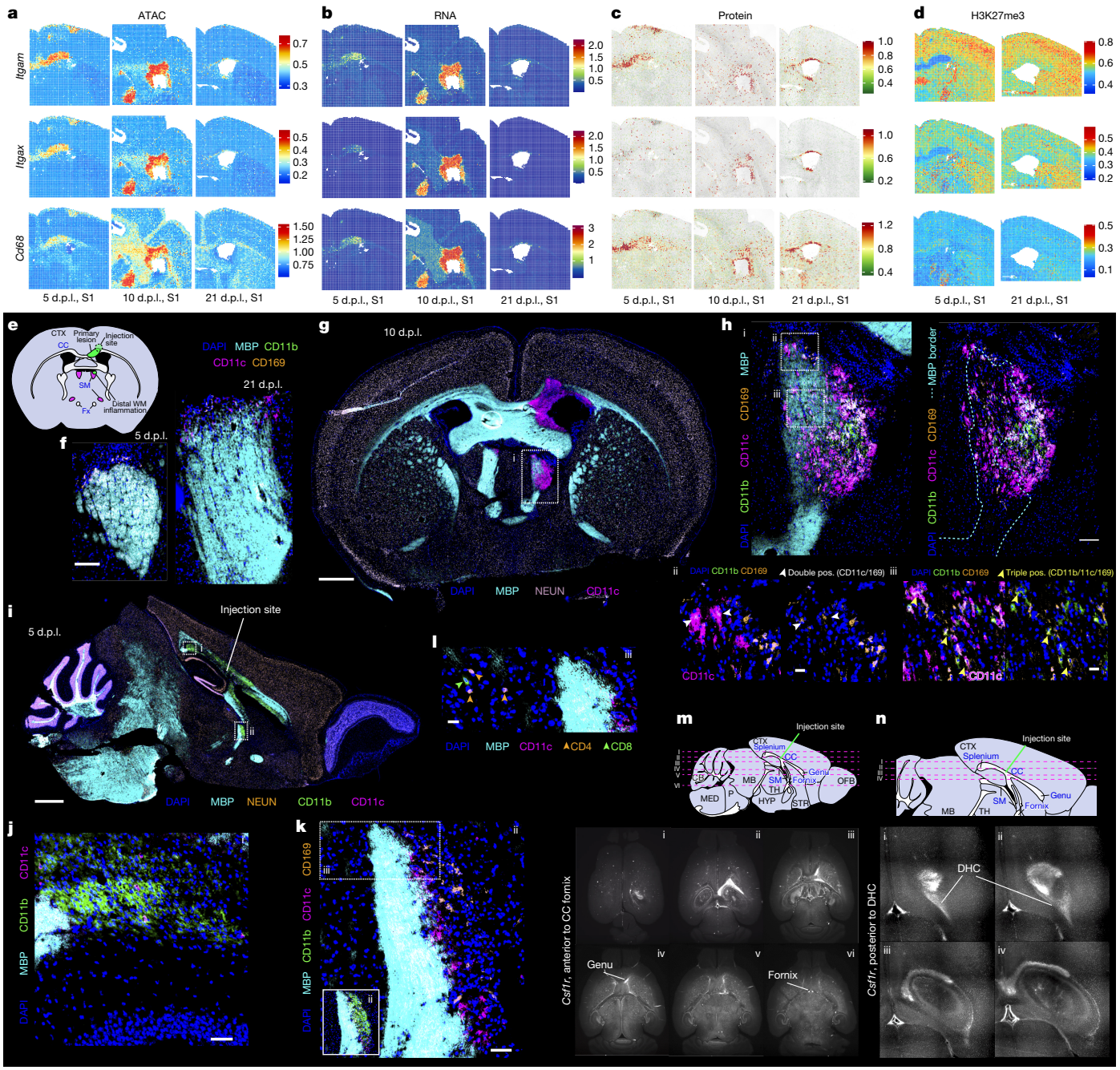

Fig. 5 | CD11c$^+$ microglia emerge in distal WM regions. a–**d**, Spatial mapping of GAS (**a**), gene expression (**b**), ADT protein expression (**c**) and CSS (**d**) for *Itgam*, *Itgax* and *Cd68* in both spatial ARP-seq (**a**–**c**) and spatial CTRP-seq (**d**). **e**, Schematic of the primary lesion and distal WM of the SM locations in a coronal tissue section. Fx, fornix. **f**, CODEX images of the SM of 5 and 21 d.p.l. mouse brains. pos., positive. **g**, CODEX image of 10 d.p.l. coronal section showing CD11c$^+$ cells in both the primary lesion and SM. **h**, Higher-magnification CODEX images of microglia in the SM at 10 d.p.l. **i**, CODEX image of the LPC mouse brain on a sagittal tissue section at 5 d.p.l. **j**, Magnified image of the region of interest indicated by a white dashed rectangle (i) in **i**. **k**, Magnified image of the region of interest indicated by a white dashed rectangle (ii) in **i**. **l**, Magnified image of the region indicated by a white dashed rectangle (iii) in **k**, with staining for CD4 and CD8. **m**,**n**, TRIC-DISCO results of *Csf1r* from the anterior (**m**) and posterior (**n**) direction relative to the injection. Scale bars, 20 µm (**h** (bottom) and **l**), 50 µm (**j** and **k**), 100 µm (**f** and **h** (top)), 800 µm (**g**) and 1 mm (**i**). CB, cerebellum; HYP, hypothalamus; MB, midbrain; MED, medulla; OFB, olfactory bulb; P, pons; STR, striatum; TH, thalamus.

at 5 d.p.l. Importantly, we observed *Csf1r* spreading (anterior to the injection) through to the genu of the CC and ventrally to the fornix (Fig. 5m). In the posterior direction, we saw *Csf1r* intensity spreading to the splenium of the CC and along the DHC (Fig. 5n). A closer look at the distal population in the CODEX dataset showed CD11c$^+$ microglia/macrophages that co-stained for CD11b and a small subset for CD169 (Fig. 5h,k). Notably, the distal cluster along the SM were found to be close to CD4$^+$ and CD8$^+$ T cells (Fig. 5k). We also performed spatial sequencing on the sagittal section and found that, even though the CD11c$^+$ cells in the distal sites were few, we were able to capture emerging ATAC signal for *Itgax* and *Itgam* (encoding CD11b) and RNA signal for *Csf1r* (Extended Data Fig. 14). This dataset is rather sparse for in-depth analysis, warranting future studies. Thus, our CODEX and TRIC-DISCO analysis further indicates that induction of a focal demyelinating lesion in one area of the brain can lead to microglial/macrophage activation distally.

Distinct primary and distal microglial dynamics

To understand the distal microglia/macrophages properties, we performed a stepwise strategy to (1) dissect the primary lesion and distal general compartments; (2) select microglia-specific pixels positive for *P2ry12*, *Tmem119* and *Cx3cr1*; and (3) perform a deeper investigation into the microglia occupying these different compartments (Fig. 6a–c and Extended Data Fig. 13). For the lesion compartments, we identified the lesion area by first selecting for the microglial pixels (core), then expanded the region of interest by integrating the tissue area occupying 2–3 pixels away (about 80–100 µm) from the identified microglial-specific pixels (Fig. 6a–c). We applied this strategy to our coronal dataset between 5 and 21 d.p.l. as we could include both the primary lesion and the distal WM site of SM in the sequencing region of interest. Although the most distal sites in the 5 d.p.l. sagittal section were sparse in our dataset, we used the sequencing data to understand whether the gene expression changes were proportional to distance from the primary lesion as we could look at the tracts along the axons running anterior to posterior through the cingulum bundle (Extended Data Fig. 14).

Cell proportion analysis indicated that microglia were enriched at the primary lesion at 5 and 10 d.p.l., whereas, in the distal WM, the microglial number increased by 10 d.p.l. (Fig. 6d). We performed unsupervised clustering with joint ATAC and RNA data on the lesion compartments and segregated five distinct compartments (Fig. 6e). Lesion compartment 1 (LC1) was limited in size in total pixel count and was primarily localized to regions proximal to the ventricle system or blood vessels. All other clusters were identified during the primary lesion evolution from 5 to 21 d.p.l., with only 10 d.p.l. having all 5 lesion compartments; LC2 was identified as the primary lesion core, with distal WM regions having very limited LC2 throughout the disease course (Fig. 6e,f and Supplementary Fig. 40a). By contrast, LC3 appeared only at 10 d.p.l. in distal lesions.

An array of proteins in our spatial ARP-seq data had differential expression in these compartments (Fig. 6g) and GO terms for RNA and ATAC also segregated the compartments (Supplementary Fig. 41b). While all the lesion compartments (except for LC1) were identified to have microglia (with the presence of CD68, CD11b, CX3CR1 and CD169 protein), the overall expression in LC5 was decreased. Instead, LC5 had expression of oligodendrocyte protein markers (OLIG2 and MBP) and was the compartment with the highest expression of PD-1 (also known as CD279; Fig. 6g)—an inhibitory receptor of T cells, B cells and myeloid cells. While the LC1–4 compartments were positive for CD49f protein (highest in LC2), this laminin receptor subunit with costimulatory effects[74] was absent from LC5. The GO term analysis of RNA and ATAC supported the protein expression profile in which LC5 was demarcated by axon ensheathment and glial cell differentiation among other related terms. LC2 and LC3 were associated with active inflammation—LC2 was associated with adaptive immunity, such as lymphocyte differentiation, while LC3 was more related to innate immunity, including regulation of innate immune response and myeloid cell activation. LC4 was related to cell–cell adhesion, cell junction assembly and synapse assembly (Supplementary Fig. 41b). Taken together, our compartment analysis suggests that immune responses are differentially phased between the primary lesion and distal WM sites.

We next performed microglial subclustering on microglial-specific pixels (positive for *P2ry12*, *Tmem119* and *Cx3cr1*) and, for the remaining pixels, we assigned cell identities across the primary lesion and distal WM (Fig. 6h and Supplementary Fig. 40b). Notably, at 5 d.p.l., MC2 (microglia cluster 2) and MC1 microglia were predominant at the core of the primary lesion. At 10 d.p.l., the primary lesion was enriched in MC3 microglia, while the distal lesion-like compartment was enriched in MC1 and MC2 microglia (Fig. 6h). We further performed GO analysis on differentially expressed genes between the three microglial subclusters and found that MC1 was neuron/myelin supportive (*Nrxn3*, *Tmeff2*, *Grip1* and *Cntn2*), while MC3 was more pro-inflammatory and phagocytotic (*Apoe*, *Abca1* and *Btk*) (Fig. 6j,k). MC2 presented very few differentially expressed genes and, rather, had similarity to both MC1 and MC3, suggesting that it could be an intermediate microglial state between MC1 and MC3. We also determined their likely identity using module scoring, comparing gene sets from previous studies[75,76]. We found that nearly all ref. 75 microglial clusters (foamy, interferon-responsive and disease-associated microglia) and ref. 76 microglia (axon tract-associated, disease-associated and injury responsive) were predicted in our RNA dataset to a higher extent in the primary lesion at 10 d.p.l., with reduced prediction in the distal WM (Fig. 6i and Supplementary Figs. 40c,d and 41a). However, in one of the replicates (S1), the ATAC module prediction was higher in the distal WM, while, in the other (S2), the difference between the primary lesion and distal WM was not as marked, suggesting that the inflammation in this area is still evolving. Moreover, the ref. 76 injury-responsive module was predicted to be enriched in the distal WM lesion-like compartment rather than in the primary lesion core (Supplementary Figs. 40c,d and 41a).

Our data suggested that differential signalling and cellular interactions might occur specifically in primary and distal lesions at 5 and 10 d.p.l. To investigate this possibility, we performed CellChat analysis and found that MC1 cells were predicted to interact with other non-microglial CNS, in contrast to MC3 cells, which were interacting more with the other subclustered microglia (Fig. 6l and Extended Data Fig. 15a–c). We also mapped the cellular interactions over space, breaking the spatial interaction patterns (IPs) into different groups. IP-A had similar receptor–ligand spatial mapping between the primary lesion and the distal WM (fibronectin 1 and integrin subunit alpha 4, *Fn1–Itga4*). IP-B was characterized by interaction intensity along the periphery of the primary lesion but higher intensity in the core of the distal WM (*Cntn2–Cntnap2* and *Bdnf–Ntrk2*). IP-C had both core intensity for both sites; however, it was much stronger in the primary lesion (*Apoe–Lrp1* and *Plau–Plaur*). IP-D receptor–ligand spatial maps appeared to have interactions occurring more specifically in the distal WM region (*Tgfb3–Tgfbr2* and *Bmp7–Acvr2b*) (Fig. 6m and Extended Data Fig. 15d,e). Taken together, our data indicate that LPC lesions can induce lesion-like compartments in the distal WM, displaying a delay in microglial activation compared with the primary WM lesion.

Discussion

While the inherent diversity and heterogeneity of the CNS were first recognized through early drawings of neuronal and glial morphology[77], recent single-cell and spatial technologies now provide deeper insights into the complex multicellular programs underlying development and disease. Here we provide a spatial multiomic compendium encompassing the development of the mouse CTX and the CC, benchmarked against human development, and the progression of focal demyelination and remyelination. We reveal temporal persistence and spatial spreading of chromatin accessibility for specific cortical-layer-defining TFs, as well as priming of myelin gene accessibility across the CC during myelination. Our data further suggest coordinated orchestration between layer-specific PN axonogenesis and myelination. We also identify microglial activation at distal sites in a focal mouse model of multiple sclerosis, with delayed induction dynamics relative to the lesion core.

Chromatin accessibility priming occurs during both embryonic cortical layer development[3] and transitions to disease-associated states[13]. While we observe such temporal and spatial priming at the CC during oligodendroglia lineage progression and myelination, we also detected epigenetic trailing of specific cortical layer-defining TFs. As some of these factors still exhibit transcription, albeit at reduced levels over time, this may reflect a fading epigenetic memory of developmental states.

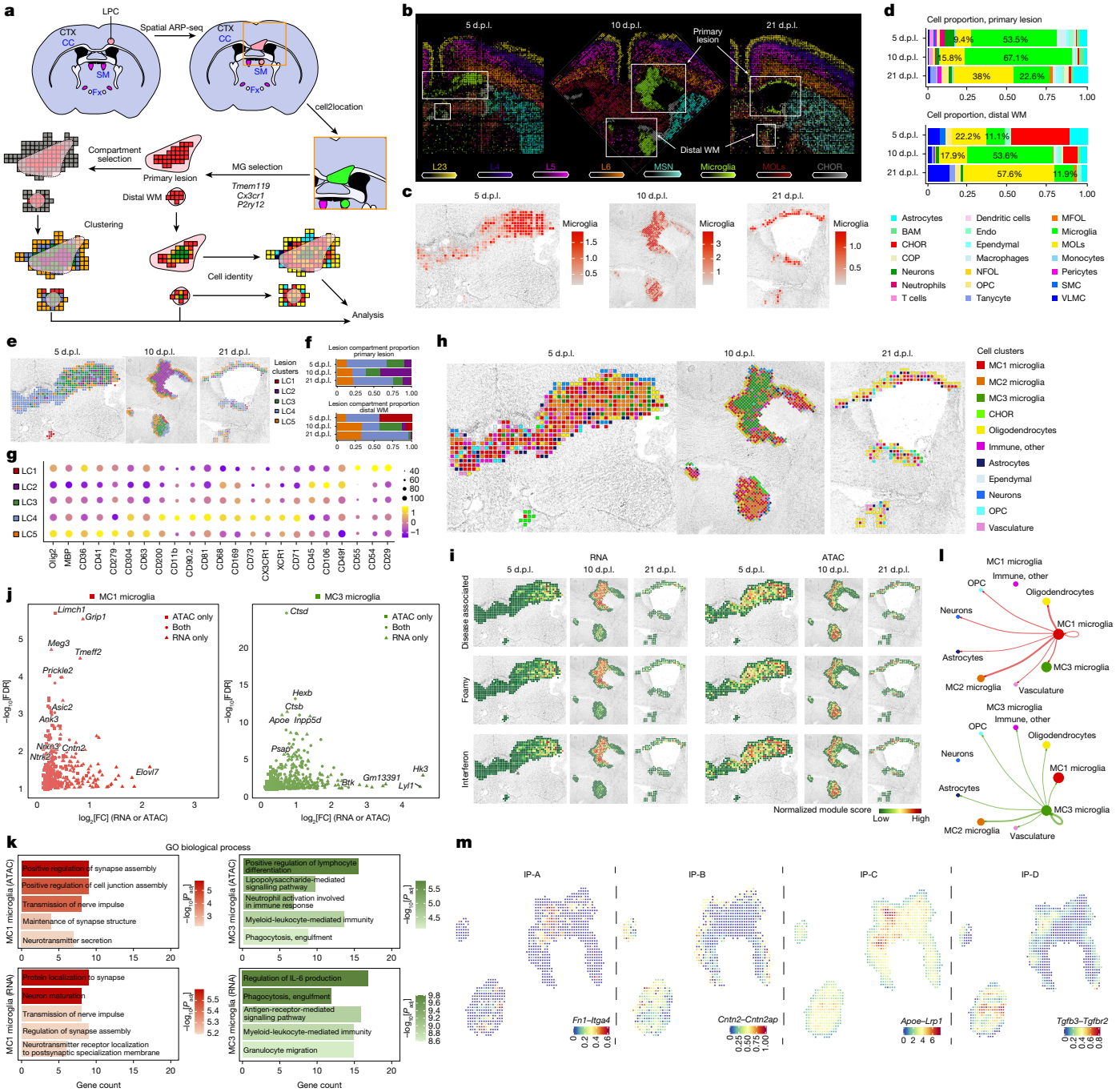

Fig. 6 | Microglial dynamics in the primary focal and distal lesion-like compartments. a, Schematic of the analysis workflow. **b**, Cell types[30,56] predicted by cell2location from 5, 10 and 21 d.p.l. mouse brains. **c**, The predicted spatial abundance of microglia as determined using cell2location in lesion-like compartments. **d**, The proportions of different cell types within lesion-like compartments in the primary lesion and distal WM, as shown in **c**. **e**, Unsupervised clustering of the lesion-like compartments in **c**. **f**, The proportions of different clusters from the primary lesion and distal WM in **e**. **g**, The expression level and the percentage of pixels from clusters LC1–5 for ADT protein data in spatial ARP-seq. **h**, Cell types and subclusters of microglia (MC1–3) in **e**. **i**, Spatial module scores of disease-associated, foamy and interferon microglial states based on RNA and ATAC data at 5, 10 and 21 d.p.l. in lesion-like compartments. Gene sets were based on a previous study[75]. **j**, The differential gene expression and GAS for the MC1 (left, red) and MC3 (right, green) microglial subclusters. **k**, GO analysis of microglial subclusters (MC1, left; MC3, right). Statistical analysis was performed using one-sided Fisher's exact tests with Benjamini–Hochberg adjustment for multiple comparisons. **l**, Communication networks of MC1 (top) and MC3 (bottom) microglia with other microglial subtypes and brain cell types, based on CellChat analysis. **m**, Representative spatial maps of ligand–receptor interaction strength for *Fn1–Itga4* (IP-A), *Cntn2–Cntnap2* (IP-B), *Apoe–Lrp1* (IP-C) and *Tgfb3–Tgfbr2* (IP-D), showing regional enrichment within lesion-like compartments at 10 d.p.l. CHOR, choroid plexus; Endo, endothelial cells, BAM, border-associated macrophages.

Our analysis suggests an association between cortical layer neuron maturation and oligodendroglial differentiation and myelination, both in the cortex and in the CC. We tracked the position of PNs and their postnatal development, successfully segregating axonogenesis and synaptogenesis in space and time. Notably, we detected RNA signatures of distinct cortical neuronal populations in specific regions of the CC, potentially reflecting the transport of mRNAs along developing axons to synaptic compartments, where they may carry out

specialized functions[78]. We propose that MOLs initially myelinate corticofugal PNs along the lateral CC and subsequently move medially to myelinate CPN tracts as they advance in their developmental program (Fig. 3n). Similar to previous reports[71], in the LPC model, we observed a population of microglia that expressed a canonical dendritic cell marker, *Itgax*. CD11c$^+$ microglia are integral to developmental myelin, and reparative in disease models[71]. In ageing and disease states (ischaemia, stroke, injury-associated Alzheimer's disease risk, amyotrophic lateral sclerosis and multiple sclerosis), the percentage of CD11c$^+$ microglia is variable depending on location and disease state. In development and multiple sclerosis models (experimental autoimmune encephalomyelitis; and cuprizone), CD11c$^+$ microglia have been associated with myelination-promoting mechanisms, including the secretion of insulin growth factor (IGF1)[79]. Consistent with a pro-repair role for CD11c$^+$ microglia, we observed increased numbers at 21 d.p.l., localized to the only region of the CC that had not yet been remyelinated.

Using CODEX and TRIC-DISCO, we were able to track distal macrophages/microglia that were populated along WM tracts both anterior and posterior to the lesion. Our observations are most probably not a consequence of mechanical injury resulting from injection induced injury as, in the tri-omics data (Fig. 5a–d), the inflammation is observed only at the primary lesion site and at the entry point of the needle at 5 d.p.l., with inflammation at the distal compartment occurring only at 10 d.p.l. Furthermore, monocyte-derived macrophage infiltration and microglial cellular augmentation are found exclusively within lesion area in mice with WM demyelination caused by LPC injection[80,81]. Comparison of the primary and distal inflammatory environments suggests that distal inflammation is probably delayed, as the primary lesion at 5 d.p.l. and the distal compartment at 10 d.p.l. show similar microglial cluster compositions. The immune attenuation observed only in distal WM may reflect unique features of distal propagation or indicate that comparable programs are active earlier in the primary lesion. Several mechanisms could drive distal macrophage/microglial spread, including ventricular transport of inflammatory cues, local activation by nearby cells or propagation along axonal tracts. T cells are unlikely to be major contributors, as they are not consistently abundant in regions of microglial expansion. Instead, microglia themselves probably shape the environment and promote low-level distal inflammation. Ventricular spread may contribute to the observed expansion in some regions, but it cannot account for all cases, as microglial expansion also occurs in non-periventricular areas. There is some evidence suggesting axonal propagation of inflammation, particularly along the visual pathway and optic nerve[82–86]. Given that the spread appears to follow WM tracts, a leading hypothesis is that neurons transmit inflammatory cues to distal sites.

By using CODEX, spatial tri-omic technologies and TRIC-DISCO, we show how multimodal spatial omics can identify aspects of brain development and disease. Recent advances, such as SPACE-seq[87] and ExIGS[88] are expanding the suite of spatial omics approaches. These and other technologies can be further used to explore additional regions of the CNS during development and neuroinflammation.

Online content

Any methods, additional references, Nature Portfolio reporting summaries, source data, extended data, supplementary information, acknowledgements, peer review information; details of author contributions and competing interests; and statements of data and code availability are available at https://doi.org/10.1038/s41586-025-09663-y.

1. Zhang, D. et al. Spatial epigenome-transcriptome co-profiling of mammalian tissues. *Nature* **616**, 113–122 (2023).
2. Greig, L. C., Woodworth, M. B., Galazo, M. J., Padmanabhan, H. & Macklis, J. D. Molecular logic of neocortical projection neuron specification, development and diversity. *Nat. Rev. Neurosci.* **14**, 755–769 (2013).
3. Di Bella, D. J. et al. Molecular logic of cellular diversification in the mouse cerebral cortex. *Nature* **595**, 554–559 (2021).
4. Kessaris, N. et al. Competing waves of oligodendrocytes in the forebrain and postnatal elimination of an embryonic lineage. *Nat. Neurosci.* **9**, 173–179 (2006).
5. Bayraktar, O. A., Fuentealba, L. C., Alvarez-Buylla, A. & Rowitch, D. H. Astrocyte development and heterogeneity. *Cold Spring Harb. Perspect. Biol.* **7**, a020362 (2014).
6. Lee, H.-G. et al. Disease-associated astrocyte epigenetic memory promotes CNS pathology. *Nature* **627**, 865–872 (2024).
7. Kukanja, P. et al. Cellular architecture of evolving neuroinflammatory lesions and multiple sclerosis pathology. *Cell* **187**, 1990–2009 (2024).
8. Patani, R., Hardingham, G. E. & Liddelow, S. A. Functional roles of reactive astrocytes in neuroinflammation and neurodegeneration. *Nat. Rev. Neurol.* **19**, 395–409 (2023).
9. Paolicelli, R. C. et al. Microglia states and nomenclature: A field at its crossroads. *Neuron* **110**, 3458–3483 (2022).
10. Kirby, L. & Castelo-Branco, G. Crossing boundaries: Interplay between the immune system and oligodendrocyte lineage cells. *Semin. Cell Dev. Biol.* https://doi.org/10.1016/j.semcdb.2020.10.013 (2020).
11. McNamara, N. B. et al. Microglia regulate central nervous system myelin growth and integrity. *Nature* **613**, 120–129 (2023).
12. Escartin, C. et al. Reactive astrocyte nomenclature, definitions, and future directions. *Nat. Neurosci.* **24**, 312–325 (2021).
13. Meijer, M. et al. Epigenomic priming of immune genes implicates oligodendroglia in multiple sclerosis susceptibility. *Neuron* **110**, 1193–1210 (2022).
14. Goltsev, Y. et al. Deep profiling of mouse splenic architecture with CODEX multiplexed imaging. *Cell* **174**, 968–981 (2018).
15. Liu, Y. et al. High-spatial-resolution multi-omics sequencing via deterministic barcoding in tissue. *Cell* **183**, 1665–1681 (2020).
16. Crick, F. Central dogma of molecular biology. *Nature* **227**, 561–563 (1970).
17. Wang, L. et al. Molecular and cellular dynamics of the developing human neocortex. *Nature* https://doi.org/10.1038/s41586-024-08351-7 (2025).
18. Fiorelli, R., Azim, K., Fischer, B. & Raineteau, O. Adding a spatial dimension to postnatal ventricular-subventricular zone neurogenesis. *Development* **142**, 2109–2120 (2015).
19. Marcy, G. et al. Single-cell analysis of the postnatal dorsal V-SVZ reveals a role for Bmpr1a signaling in silencing pallial germinal activity. *Sci. Adv.* **9**, eabq7553 (2023).
20. Lein, E. S. et al. Genome-wide atlas of gene expression in the adult mouse brain. *Nature* **445**, 168–176 (2007).
21. Rajan, W. D. et al. Defining molecular identity and fates of CNS-border associated macrophages after ischemic stroke in rodents and humans. *Neurobiol. Dis.* **137**, 104722 (2020).
22. Mrdjen, D. et al. High-dimensional single-cell mapping of central nervous system immune cells reveals distinct myeloid subsets in health, aging, and disease. *Immunity* **48**, 380–395 (2018).
23. van Tilborg, E. et al. Origin and dynamics of oligodendrocytes in the developing brain: Implications for perinatal white matter injury. *Glia* **66**, 221–238 (2018).
24. Hisaoka, T., Nakamura, Y., Senba, E. & Morikawa, Y. The forkhead transcription factors, Foxp1 and Foxp2, identify different subpopulations of projection neurons in the mouse cerebral cortex. *Neuroscience* **166**, 551–563 (2010).
25. Takahashi, K., Liu, F. C., Hirokawa, K. & Takahashi, H. Expression of Foxp4 in the developing and adult rat forebrain. *J. Neurosci. Res.* **86**, 3106–3116 (2008).
26. Ferland, R. J., Cherry, T. J., Preware, P. O., Morrisey, E. E. & Walsh, C. A. Characterization of Foxp2 and Foxp1 mRNA and protein in the developing and mature brain. *J. Comp. Neurol.* **460**, 266–279 (2003).
27. Ahmed, N. I. et al. Compensation between FOXP transcription factors maintains proper striatal function. *Cell Rep.* **43**, 114257 (2024).
28. Joglekar, A. et al. Single-cell long-read sequencing-based mapping reveals specialized splicing patterns in developing and adult mouse and human brain. *Nat. Neurosci.* **27**, 1051–1063 (2024).
29. Rosenberg, A. B. et al. Single-cell profiling of the developing mouse brain and spinal cord with split-pool barcoding. *Science* **360**, 176–182 (2018).
30. Wheeler, M. A. et al. MAFG-driven astrocytes promote CNS inflammation. *Nature* **578**, 593–599 (2020).
31. Li, Y. E. et al. An atlas of gene regulatory elements in adult mouse cerebrum. *Nature* **598**, 129–136 (2021).
32. Saitta, K. S. et al. CHPG enhances BDNF and myelination in cuprizone-treated mice through astrocytic metabotropic glutamate receptor 5. *Glia* **69**, 1950–1965 (2021).
33. Lee, S. K. et al. The LIM domain-only protein LMO4 is required for neural tube closure. *Mol. Cell. Neurosci.* **28**, 205–214 (2005).
34. McKenna, W. L. et al. Tbr1 and Fezf2 regulate alternate corticofugal neuronal identities during neocortical development. *J. Neurosci.* **31**, 549–564 (2011).
35. Deng, Y. et al. Spatial-CUT&Tag: spatially resolved chromatin modification profiling at the cellular level. *Science* **375**, 681–686 (2022).
36. Falcão, A. M. et al. Disease-specific oligodendrocyte lineage cells arise in multiple sclerosis. *Nat. Med.* **24**, 1837–1844 (2019).
37. Marques, S. et al. Oligodendrocyte heterogeneity in the mouse juvenile and adult central nervous system. *Science* **352**, 1326–1329 (2016).
38. Spitzer, S. O. et al. Oligodendrocyte progenitor cells become regionally diverse and heterogeneous with age. *Neuron* **101**, 459–471 (2019).
39. Miskic, T., Kostovic, I., Rasin, M. R. & Krsnik, Z. Adult upper cortical layer specific transcription factor CUX2 is expressed in transient subplate and marginal zone neurons of the developing human brain. *Cells* **10**, 415 (2021).
40. Semple, B. D., Blomgren, K., Gimlin, K., Ferriero, D. M. & Noble-Haeusslein, L. J. Brain development in rodents and humans: Identifying benchmarks of maturation and vulnerability to injury across species. *Prog. Neurobiol.* **106–107**, 1–16 (2013).
41. Craig, A. et al. Quantitative analysis of perinatal rodent oligodendrocyte lineage progression and its correlation with human. *Exp. Neurol.* **181**, 231–240 (2003).
42. Sturrock, R. R. Myelination of the mouse corpus callosum. *Neuropathol. Appl. Neurobiol.* **6**, 415–420 (1980).

43. Vincze, A., Mazlo, M., Seress, L., Komoly, S. & Abraham, H. A correlative light and electron microscopic study of postnatal myelination in the murine corpus callosum. *Int. J. Dev. Neurosci.* **26**, 575–584 (2008).
44. Hilscher, M. M. et al. Spatial and temporal heterogeneity in the lineage progression of fine oligodendrocyte subtypes. *BMC Biol.* **20**, 122 (2022).
45. Dawson, M. R., Polito, A., Levine, J. M. & Reynolds, R. NG2-expressing glial progenitor cells: an abundant and widespread population of cycling cells in the adult rat CNS. *Mol. Cell. Neurosci.* **24**, 476–488 (2003).
46. Bergles, D. E. & Richardson, W. D. Oligodendrocyte development and plasticity. *Cold Spring Harb. Perspect. Biol.* **8**, a020453 (2015).
47. Lubetzki, C., Sol-Foulon, N. & Desmazières, A. Nodes of Ranvier during development and repair in the CNS. *Nat. Rev. Neurol.* **16**, 426–439 (2020).
48. Zhang, A. et al. Neurofascin 140 is an embryonic neuronal neurofascin isoform that promotes the assembly of the node of Ranvier. *J. Neurosci.* **35**, 2246–2254 (2015).
49. Vabnick, I. & Shrager, P. Ion channel redistribution and function during development of the myelinated axon. *J. Neurobiol.* **37**, 80–96 (1998).
50. Rios, J. C. et al. Contactin-associated protein (Caspr) and contactin form a complex that is targeted to the paranodal junctions during myelination. *J. Neurosci.* **20**, 8354–8364 (2000).
51. Liu, J. et al. FOXG1 sequentially orchestrates subtype specification of postmitotic cortical projection neurons. *Sci. Adv.* **8**, eabh3568 (2022).
52. Alcamo, E. A. et al. Satb2 regulates callosal projection neuron identity in the developing cerebral cortex. *Neuron* **57**, 364–377 (2008).
53. Deck, M. et al. Pathfinding of corticothalamic axons relies on a rendezvous with thalamic projections. *Neuron* **77**, 472–484 (2013).
54. Rodriguez-Tornos, F. M. et al. Cux1 enables interhemispheric connections of layer II/III neurons by regulating kv1-dependent firing. *Neuron* **89**, 494–506 (2016).
55. Mizuno, H., Hirano, T. & Tagawa, Y. Pre-synaptic and post-synaptic neuronal activity supports the axon development of callosal projection neurons during different post-natal periods in the mouse cerebral cortex. *Eur. J. Neurosci.* **31**, 410–424 (2010).
56. Yao, Z. et al. A high-resolution transcriptomic and spatial atlas of cell types in the whole mouse brain. *Nature* **624**, 317–332 (2023).
57. Baydyuk, M. et al. Tracking the evolution of CNS remyelinating lesion in mice with neutral red dye. *Proc. Natl Acad. Sci. USA* **116**, 14290–14299 (2019).
58. Miron, V. E. et al. M2 microglia and macrophages drive oligodendrocyte differentiation during CNS remyelination. *Nat. Neurosci.* **16**, 1211–1218 (2013).
59. Bieber, A. J., Kerr, S. & Rodriguez, M. Efficient central nervous system remyelination requires T cells. *Ann. Neurol.* **53**, 680–684 (2003).
60. Dombrowski, Y. et al. Regulatory T cells promote myelin regeneration in the central nervous system. *Nat. Neurosci.* **20**, 674–680 (2017).
61. Rothlein, R., Dustin, M. L., Marlin, S. D. & Springer, T. A. A human intercellular adhesion molecule (ICAM-1) distinct from LFA-1. *J. Immunol.* **137**, 1270–1274 (1986).
62. Hubbard, A. K. & Rothlein, R. Intercellular adhesion molecule-1 (ICAM-1) expression and cell signaling cascades. *Free Radic. Biol. Med.* **28**, 1379–1386 (2000).
63. Terada, N. et al. The tetraspanin protein, CD9, is expressed by progenitor cells committed to oligodendrogenesis and is linked to β1 integrin, CD81, and Tspan-2. *Glia* **40**, 350–359 (2002).
64. Jurga, A. M., Paleczna, M. & Kuter, K. Z. Overview of general and discriminating markers of differential microglia phenotypes. *Front. Cell. Neurosci.* **14**, 198 (2020).
65. Jones, B. A., Beamer, M. & Ahmed, S. Fractalkine/CX3CL1: a potential new target for inflammatory diseases. *Mol. Interv.* **10**, 263–270 (2010).
66. Slavik, J. M., Hutchcroft, J. E. & Bierer, B. E. CD28/CTLA-4 and CD80/CD86 families. *Immunol. Res.* **19**, 1–24 (1999).
67. Dai, X.-M. et al. Targeted disruption of the mouse colony-stimulating factor 1 receptor gene results in osteopetrosis, mononuclear phagocyte deficiency, increased primitive progenitor cell frequencies, and reproductive defects. *Blood* **99**, 111–120 (2002).
68. Butovsky, O. et al. Modulating inflammatory monocytes with a unique microRNA gene signature ameliorates murine ALS. *J. Clin. Invest.* **122**, 3063–3087 (2012).
69. Konishi, H. et al. Siglec-H is a microglia-specific marker that discriminates microglia from CNS-associated macrophages and CNS-infiltrating monocytes. *Glia* **65**, 1927–1943 (2017).
70. Arnoux, I. & Audinat, E. Fractalkine signaling and microglia functions in the developing brain. *Neural Plast.* **2015**, 689404 (2015).
71. Wlodarczyk, A. et al. A novel microglial subset plays a key role in myelinogenesis in developing brain. *EMBO J.* **36**, 3292–3308 (2017).
72. Nemes-Baran, A. D., White, D. R. & DeSilva, T. M. Fractalkine-dependent microglial pruning of viable oligodendrocyte progenitor cells regulates myelination. *Cell Rep.* **32**, 108047 (2020).
73. Kanatani, S. et al. Whole-brain spatial transcriptional analysis at cellular resolution. *Science* **386**, 907–915 (2024).
74. Shimizu, Y., van Seventer, G. A., Horgan, K. J. & Shaw, S. Costimulation of proliferative responses of resting CD4+ T cells by the interaction of VLA-4 and VLA-5 with fibronectin or VLA-6 with laminin. *J. Immunol.* **145**, 59–67 (1990).
75. Androvic, P. et al. Spatial transcriptomics-correlated electron microscopy maps transcriptional and ultrastructural responses to brain injury. *Nat. Commun.* **14**, 4115 (2023).
76. Hammond, T. R. et al. Single-cell RNA sequencing of microglia throughout the mouse lifespan and in the injured brain reveals complex cell-state changes. *Immunity* **50**, 253–271 (2019).
77. de Castro, F. Cajal and the Spanish Neurological School: neuroscience would have been a different story without them. *Front. Cell. Neurosci.* **13**, 187 (2019).
78. Ma, H. et al. Excitation-transcription coupling, neuronal gene expression and synaptic plasticity. *Nat. Rev. Neurosci.* **24**, 672–692 (2023).
79. Myhre, C. L. et al. Microglia express insulin-like growth factor-1 in the hippocampus of aged APP(swe)/PS1(ΔE9) transgenic mice. *Front. Cell. Neurosci.* **13**, 308 (2019).
80. Lloyd, A. F. et al. Central nervous system regeneration is driven by microglia necroptosis and repopulation. *Nat. Neurosci.* **22**, 1046–1052 (2019).
81. Dolan, M.-J. et al. Spatiotemporal analysis of remyelination reveals a concerted interferon-responsive glial state that coordinates immune infiltration. Preprint at *bioRxiv* https://doi.org/10.1101/2025.04.22.649486 (2025).
82. Buren, J. M. V. Trans-synaptic retrograde degeneration in the visual system of primates. *J. Neurol. Neurosurg. Psychiatry* **26**, 402–409 (1963).
83. Rocca, M. A. et al. Wallerian and trans-synaptic degeneration contribute to optic radiation damage in multiple sclerosis: a diffusion tensor MRI study. *Mult. Scler.* **19**, 1610–1617 (2013).
84. Reich, D. S. et al. Damage to the optic radiation in multiple sclerosis is associated with retinal injury and visual disability. *Arch. Neurol.* **66**, 998–1006 (2009).
85. Tur, C. et al. Longitudinal evidence for anterograde trans-synaptic degeneration after optic neuritis. *Brain* **139**, 816–828 (2016).
86. Al-Louzi, O., Button, J., Newsome, S. D., Calabresi, P. A. & Saidha, S. Retrograde trans-synaptic visual pathway degeneration in multiple sclerosis: a case series. *Mult. Scler. J.* **23**, 1035–1039 (2017).
87. Huang, Y.-H. et al. Unified molecular approach for spatial epigenome, transcriptome, and cell lineages. *Proc. Natl Acad. Sci. USA* **122**, e2424070122 (2025).
88. Labade, A. S. et al. Expansion in situ genome sequencing links nuclear abnormalities to aberrant chromatin regulation. *Science* **389**, eadt2781 (2025).

Methods

Animals

This study followed some applicable aspects of the PREPARE[89] planning guidelines checklist, such as the formulation of the in vivo study, dialogue between scientists and the animal facility, and quality control of the in vivo components in the study. All animals were born, bred and housed at the Karolinska Institutet, Comparative Medicine Biomedicum animal facility (KMB). Mouse brain tissues (postnatal days P0, P2, P5, P7, P10 and P21) were obtained from a mouse line generated by crossing *Sox10:cre* animals (The Jackson Laboratory, 025807) on the C57BL/6j genetic background with *RCE:loxP* (eGFP) animals (The Jackson Laboratory, 32037-JAX) on a C57BL/6xCD1 mixed genetic background. Females with a hemizygous *cre* allele were mated with males lacking the *cre* allele, while the reporter allele was kept in hemizygosity in both females and males. In the resulting *Sox10:cre-RCE:loxP* (eGFP) progeny, the entire OL lineage was labelled with eGFP.

None of the experimental animals in this study were subjected to previous procedures before enrolment in the study. All of the animals were free from mouse viral pathogens, ectoparasites, endoparasites and mouse bacterial pathogens. Mice were kept under the following light–dark cycle: dawn, 6:00–7:00; daylight, 7:00–18:00; dusk, 18:00–19:00; night, 19:00–6:00; a maximum number of 5 mice were housed per cage in individually ventilated cages (IVC Sealsafe plus GM500, Tecniplast). General housing parameters such as relative humidity, temperature and ventilation follow the European Convention for the Protection of Vertebrate Animals used for experimental and other scientific purposes treaty ETS 123, Strasbourg 18.03.1996/01.01.1991. In brief, consistent relative air humidity of 55 ± 10% was maintained at 22 °C and the air quality was controlled with the use of stand-alone air handling units supplemented with HEPA filtrated air. Monitoring of husbandry parameters was done using ScanClime (Scanbur) units. Cages contained hardwood bedding (TAPVEI), nesting material, shredded paper, gnawing sticks and card box shelter (Scanbur). The mice received a regular chow diet (CRM(P) SDS and CRM(P), SAFE). Water was provided by using a water bottle, which was changed weekly. The cages were changed every other week. Cage changes were done in a laminar air-flow cabinet (NinoSafe MCCU mobile cage changing unit) with a HEPA H14 EN1822 filter (0.3 µm particle size). Facility personnel wore dedicated scrubs, socks and shoes. Respiratory masks were used when working outside of the laminar air-flow cabinet. Both sexes were included in the study. Randomization was performed to assign samples to time-point groups.

All experimental procedures on animals were performed following the European directive 2010/63/EU, local Swedish directive L150/SJVFS/2019:9, Saknr L150, Karolinska Institutet complementary guidelines for procurement and use of laboratory animals, Dnr. 1937/03-640 and Karolinska Institutet Comparative Medicine veterinary guidelines and plans (version 2020/12/18). The procedures described were approved by the regional committee for ethical experiments on laboratory animals in Sweden (Stockholm Norra Djurförsöksetiska Nämnd, 1995/2019 and 7029/2020).

Tissue and slide preparation

For all postnatal collection points except for P21, we performed a decapitation and extracted the brain, immediately placing the tissue in Tissue Tek O.C.T. compound over a bath of dry ice and 70% ethanol. For all mice older than P21 we anaesthetized the mice and then performed a transcardiac perfusion with gassed, ice-cold artificial cerebral spinal fluid. Next, we decapitated the mice and removed the brain and followed the same embedding procedure as for the neonates.

All tissues were stored at −80 °C until further usage. Fresh 50 × 75 mm (Ted Pella, NC1811932) 0.01% poly-L-lysine-coated (Sigma-Aldrich, P1524-100) slides were prepared and stored at 4 °C and used within 1 week for mounting tissue. For brain tissue sectioning, the tissue was incubated for 30 min in the cryostat chamber at −20 °C. The slides were simultaneously precooled (poly-L-lysine coated for DBiT and charged Superfrost Plus (Eprendia, 4951PLUS-001) for CODEX) and kept in the cryostat for the entire procedure. The sections were cut using an antiroll plate, to a thickness of 10 µm. Tissue collection was done by placing the cold slide in the correct position on top of the tissue then placing over a gloved backhand until the tissue was fully bound. The slide was immediately placed back in the cryostat chamber until sectioning was complete, at which point all slides were stored at −80 °C.

LPC mouse model (1% LPC injection)

Sox10:cre-RCE:loxP (eGFP) mice of mixed sex, at around P85, were used in the LPC study. In brief, under an aseptic technique, mice received an intraperitoneal injection of a non-steroidal anti-inflammatory analgesic (Carprofen; 5 mg kg^{-1}), and were then deeply anaesthetized with isoflurane; an ophthalmic ointment was then applied in both eyes to prevent corneal desiccation, and the mouse was placed over a warm pad for the entire procedure to prevent hypothermia. The site of the incision was shaved and sanitized with 2% chlorhexidine before cutting a 0.5 cm incision with a scalpel to expose the cranium. Using a stereotaxic frame, the rough coordinates of −0.8 mm posterior and 0.8 mm lateral were measured for a skull drilling perforation. After completing, the 1% LPC solution was loaded into a pulled-glass micropipette and the coordinates were recalculated. The micropipette was then slowly inserted 1.3 mm deep (CC below cingulum bundle). The 2 µl injection was performed using an injection speed of 5 nl s^{-1}. After the injection was complete the micropipette was kept in place for an additional 5 min to prevent efflux and then slowly pulled out of the brain. Monitoring of reflexes, respiratory rate and breathing pattern was performed during the entire surgical procedure. The skin was sutured with a non-absorbable suture (Vicryl, Ethicon), and the mouse was observed until regaining full consciousness and mobility. Post-operative care was administered daily for the next 72 h. Mice were euthanized at 5, 10 and 21 days after surgery using the sampling procedure and sample collection method as for the P21 mice (above).

Retro-AAV-eGFP injection

P1 mice were injected with 0.5 µl of retro-AAV-eGFP virus (ssAAV-retro/2-CAG-eGFP-WPRE-SV40p(A); V24-retro; produced at the Universität Zürich Viral Vector Facility) into either layer II/III of the CTX (1.5 mm anterior of lambda, 0.7 mm lateral of midline and 0.5 mm deep from skin) or the thalamus (1.5 mm anterior of lambda, 1.6 mm lateral of midline and 2.8 mm deep). In brief, neonates received a subcutaneous injection buprenorphine (0.5 mg kg^{-1}) and, after 30 min, the neonates were put under general anaesthesia using isoflurane. The bregma coordinates were found, and a pulled-glass capillary preloaded with virus and mineral oil was inserted to the desired depth before injection of virus into the parenchyma at a rate of 100 nl min^{-1}. After the injection, the glass capillary was kept in place for an additional 5 min before it was slowly withdrawn. The neonate's foot was tattooed, and the neonates were then acclimatized back to the mother by rubbing bedding on the pup to prevent maternal rejection. The neonates were monitored to verify that they successfully came out of anaesthesia. Daily monitoring and pain assessments were performed until euthanization at P10. Mice were perfused with cold PBS followed by 4% PFA (3–5 ml each) and tissue was incubated overnight in 4% PFA and then transferred to 30% sucrose for 2–3 days. Finally, the brain tissue was cryosectioned at a thickness of 20 µm, stained with anti-rat MBP (EMD Millipore, MAB 386) antibodies and both eGFP and Alexa Fluor 555 were imaged using a Zeiss LSM900-Airy using *z* stacking. Blinded imaging analysis was performed by first creating a maximum-projection image for each channel; the MBP area was drawn for each image then the percentage area of MBP, retro-AAV-eGFP and the dual overlap percentage area was measured. To compare the extent of myelination for each labelled tract, we calculated the area under the curve across the entire CC (percentage area of the

CC that was eGFP and MBP positive) then performed a two-tailed *t*-test using the total mean area of MBP and standard error values that were generated through the area under the curve calculation. Experimental blinding was implemented during retro-AAV-eGFP image analysis.

Tris-mediated retention of in situ hybridization signal during clearing DISCO

Three *Sox10:cre-RCE:loxP* (eGFP) mice (aged 8–10 weeks) were stereotactically injected with 1% LPC and euthanized 5 days after the procedure, as described above except that a 4% PFA perfusion was included directly after the artificial cerebrospinal fluid. Each brain was carefully extracted and then stored overnight in 4% PFA at 4 °C before processing through the full TRIC-DISCO protocol[73]. In brief, a methanol gradient (60%, 80%, 100%, 100%) was done and then stored overnight at −20 °C. Successive steps to delipidate (100% dichloromethane), wash and bleach (100% methanol + 5% hydrogen peroxide) were done with overnight incubations at 4 °C. For whole-brain in situ hybridization chain reaction, the samples were incubated with 50% formamide wash buffer until brain sinking, followed by incubation for 3 days at 37 °C in 50% hybridization buffer with *Csf1r* DNA probe (1.6 pmol of probe in 400 µl). The samples were then washed three times in 5× saline-sodium citrate (5× SSC) buffer with Tween-20 (5× SSCT), incubated in amplification buffer overnight (room temperature), and then washed three times in 5× SSCT buffer. Tris-mediated signal retention involved three wash steps (for 1 h at room temperature) in 500 mM of Tris-HCl, sample dehydration in 100% methanol (1 h at room temperature) then dehydration and delipidation in 66% DCM and 33% methanol (3 h) and finally two washes with 100% DCM. To promote tissue transparency an overnight dibenzl ether (DBE) incubation was performed with one DBE solution change. Whole-brain light-sheet microscopy using LaVision Ultramicroscope II (MiltenyBiotec) provided images that were used in the study.

Human samples and slide preparation

De-identified human tissue samples from the second trimester were collected at Zuckerberg San Francisco General Hospital (ZSFGH), with the acquisition approved by the UCSF Human Gamete, Embryo and Stem Cell Research Committee (10-05113). All of the procedures adhered to protocol guidelines, and informed consent was obtained before sample collection and use for this study. The de-identified third-trimester and early postnatal tissues without known neurological disorders were obtained from the University of Maryland Brain and Tissue Bank through NIH NeuroBioBank under the bank's Institutional Review Boards oversight. For all samples, coronal cryosections of 10 µm were prepared on poly-L-lysine-coated glass slides (63478-AS, Electron Microscopy Sciences) or 50 × 75 mm poly-L-lysine-coated glass slides, and stored at −80 °C for subsequent use.

Multiplex immunofluorescence imaging (CODEX)

Immunofluorescence imaging was conducted using the Akoya Biosciences PhenoCycler system, which is integrated with a Keyence BZ-X800 epifluorescence microscope. The protocol for antibody–barcode conjugation, staining and imaging fresh-frozen tissue, as described in the manufacturer's user manual, was strictly adhered to. Antibodies and detailed information are listed in Supplementary Tables 6 and 13. As CODEX images vary in magnification, the group's post-acquisition exposure settings are uniform for each magnification within a figure. All post-acquisition processing was performed using QuPath[90]. Batch-to-batch (S1 and S2) variation correction for the exposure settings for each antibody channel was adjusted by performing mean intensity measurements over one hemisphere using ImageJ[91] until the mean intensities aligned between the exposure settings.

DNA barcodes sequences, DNA oligos and other key reagents

DNA oligos used for transposome assembly, PCR and library construction are shown in Supplementary Table 1. All of the DNA barcode are provided in Supplementary Tables 2 and 3, and all other chemicals and reagents were listed in Supplementary Table 6. The hydrogel-based DBiT devices preloaded with 220 barcodes were purchased from AtlasXomics (AXO-0457).

Spatial ARP-seq

The fresh-frozen tissue slide was thawed for 10 min before fixing with 0.2% formaldehyde with 0.05 U μl^{-1} RNase inhibitor (RI) and quenching with 1.25 M glycine for 5 min. After three washes with 0.5× DPBS-RI, the tissue section was permeabilized with lysis buffer for 15 min, followed by another two washes with 0.5× DPBS-RI and a final wash with deionized H_2O. The ADT cocktails (diluted 20 times from the original stock) from BioLegend and self-conjugated antibodies (including intracellular and surface proteins for mouse brain) were added and incubated for 3 h at 4 °C. The mouse ADT protein panel encompasses 119 antibodies targeting cell surface antigens, 9 isotype control antibodies specific to immune cells and, optionally, 8 self-conjugated antibodies for intracellular markers representative of canonical mouse brain cell types (Supplementary Table 4). Similarly, the human ADT panel includes 154 antibodies against unique cell surface antigens, covering key lineage antigens, complemented by nine isotype control antibodies for immune cell profiling (Supplementary Table 5). The ADT cocktail was removed by washing three times with 0.5× DPBS-RI. The tissue was then washed for 5 min with a lysis buffer containing 0.001% Digitonin, 10 mM Tris-HCl (pH 7.4), 3 mM $MgCl_2$, 0.01% NP-40, 1% BSA, 10 mM NaCl, 0.05 U μl^{-1} RNase inhibitor and 0.01% Tween-20. Subsequently, it was washed twice for 5 min each with a wash buffer composed of 0.1% Tween-20, 1% BSA, 10 mM Tris-HCl (pH 7.4), 3 mM $MgCl_2$ and 10 mM NaCl. A transposition mix was prepared consisting of 5 µl homemade transposome, 50 µl 2× Tagmentation buffer, 33 µl 1× DPBS, 1 µl 1% Digitonin, 0.05 U μl^{-1} RNase inhibitor, 10 µl nuclease-free H_2O and 1 µl 10% Tween-20. This mixture was then added to the sample and incubated at 37 °C for 30 min. Next, 40 mM EDTA containing 0.05 U μl^{-1} RNase inhibitor was added and incubated for 5 min at room temperature to halt the transposition process. Subsequently, the tissue section was washed three times with 0.5× PBS-RI for 5 min each. The RT mixture consisting of 3.1 µl 10 mM dNTPs each, 4.5 µl RNase-free water, 0.4 µl RNase inhibitor, 12.5 µl 5× RT buffer, 6.2 µl Maxima H Minus reverse transcriptase, 0.8 µl SuperaseIn RNase inhibitor, 10 µl RT primer and 25 µl 0.5× PBS-RI was added to the tissue. The tissue was then incubated for 30 min at room temperature and subsequently at 42 °C for 90 min in a humidified chamber. After the reverse transcription reaction, the tissue was washed for 5 min with 1× NEBuffer 3.1 containing 1% RNase inhibitor.

For the first in situ ligation of barcodes (barcodes A), the PDMS chip was positioned over the region of interest (ROI) on the tissue slide. To ensure proper alignment, a bright-field image was captured using a ×10 objective on the Thermo Fisher Scientific EVOS FL Auto microscope (AMF7000) with EVOS FL Auto 2 Software Revision v.2.0.2094.0. The PDMS device and tissue slide were then securely fastened using a homemade clamp. Initially, barcode A was combined with ligation linker 1: 10 µl of 100 µM ligation linker, 10 µl of 100 µM each barcode A and 20 µl of 2× annealing buffer (2 mM EDTA, 100 mM NaCl, 20 mM Tris, pH 7.5–8.0) were thoroughly mixed. For each channel, a ligation master mixture was prepared, containing 2 µl of ligation mix (11 µl T4 DNA ligase, 72.4 µl RNase-free water, 27 µl T4 DNA ligase buffer, 5.4 µl 5% Triton X-100), 2 µl of 1× NEBuffer 3.1 and 1 µl of each annealed DNA barcode A (A1–100, 25 µM). The ligation master mixture was loaded into 100 channels of the device using a vacuum. The device was then incubated at 37 °C for 30 min in a humidified chamber. After the incubation, the PDMS chip and clamp were removed after a 5-min wash with 1× NEBuffer 3.1. The slide was subsequently washed with water and then air-dried.

For the second in situ ligation of barcodes (barcodes B), the second PDMS chip was placed over the slide. A bright-field image was captured using a 10× objective for alignment purposes. The PDMS device and

tissue slide were securely clamped together using a clamp. The annealing of barcodes B (B1–100, 25 μM) and the preparation of the ligation master mix were performed identically to as described for barcodes A. The device was then incubated at 37 °C for 30 min in a humidified chamber. After incubation, the PDMS chip and clamp were removed after a 5-min wash with 1× DPBS containing SUPERase In RNase inhibitor. The slide was then rinsed with water and air-dried. A bright-field image was taken afterwards to assist with further alignment.

The ligation of barcodes A and B for the 220 × 220 barcode chips was performed according to the manufacturer's protocol (AXO-0457).

After the barcoding process, the ROI on the tissue was treated with a reverse-crosslinking mixture containing 1 mM EDTA, 0.4 mg ml^{-1} proteinase K, 50 mM Tris-HCl (pH 8.0), 1% SDS and 200 mM NaCl. This mixture was incubated at 58 °C for 2 h in a humidified chamber. The lysate was then transferred to a 1.5 ml tube and incubated at 65 °C overnight.

To separate DNA and cDNA, the lysate was purified using the Zymo DNA Clean & Concentrator-5 kit and then eluted into 100 μl of RNase-free water. The Dynabeads MyOne Streptavidin C1 beads (40 μl) were washed three times using 1× B&W buffer containing 0.05% Tween-20. The beads were then resuspended in 100 μl of 2× B&W buffer with 2.5 μl of SUPERase In RNase inhibitor. This bead suspension was then mixed with the lysate and allowed to bind at room temperature for 1 h with agitation. Finally, a magnet was used to separate the beads from the supernatant in the lysate.

The supernatant was processed for ATAC–seq library construction and purified using the Zymo DNA Clean & Concentrator-5 kit, then eluted into 20 μl of RNase-free water. For the PCR, 2.5 μl of 25 μM indexed i7 primer, 25 μl of 2× NEBNext Master Mix and 2.5 μl of 25 μM P5 PCR primer were added and thoroughly mixed. The initial PCR program was set as follows: 72 °C for 5 min; 98 °C for 30 s; followed by 5 cycles of 98 °C for 10 s, 63 °C for 30 s and 72 °C for 1 min. To determine the need for additional cycles, 5 μl of the pre-amplified mixture was combined with a quantitative PCR (qPCR) solution consisting of 0.5 μl of 25 μM new P5 PCR primer, 5 μl 2× NEBNext Master Mix, 3.76 μl nuclease-free water, 0.24 μl 25× SYBR Green and 0.5 μl of 25 μM indexed i7 primer. The qPCR reaction was then performed using the following program: 98 °C for 30 s; followed by 20 cycles of 98 °C for 10 s, 63 °C for 30 s and 72 °C for 1 min. On the basis of the qPCR results, the remaining 45 μl of pre-amplified DNA was further amplified for additional cycles until it reached one-third of the saturation signal. The final PCR product was then purified using 45 μl of 1× Ampure XP beads and eluted in 20 μl of nuclease-free water.

The beads were used to construct cDNA libraries. Initially, they were washed twice with 400 μl of 1× B&W buffer containing 0.05% Tween-20 and then once with 10 mM Tris (pH 8.0) with 0.1% Tween-20. The Streptavidin beads, with cDNA molecules bound, were resuspended in a TSO solution composed of 44 μl of 5× Maxima RT buffer, 22 μl of 10 mM dNTPs, 44 μl of 20% Ficoll PM-400 solution, 5.5 μl of RNase inhibitor, 5.5 μl of 100 μM template switch primer, 88 μl of RNase-free water, and 11 μl of Maxima H Minus reverse transcriptase. The beads were incubated at room temperature for 30 min and then at 42 °C for 90 min with gentle shaking. Next, the beads were washed once with 10 mM Tris containing 0.1% Tween-20 and once with water, then resuspended in a PCR solution consisting of 91.9 μl of RNase-free water, 8.8 μl of 10 μM each of primers 1 and 2, 0.5 μl of 1 μM primer 2-citeseq and 110 μl of 2× Kapa HiFi HotStart Master Mix. PCR thermocycling was conducted with an initial denaturation at 95 °C for 3 min, followed by 5 cycles of 98 °C for 20 s, 65 °C for 45 s and 72 °C for 3 min. After the initial five cycles, the Dynabeads MyOne Streptavidin C1 beads were removed from the PCR solution and 25× SYBR Green was added at a 1× concentration. The samples were then subjected to further qPCR with the programme set at 95 °C for 3 min, cycled at 98 °C for 20 s, 65 °C for 20 s, and 72 °C for 3 min for 15 cycles, with a final extension at 72 °C for 5 min. The reaction was terminated once the qPCR signal began to plateau.

To differentiate and purify cDNAs derived from mRNA and ADT, we used 0.6× SPRI beads according to the standard protocol. We mixed 120 μl of SPRI beads with 200 μl of the PCR product solution and allowed the mixture to incubate for 5 min. The supernatant, which contained the ADT-derived cDNAs, was then transferred to a 1.5 ml Eppendorf tube. The beads remaining in the original container were washed with 85% ethanol for 30 s and eluted in RNase-free water over 5 min. The mRNA-derived cDNAs were subsequently quantified using Qubit and BioAnalyzer. For further purification of the supernatant, we added 1.4× SPRI beads and incubated for 10 min. These beads were cleaned once with 80% ethanol and resuspended in 50 μl of water. An additional purification step was conducted by adding 100 μl of 2× SPRI beads and incubating for another 10 min. After two washes with 80% ethanol, the ADT-derived cDNAs were finally eluted with 50 μl of RNase-free water.

The sequencing libraries for the two types of cDNA products were constructed separately. For the mRNA library, we used the Nextera XT Library Prep Kit. We began by diluting 1 ng of purified cDNA in RNase-free water to a final volume of 5 μl. We then added 10 μl of Tagment DNA buffer and 5 μl of Amplicon Tagment Mix, and incubated the mixture at 55 °C for 5 min. Next, 5 μl of NT buffer was added and the mixture was incubated at room temperature for another 5 min. The PCR master solution, consisting of 15 μl PCR master mix, 1 μl of 10 μM P5 primer, 1 μl of 10 μM indexed P7 primer and 8 μl RNase-free water, was then added. The PCR was then conducted with the following programme: an initial denaturation at 95 °C for 30 s; followed by 12 cycles of 95 °C for 10 s, 55 °C for 30 s, 72 °C for 30 s and a final extension at 72 °C for 5 min. The PCR product was purified using 0.7× Ampure XP beads to obtain the final library.

For the ADT cDNAs, the library was constructed using PCR. In a PCR tube, 45 μl of the ADT cDNA solution was mixed with 10 μM 2.5 μl of P5 index, 2.5 μl of a 10 μM customized i7 index and 50 μl of 2× KAPA HiFi PCR Master Mix. The PCR conditions were set as follows: an initial denaturation at 95 °C for 3 min, followed by six cycles of denaturation at 95 °C for 20 s; annealing at 60 °C for 30 s; extension at 72 °C for 20 s; and a final extension at 72 °C for 5 min. The PCR product was then purified using 1.6× SPRI beads.

The size distribution and concentration of the library were analysed using the Agilent Bioanalyzer High Sensitivity Chip before sequencing. Next-generation sequencing (NGS) was then performed using the Illumina NovaSeq 6000 sequencer in paired-end 150 bp mode.

Spatial CTRP-seq

Tissue slide preparation and antibody incubation were performed according to the same protocol as used in the spatial ARP-seq method. After these initial steps, the tissue was washed twice with wash buffer (0.5 mM spermidine, 150 mM NaCl, one tablet of protease inhibitor cocktail, 20 mM HEPES, pH 7.5) and was subsequently incubated in NP40-Digitonin wash buffer (0.01% NP40, 0.01% Digitonin, 0.5 mM spermidine, 150 mM NaCl, one tablet of protease inhibitor cocktail, 20 mM HEPES pH 7.5) for 5 min, followed by three washes with 0.5× DPBS-RI. The section was then washed with wash buffer (0.5 mM spermidine, 150 mM NaCl, one tablet of protease inhibitor cocktail, 20 mM HEPES pH 7.5). The primary antibody was diluted 1:50 in antibody buffer (2 mM EDTA, 0.001% BSA, in NP40-Digitonin wash buffer) and applied to the tissue, which was then incubated overnight at 4 °C. The secondary antibody (guinea pig anti-rabbit IgG), diluted 1:50 in NP40-Digitonin wash buffer, was then added and incubated for 30 min at room temperature. The tissue was washed with wash buffer for 5 min. Next, a 1:100 dilution of the pA-Tn5 adapter complex in 300-wash buffer (20 mM HEPES pH 7.5, 300 mM NaCl, one tablet of protease inhibitor cocktail, 0.5 mM spermidine) was added and incubated at room temperature for 1 h, followed by a 5 min wash with 300-wash buffer. Tagmentation buffer (10 mM $MgCl_2$ in 300-wash buffer) was then added and incubated at 37 °C for 1 h. Finally, to stop the tagmentation, 40 mM EDTA with 0.05 U μl^{-1} RNase inhibitor was added and incubated at room

temperature for 5 min. The tissue was washed three times with 0.5× DPBS-RI for 5 min for further processing.

For the reverse transcription, two ligations and beads separation, the procedures were performed as described for those established in the spatial ARP-seq protocol. For constructing the CUT&Tag library, the supernatant was purified using Zymo DNA Clean & Concentrator-5 kit and eluted into 20 µl of RNase-free water. The PCR mix, consisting of 2 µl of 10 µM each of P5 PCR primer and indexed i7 primer along with 25 µl of NEBNext master mix, was added and thoroughly mixed. The PCR programme included an initial incubation at 58 °C for 5 min, 72 °C for 5 min and 98 °C for 30 s, followed by 12 cycles of 98 °C for 10 s and 60 °C for 10 s, with a final extension at 72 °C for 1 min. The PCR product was then purified using 1.3× Ampure XP beads according to the standard protocol and eluted in 20 µl of nuclease-free water. The construction of the cDNA libraries for mRNA and ADT was carried out according to the spatial ARP-seq protocol.

Before sequencing, the size distribution and concentration of the library were assessed using the Agilent Bioanalyzer High Sensitivity Chip. Subsequently, NGS was performed using the Illumina NovaSeq 6000 sequencer in paired-end 150 bp mode.

Quality control metrics for spatial ARP-seq and spatial CTRP-seq

For spatial ARP-seq, across all samples from mouse development, the LPC model and human brain V1 development, we observed a median of 11,635 unique fragments per pixel for ATAC modality. Among these, 19% were enriched at transcription start sites (TSS) and 18% were located in peaks (Supplementary Figs. 15a and 16a). For the RNA portion, a total of 23,824 genes were detected with an average of 1,230 genes and 2,392 unique molecular identifiers (UMIs) per pixel (Supplementary Fig. 16a). For the proteins, the average protein count per pixel was 59, and the protein UMI account per pixel was 394.

Spatial CTRP-seq for H3K27me3 was performed on 5 and 21 d.p.l. mouse brains. We obtained a median of 9,102 unique fragments per pixel, of which 10% of fragments overlapped with TSS regions, and 12% were located in peaks (Supplementary Figs. 15a and 16a). For the RNA data, a total of 23,397 genes was detected with an average of 1,318 genes per pixel and 2,392 UMIs per pixel (Supplementary Fig. 16a). For the proteins, the average protein count per pixel was 88, and the protein UMI counts per pixel was 793.

The insert size distributions of spatial ARP-seq and CTRP-seq (H3K27me3) fragments were consistent with the captured nucleosomal fragments in all tissues (Supplementary Fig. 15b). The correlation analysis between replicates showed high reproducibility (r = 0.99 for ATAC, r = 0.98 for RNA and r = 0.99 for protein in spatial ARP-seq; r = 0.98 for CUT&Tag (H3K27me3), r = 0.95 for RNA and r = 0.99 for protein in spatial CTRP-seq, where r is the Pearson correlation coefficient; Supplementary Fig. 16b,c).

Data preprocessing

For ATAC and RNA, as well as CUT&Tag and RNA data, linker 1 and linker 2 were used to filter read 2, and the sequences were converted to Cell Ranger ARC format (v.2.0.2, 10x Genomics). The genome sequences were in the newly formed read 1, barcodes A and barcodes B were included in newly formed read 2. The human reference (GRCh38) or mouse reference (GRCm38) genome was used to align the fastq files.

For protein data from ADTs, the raw FASTQ file of read 2 was reformatted in the same manner as for RNA. Using the default configurations of CITE-seq-Count v.1.4.2, we quantified the ADT UMI counts associated with each antibody at various spatial locations.

Data clustering and visualization

Initially, we determined the locations of pixels on the tissue sections from brightfield images using MATLAB 2020b. Subsequently, we generated spatial data files by using codes available at GitHub (https://github.com/di-0579/spatial_tri-omics).

Seurat (v.4.1)[92] was loaded in R (v.4.1) to construct Seurat objects for each sample using RNA matrices. Attribute information was then added to each object, and the objects were merged using the merge function. Pixel normalization, logarithmic transformation of counts and gene scaling were performed, followed by PCA, retaining the top 50 principal components. To reduce sample heterogeneity, the RunHarmony function was used for integration, and RunUMAP and FindClusters were applied to generate RNA clustering information. Finally, metadata were extracted to enable the spatial visualization of RNAcluster for each sample.

We used Library Signac (v.1.8)[93] in R (v.4.1) to read the ATAC data matrices. To integrate multiple datasets, functions from the GenomicRanges package were used to establish a common peak set. Fragment objects were then created for each sample, peaks were quantified across datasets and these quantified matrices were used to create a Seurat object for each dataset, with the Fragment object stored within each respective assay. The datasets were merged using the merge function. To minimize sample heterogeneity, we used FindIntegrationAnchors to identify integration anchors, using LSI embeddings for integration. Subsequently, we performed ATAC clustering and extracted metadata for spatial visualization of ATACcluster.

We used the SpatialGlue[94] package to integrate and cluster ATAC and RNA data, obtaining spatial domain information. The ArchR[95] package was used to load both ATAC and RNA data, incorporating the spatial domain information from SpatialGlue. This enabled us to identify differential RNA expression and the GAS across various regions. We used the addImputeWeights() function in ArchR to compute smoothing weights based on low-dimensional embeddings derived from the GeneExpressionMatrix within the ArchR project, which was selected for better spatial domain resolution. We then extracted RNA expression matrices, ATAC GAS expression matrices and CUT&Tag CSS expression matrices from ArchR objects for spatial gene visualization.

Spatiotemporal data analysis

To better identify the spatiotemporal patterns of gene regulation using our developed spatial multi-omics technology, we implemented a computational framework that consists of the following three main steps:

(1) Spatiotemporal regression model fitting

For each gene in RNA with expression in more than 2% of pixels across timepoints, we fit a negative binomial generalized additive model (NB-GAM) to account for the effects of library size, time and spatial location on gene expression levels and smooth terms were used to represent the effects of time and spatial location on gene expression, as well as their interaction[96]. Specifically, for the RNA counts Y_{gc} for a given gene g and pixel c with gene-specific means μgc and dispersion parameters ϕ_g, we have

$$Y_{gc} \sim NB(\mu_{gc}, \phi_g),$$

$$\log(\mu_{gc}) = \beta_{g0} + \beta_{g1} N_c + f_{g1}(tc) + f_{g2}(sc) + f_{g3}(tc, sc),$$

where ~ indicates 'distributed as', N indicates the sequencing depth; t_c indicates the timepoint information (P0, 2, 5, 7, 10, 21) of pixel c; s_c indicates the spatial location of pixel c. In the analysis of the CC, the spatial location was defined by manually dividing the CC region into ten bins after manually delineating the region. In the analysis of cortical layers, the spatial location was defined using the SpatialGlue results. For a given g, $f_{g1}()$ is a smooth function capturing temporal variations, $f_{g2}()$ is a smooth function capturing spatial variations and $f_{g3}()$ is a tensor product smooth function capturing the interaction between time and spatial location. We used the cubic regression spline as the marginal basis of the smooth function. The model is fitted using gam(), with ti() as the smooth function and family as nb() from R package mgcv.

For ATAC data, we first derived the gene score matrix by aggregating

the peak accessibility for peaks falling within a window ±50 kb of the TSS around each gene and expressed in more than 1% pixels across five timepoints, using the function getDORCScores() from R package FigR[97]. We smoothed the sparse gene score matrix per pixel per gene using its four nearest neighbours based on the first 50 principal components from RNA data, using the function smoothScoresNN(). We then fitted the GAM on the log-scaled smoothed gene score matrix with the Gaussian family.

This model enables us to identify genes with significant associations with either time, spatial location or their interaction. We determined the significance using Wald tests for the model coefficients and used the Benjamini–Hochberg procedure to adjust the *P* values. Genes with an adjusted *P* value of less than 0.01 in any of the spatial, time or time and spatial interaction terms were selected for further analysis.

(2) Gene spatiotemporal clustering

We performed a two-step procedure to group patterns of genes that show significant changes across time and space in either RNA or ATAC. First, we derived pixel-level estimates μ_{gc} from our statistical model and aggregated them by their respective timepoints and spatial location regions, calculating RNA and ATAC separately. These aggregated profiles were then scaled. Next, we concatenated the RNA and ATAC aggregated profiles and then performed hierarchical clustering using one minus Pearson correlation coefficient as the distance metric and Ward's minimum variance as a linkage method[98], with the number of clusters set as 20 in the analysis of the CC and set as 30 in the analysis of cortical layers. This procedure aims to jointly capture both ATAC and RNA patterns. The number of clusters was intentionally set higher to overestimate the number of clusters, enabling us to capture as many joint patterns of RNA and ATAC as possible.

As we observed that some patterns in RNA and ATAC are similar, we subsequently combined the clusters on the basis of their similarity in RNA and ATAC profiles, respectively. First, we aggregated the RNA and ATAC profiles by their gene clustering labels from the previous step. We then performed hierarchical clustering with a smaller number of clusters: 6 for RNA and 4 for ATAC in the CC analysis (integrated S1 and S2 data), and 15 for RNA and 10 for ATAC for S2 data, and 13 for RNA and 7 for ATAC for S1 data in the cortical layers analysis. The number of clusters was determined by assessing whether the main patterns belonged to separate clusters and by evaluating the interpretability of the results. For the previous overclustered results in the previous step, we assigned labels to represent their RNA and ATAC patterns. If clusters shared the same RNA and ATAC pattern labels, we combined these clusters. Each cluster is then labelled based on its RNA and ATAC pattern, for example, R1-A1 for a cluster where the RNA pattern belongs to R1 and the ATAC pattern belongs to A1. This step summarizes the RNA and ATAC patterns and improves the interpretability of each cluster. By characterizing genes with similar RNA and ATAC patterns separately, we can also jointly examine clusters with different RNA and ATAC patterns across space and time. For example, clusters labelled R1-A1 and R1-A3 share the same RNA pattern but have different ATAC patterns, while clusters labelled R1-A1 and R2-A1 share the same ATAC pattern but have different RNA patterns.

(3) GO enrichment analysis of gene spatiotemporal clustering

We performed GO enrichment analysis to further characterize the identified clusters, focusing on the orthogonal ontology of biological processes. The analysis was performed using the function enrichGO() from the R package clusterProfiler[99] with minGSSize set to 20 and maxGSSize set to 200.

CODEX data clustering

Whole-cell segmentation was performed with Cellpose[100] using the Cytoplasm model cyto. After obtaining the cell-level protein intensity matrix, we used Seurat v.4.1 to perform the subsequent analysis. For each sample, the data are first normalized using arcsinh transformation of the intensity matrix that scaled with a cofactor of 150 (ref. 101) and then scaled using ScaleData() and RunPCA() with all informative features. We removed the sample effect using the FindIntegrationAnchors() function, with reciprocal PCA (rpca) set as the dimensional reduction method to identify anchors and the first 20 principal components used as the dimensions. After integration, we performed clustering using the FindClusters() function on the neighbour graphs built based on the first 20 PCs, with the resolution set to 0.4. Each cluster was then manually annotated on the basis of their highly expressed markers.

Cell type and niche deconvolution

We performed cell2location (v.0.1.3)[102] to deconvolute the cell types of our spatial transcriptomics data using public references in Python v.3.9. We combined all samples in mouse development or in mouse LPC model together. We set the model 'cell2location.models.Cell2location()' with the expected average cell abundance as 5 and trained with full data with maximum epochs set as 30,000. The estimated cell abundance is based on the posterior mean using export_posterior().

To map cell types and spatial niches from MERFISH reference data[17] to our human visual cortex spatial transcriptomics data, we implemented Seurat's (v.4.3) label-transfer pipeline. For each developmental stage, we first identified transfer anchors using canonical correlation analysis on the top 30 principal components. We then transferred both cell type and spatial niche annotations from reference to query data using the TransferData() function. To ensure annotation reliability, pixels with maximum prediction scores below the 25th percentile threshold were excluded and isolated or sparsely distributed pixels were eliminated.

Selection of lesion-like compartments

To characterize microglial responses to demyelination in both primary lesion and distal regions, we implemented a stepwise strategy to identify spatially resolved lesion-like compartments. We first used cell2location-predicted cell type abundances, combined with spatial expression patterns of canonical microglial markers *Cx3cr1*, *P2ry12* and *Tmem119* across RNA and ATAC modalities, to define high-confidence microglia pixels. To remove random pixels not located in primary and distal regions, we applied a *k*-nearest neighbour (*k*-NN) filter, retaining core pixels of which the average distance to their five nearest neighbours was within the 85–90th percentile. Core regions were then expanded by including surrounding pixels within a 10–15-neighbour *k*-NN window (around 80–100 μm) to capture broader lesion-like compartment.

Multimodal clustering and differential analysis of lesion-like compartments

To further dissect the heterogeneity of microglia within primary and distal lesion-like compartments, we performed joint RNA and ATAC analysis using ArchR[95] for all the LPC samples. Dimensionality reduction was performed using iterative latent semantic indexing (LSI) separately on ATAC and RNA matrices. Harmony batch correction was applied to each modality using the sample identity as the grouping variable. We then integrated both modalities using the addCombinedDims() function to obtain a joint reduced embedding (LSI_Combined). UMAP visualization and clustering were performed on this combined space using a resolution of 1.0. The resulting multimodal clusters were visualized using cluster-specific UMAP plots and assigned labels LC1–LC5 for downstream interpretation. To identify marker genes for each subset (LC1–LC5), we applied getMarkerFeatures() to both the gene activity (GeneScoreMatrix) and RNA expression (GeneExpressionMatrix) using the Wilcoxon test. GO enrichment analysis was then performed on the cluster-specific marker genes to uncover functional distinctions across clusters. To compare protein-level differences across subsets, we applied the ArchR derived LC1–LC5 cluster labels to the ADT data.

Expression levels of selected markers were visualized using the DotPlot() function from Seurat, based on normalized ADT assay values.

Gene module scoring of lesion-like compartments

To assess microglia in primary lesion and distal compartments, we constructed gene modules based on two previously published studies[75,76] (Supplementary Table 12). We computed module scores independently for RNA and ATAC data using the addModuleScore() function in ArchR[95], applied to the GeneExpressionMatrix and GeneScoreMatrix, respectively. To enhance spatial coherence of gene module scores, we applied nearest-neighbour smoothing using the addImputeWeights() function, with weights computed from LSI embeddings derived from the corresponding GeneExpressionMatrix and GeneScoreMatrix. We then extracted RNA and ATAC module score matrices from ArchR objects for spatial visualization.

Subclustering of microglia and identification of differentially expressed genes

We selected microglial-specific pixels based on cell2location predictions, retaining only those in which microglia showed the highest abundance among all cell types. Using these microglial-specific pixels, we performed multimodal subclustering by applying low-dimensional embedding (LSI and Harmony) and clustering on the combined RNA–ATAC data. This approach identified three distinct subclusters (MC1, MC2 and MC3). Differential analysis between subclusters was performed for both RNA expression (GeneExpressionMatrix) and chromatin accessibility (GeneScoreMatrix) using the getMarkerFeatures() function in ArchR[95], with thresholds of FDR ≤ 0.1 and $\log_2$[FC] ≥ 0.1. Volcano plots were generated to visualize the $\log_2$ fold changes and statistical significance ($-\log_{10}$[FDR]) for each modality. Genes exhibiting significant differences in both RNA and ATAC were highlighted to support joint interpretation of transcriptional and epigenetic states across the microglia subtypes.

Cell–cell communication analysis using CellChat

To explore intercellular communication among microglial subclusters (MC1–MC3) and other surrounding cell types, we applied CellChat[103] to spatial RNA data from 5 d.p.l. and 10 d.p.l. samples. The analysis focused on SCT-normalized RNA expression values from lesion-like compartments. Each pixel was assigned a specific cell type identity based on cell2location predictions, with microglia pixels labelled as MC1–MC3 according to their respective subclusters. We constructed a spatial CellChat object (datatype = "spatial") with spatial filtering enabled (distance.use = TRUE, interaction.range = 250, scale.distance = 0.5, contact.dependent = TRUE). Communication probabilities were computed using the truncated mean method (10% trimming), and significant interactions were filtered using min.cells = 2 and adjusted $P < 0.05$. All significant interactions ($P < 0.05$) across cell types were visualized using netVisual_bubble(), highlighting signalling associated with MC1–MC3 microglia.

Ligand–receptor analysis using NICHES

We applied the NICHES[104] framework to lesion-like compartments at 10 d.p.l. using the ALRA-imputed expression matrix (alra_SCT) as input to denoise sparse spatial expression. NICHES was run with the CellToCellSpatial, CellToNeighborhood and NeighborhoodToCell modes enabled, using the FANTOM5 ligand–receptor database, cell annotation and a neighbourhood size of $k = 9$.

To analyse cell–cell signalling patterns based on the NeighborhoodToCell_SCT_9_alra assay (produced by NICHES), we performed unsupervised clustering including variable feature selection, scaling, PCA (100 components), neighbourhood graph construction and Louvain clustering (resolution = 0.5). A UMAP embedding was generated using the top 30 principal components. Cluster-specific ligand–receptor signatures were identified using FindAllMarkers with a minimum expression threshold (min.pct = 0.5) and log-transformed fold change threshold (logfc.threshold = 0.25). The top 10 and top 30 marker genes per cluster were ranked by average $\log_2$-transformed fold change and exported as CSV files. SpatialFeaturePlots were generated for all top marker genes across spatial coordinates to visualize the spatial distribution of key ligand–receptor signals.

Reporting summary

Further information on research design is available in the Nature Portfolio Reporting Summary linked to this article.

Data availability

All raw and processed data have been deposited in the Neuroscience Multi-omic Data Archive (NeMO; https://assets.nemoarchive.org/col-1w5kt2k), and the mouse subset is also deposited in the Gene Expression Omnibus under accession code GSE308623. These datasets are available as a web resource and can be browsed within the tissue spatial coordinates in our data portal (https://spatial-omics.yale.edu/), also accessible via Oligointernode (https://ki.se/en/research/research-areas-centres-and-networks/research-groups/goncalo-castelo-branco-group#tab-oligointernode-datasets-and-resources). CODEX data have been deposited at Zenodo[105] (https://zenodo.org/records/17121652). The resulting fastq files were aligned to the human reference genome (GRCh38) (https://hgdownload.soe.ucsc.edu/goldenPath/hg38/chromosomes/) or mouse reference genome (GRCm38) (https://hgdownload.soe.ucsc.edu/goldenPath/mm10/chromosomes/). Published data for integration and quality comparison are available online: Atlas of gene regulatory elements in adult mouse cerebrum (http://catlas.org/mousebrain/#!/downloads); atlas of the adolescent mouse brain (http://mousebrain.org/adolescent/downloads.html); developing mouse brain data (https://www.ncbi.nlm.nih.gov/geo/query/acc.cgi?acc=GSE110823); mouse brain (https://assets.nemoarchive.org/dat-qwqfftg); CNS inflammation (https://www.ncbi.nlm.nih.gov/geo/query/acc.cgi?acc=GSE130119); and atlas of adult mouse brain (https://assets.nemoarchive.org/dat-qg7n1b0)

Code availability

Code for sequencing data analysis is available at GitHub (https://github.com/di-0579/spatial_tri-omics) and archived at Zenodo[105] (https://zenodo.org/records/17121652).

89. Smith, A. J., Clutton, R. E., Lilley, E., Hansen, K. E. A. & Brattelid, T. PREPARE: guidelines for planning animal research and testing. *Lab. Anim.* **52**, 135–141 (2018).
90. Bankhead, P. et al. QuPath: open source software for digital pathology image analysis. *Sci. Rep.* **7**, 16878 (2017).
91. Schneider, C. A., Rasband, W. S. & Eliceiri, K. W. NIH Image to ImageJ: 25 years of image analysis. *Nat. Methods* **9**, 671–675 (2012).
92. Hao, Y. et al. Integrated analysis of multimodal single-cell data. *Cell* **184**, 3573–3587 (2021).
93. Stuart, T., Srivastava, A., Madad, S., Lareau, C. A. & Satija, R. Single-cell chromatin state analysis with Signac. *Nat. Methods* **18**, 1333–1341 (2021).
94. Long, Y. et al. Deciphering spatial domains from spatial multi-omics with SpatialGlue. *Nat. Methods* **21**, 1658–1667 (2024).
95. Granja, J. M. et al. ArchR is a scalable software package for integrative single-cell chromatin accessibility analysis. *Nat. Genet.* **53**, 403–411 (2021).
96. Wood, S. N. Low-rank scale-invariant tensor product smooths for generalized additive mixed models. *Biometrics* **62**, 1025–1036 (2006).
97. Kartha, V. K. et al. Functional inference of gene regulation using single-cell multi-omics. *Cell Genom.* **2**, 100166 (2022).
98. Murtagh, F. & Legendre, P. Ward's hierarchical agglomerative clustering method: which algorithms implement Ward's criterion? *J. Class.* **31**, 274–295 (2014).
99. Wu, T. et al. clusterProfiler 4.0: a universal enrichment tool for interpreting omics data. *Innovation* **2**, 100141 (2021).
100. Stringer, C., Wang, T., Michaelos, M. & Pachitariu, M. Cellpose: a generalist algorithm for cellular segmentation. *Nat. Methods* **18**, 100–106 (2021).
101. Hickey, J. W., Tan, Y., Nolan, G. P. & Goltsev, Y. Strategies for accurate cell type identification in CODEX multiplexed imaging data. *Front. Immunol.* **12**, 727626 (2021).
102. Kleshchevnikov, V. et al. Cell2location maps fine-grained cell types in spatial transcriptomics. *Nat. Biotechnol.* **40**, 661–671 (2022).

103. Jin, S., Plikus, M. V. & Nie, Q. CellChat for systematic analysis of cell–cell communication from single-cell transcriptomics. *Nat. Protoc.* **20**, 180–219 (2025).
104. Raredon, M. S. B. et al. Comprehensive visualization of cell-cell interactions in single-cell and spatial transcriptomics with NICHES. *Bioinformatics* **39**, btac775 (2023).
105. Zhang, D. et al. Data and code for 'Spatial dynamics of brain development and neuroinflammation'. *Zenodo* https://doi.org/10.5281/zenodo.17121449 (2025).

Acknowledgements We thank J. Hjerling-Leffler for discussions; the staff at the Yale Center for Research Computing for guidance and use of the research computing infrastructure; E. Agirre for her expert advice and guidance in the computation analysis; C. Zheng, N. Mahmud, J. Sundell, E. Parvisto, M. Averstad, C. Zullian and the staff at Comparative Medicine-Biomedicum for assistance with animal husbandry and care. The moulds for microfluidic devices were fabricated at the Yale University School of Engineering and Applied Science (SEAS) Nanofabrication Center. NGS was conducted at the Yale Center for Genome Analysis (YCGA) as well as the Yale Stem Cell Center Genomics Core Facility, which was supported by the Connecticut Regenerative Medicine Research Fund and the Li Ka Shing Foundation. Services provided by the Genomics Core of Yale Cooperative Center of Excellence in Hematology (U54DK106857) were used. Work in G.C.-B.'s research group was supported by the Swedish Research Council (grants 2019-01360 and Distinguished Professor grant 2023-00324), the European Union (Horizon Europe Research and Innovation Programme/ERC Advanced grant SingleMS, 101096064), the Swedish Cancer Society (Cancerfonden; 23 2945 Pj 01 H), Knut and Alice Wallenberg Foundation (grants 2019-0107 and 2019-0089 and Wallenberg Scholar grant 2023-0280), Swedish Brain Foundation (grant FO2023-0032), The Swedish Society for Medical Research (SSMF, grant JUB2019), the Göran Gustafsson Foundation for Research in Natural Sciences and Medicine and the Karolinska Institutet. L.A.R.R.-K. was supported by European Committee for Treatment and Research in Multiple Sclerosis (ECTRIMS) and National MS Society (NMSS, USA, TA-2305-41342). Y.D. was supported by Cancerfonden. This research was supported by Packard Fellowship for Science and Engineering (to R.F.), Yale Stem Cell Center Chen Innovation Award (to R.F.) and the US National Institutes of Health (NIH) (RF1MH128876, U54AG076043, U54AG079759, UG3CA257393, UH3CA257393, R01CA245313, U54CA274509 and RM1MH132648 to R.F.).

Author contributions Conceptualization: R.F., D.Z., G.C.-B. and L.A.R.R.-K. Methodology: D.Z. and L.A.R.R.-K. Experimental Investigation: D.Z. and L.A.R.R.-K. Model design: D.Z., L.AR.R.-K. and Y. Lin. Model development: Y. Lin and D.Z. Data analysis: D.Z., L.A.R.R.-K., Y. Lin, X.L., W.W., Lijun Wang, H.Z., S.B., C.M., G.C.-B. and R.F. Data interpretation: L.A.R.R.-K., D.Z., G.C.-B. and R.F. In vivo experimentation and mouse husbandry: L.A.R.R.-K.. Resources: L.A.R.R.-K., M.S., Li Wang, S.K., T.J.-B., Y.D., M.Z., P.K., S.W., X.L.C., F.G., D.W., H.X., Y. Liu, J.C., N.S., P.U. and A.K. Data browser: Y. Lin, DZ. and Lijun Wang. Original draft: D.Z., L.A.R.R.-K., G.C.-B. and R.F. All of the authors reviewed, edited and approved the manuscript.

Competing interests R.F. is a scientific founder and advisor of IsoPlexis, Singleron Biotechnologies and AtlasXomics. The interests of R.F. were reviewed and managed by Yale University Provost's Office in accordance with the University's conflict of interest policies. G.C.-B. is shareholder and board member of Nexus Epigenomics. The other authors declare no competing interests.

Additional information

Supplementary information The online version contains supplementary material available at https://doi.org/10.1038/s41586-025-09663-y.

Correspondence and requests for materials should be addressed to Gonçalo Castelo-Branco or Rong Fan.

Peer review information *Nature* thanks Ozgun Gokce and the other, anonymous, reviewer(s) for their contribution to the peer review of this work. Peer reviewer reports are available.

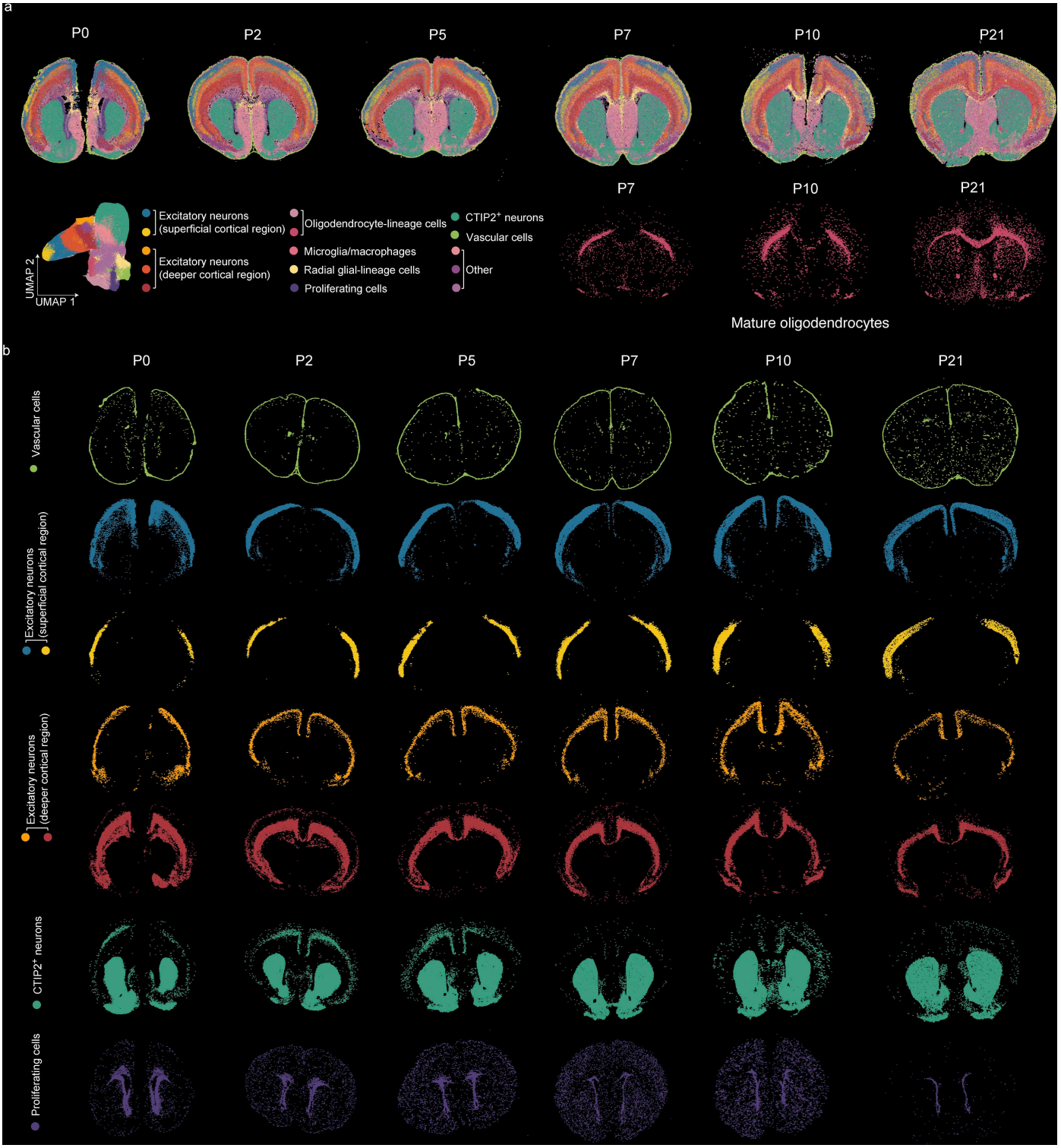

Extended Data Fig. 1 | Further data analysis of CODEX images for mouse brains. a, Seurat clustering of the CODEX images from P0 to P21. **b**, Spatial map of the cell types from **a**.

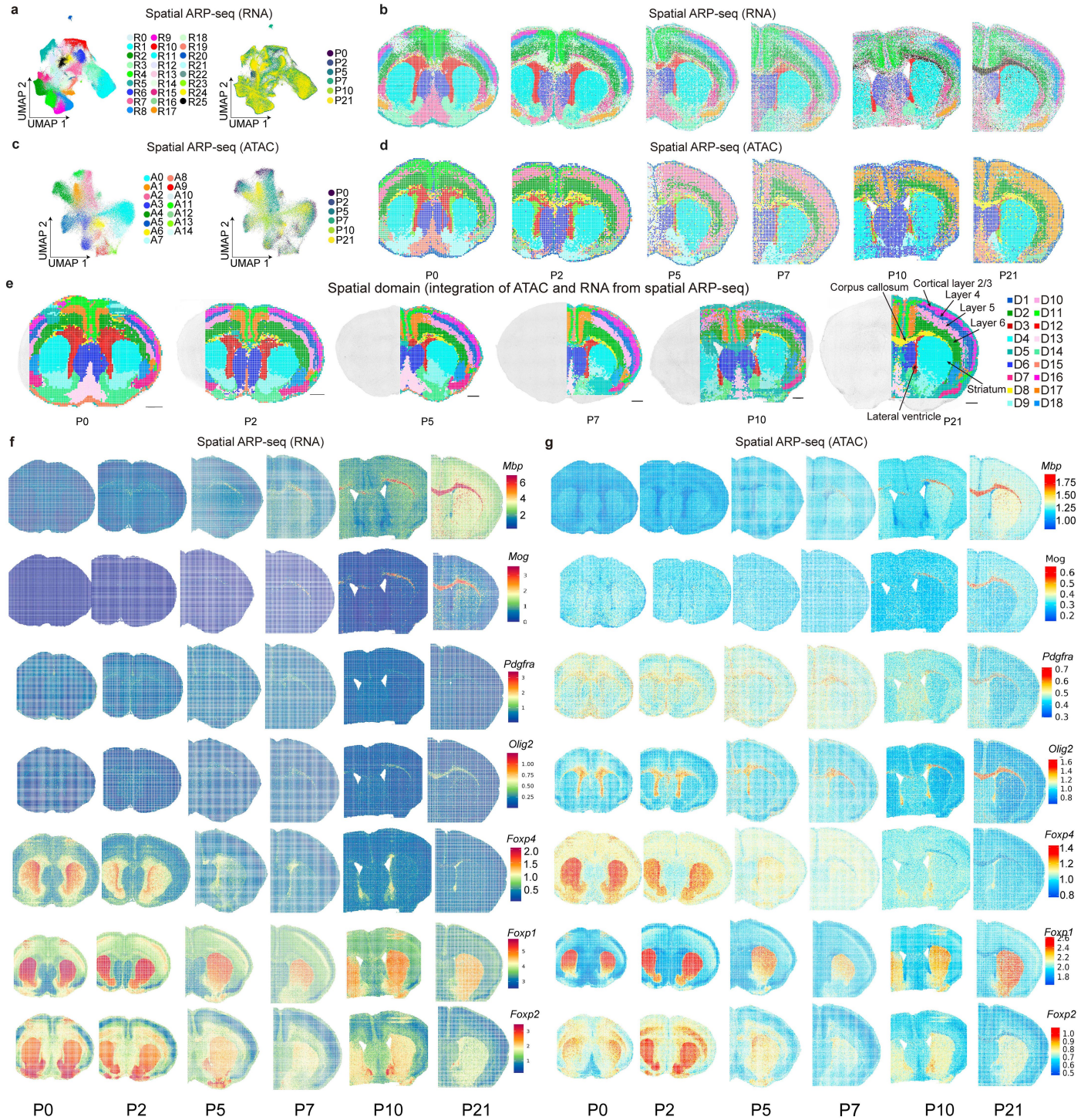

Extended Data Fig. 2 | Further analysis of spatial ARP-seq for postnatal mouse brains. a-b, UMAPs (**a**) and spatial distribution (**b**) of the mouse brain spatial RNA clusters at different stages from P0 to P21 (S2). **c-d**, UMAPs (**c**) and spatial distribution (**d**) of the mouse brain spatial ATAC clusters at different ages from P0 to P21 (S2, merged pixels (2×2 binning)). **e**, Spatial domain of the mouse brains generated by the integration of RNA and ATAC data in spatial ARP-seq (S2, merged pixels (2×2 binning)). Scale bar, 1 mm. **f-g**, Spatial mapping of gene expression (**f**) and ATAC GAS (**g**) of representative genes for RNA and ATAC in spatial ARP-seq.

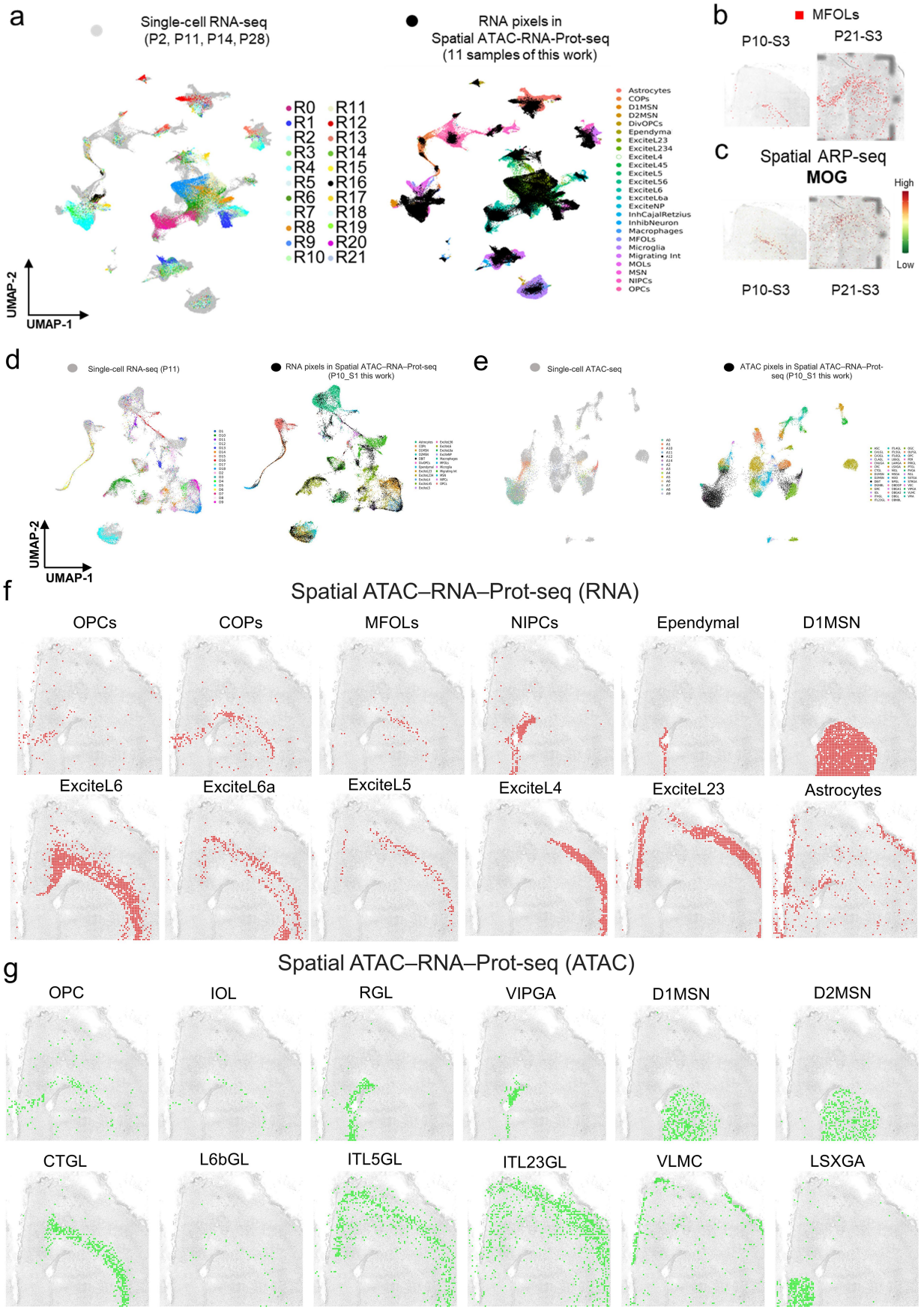

Extended Data Fig. 3 | See next page for caption.

Extended Data Fig. 3 | Further analysis of spatial ARP-seq for postnatal mouse brains. a, Integration of scRNA-seq[28–30] data from P2, P11, P14, and P28 mouse brains with our spatial RNA data in spatial ARP-seq (S1 + S3). **b**, Spatial mapping of MFOLs identified by label transfer from scRNA-seq to spatial RNA of P10 and P21 mouse brains. **c**, MOG expression in P10 and P21 mouse brain from the ADT protein data in spatial ARP-seq. **d**, Integration of P10 spatial RNA data and scRNA-seq data from mouse brain. **e**, Integration of P10 spatial ATAC data and scATAC-seq[31] data from mouse brain. **f**, Spatial mapping of cell types identified by label transfer from scRNA-seq to P10 spatial RNA data. **g**, Spatial mapping of cell types identified by label transfer from scATAC-seq[31] to P10 spatial ATAC data.

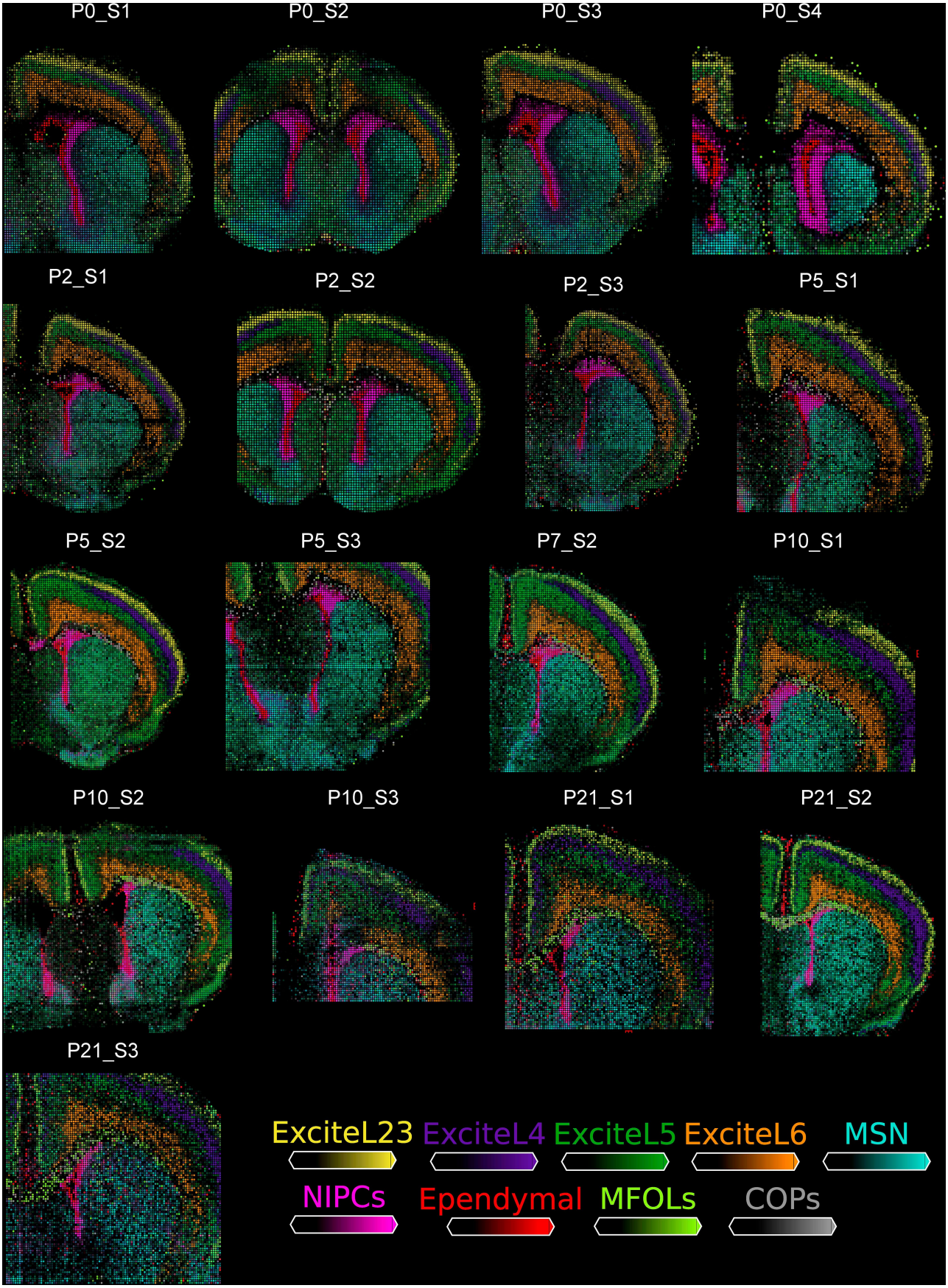

Extended Data Fig. 4 | Further analysis of spatial ARP-seq for postnatal mouse brains. Cell types[28–30] predicted by cell2location from all processed postnatal mouse brain samples.

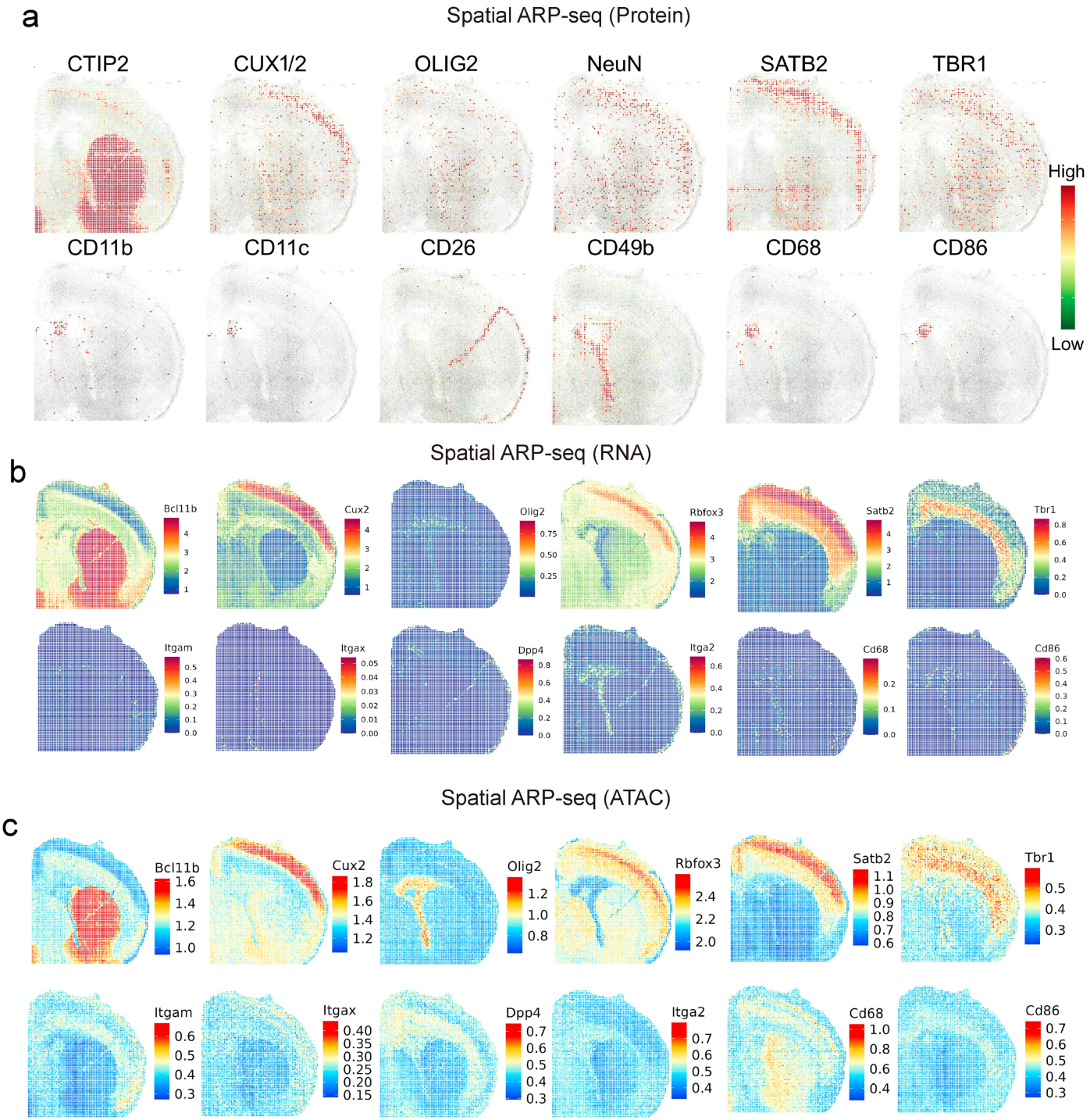

Extended Data Fig. 5 | Further analysis of spatial ARP-seq for postnatal mouse brains. a, Expression of selected ADT proteins in spatial ARP-seq from P0. **b-c**, Spatial mapping of gene expression (**b**) and ATAC GAS (**c**) for selected genes at P0.

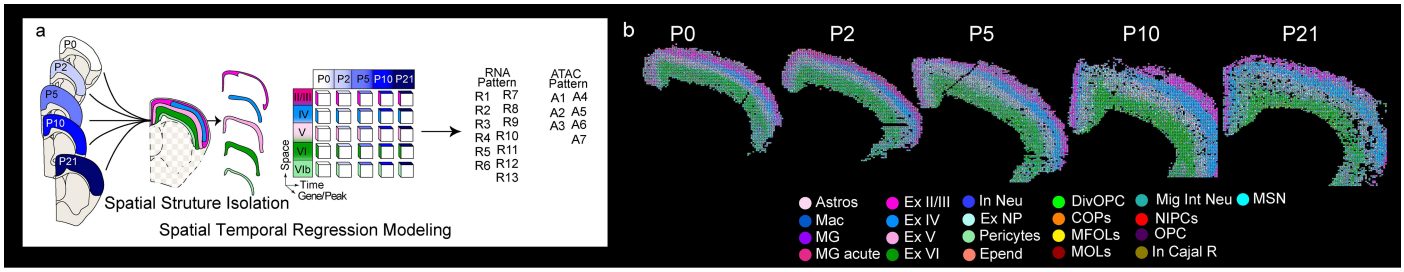

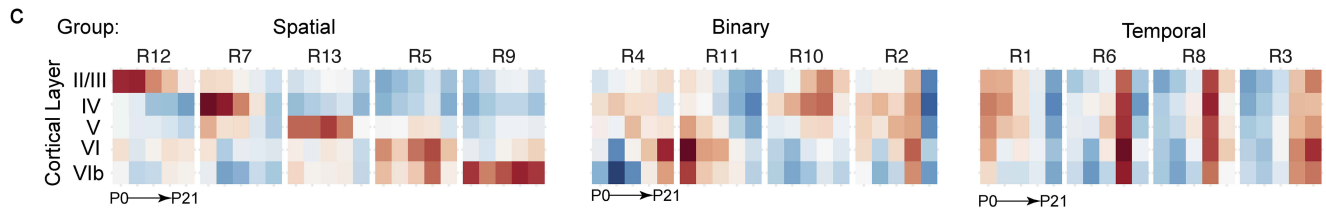

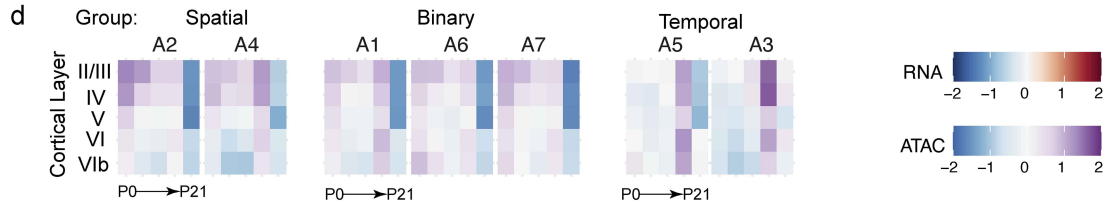

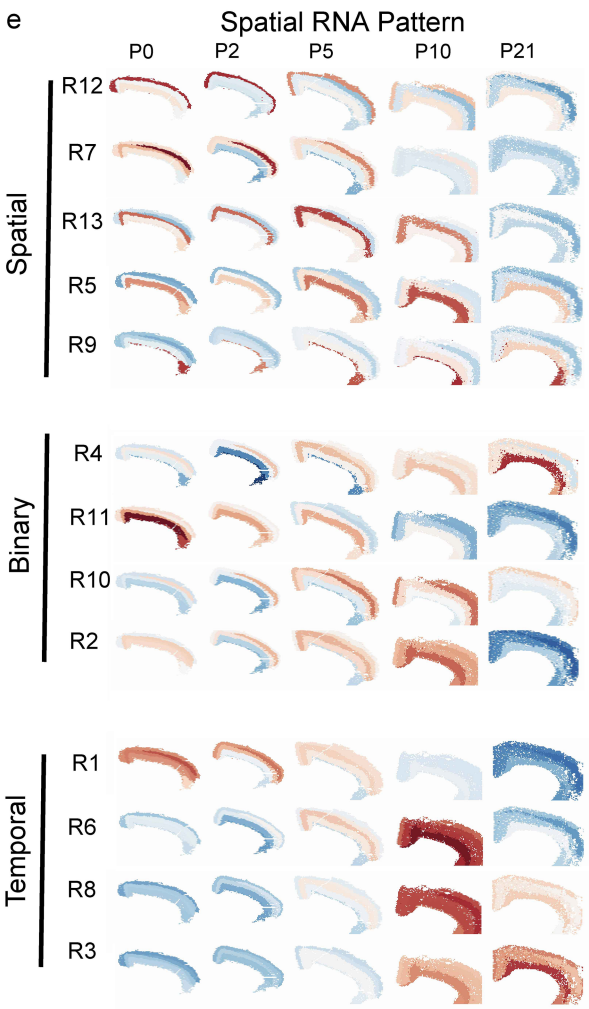

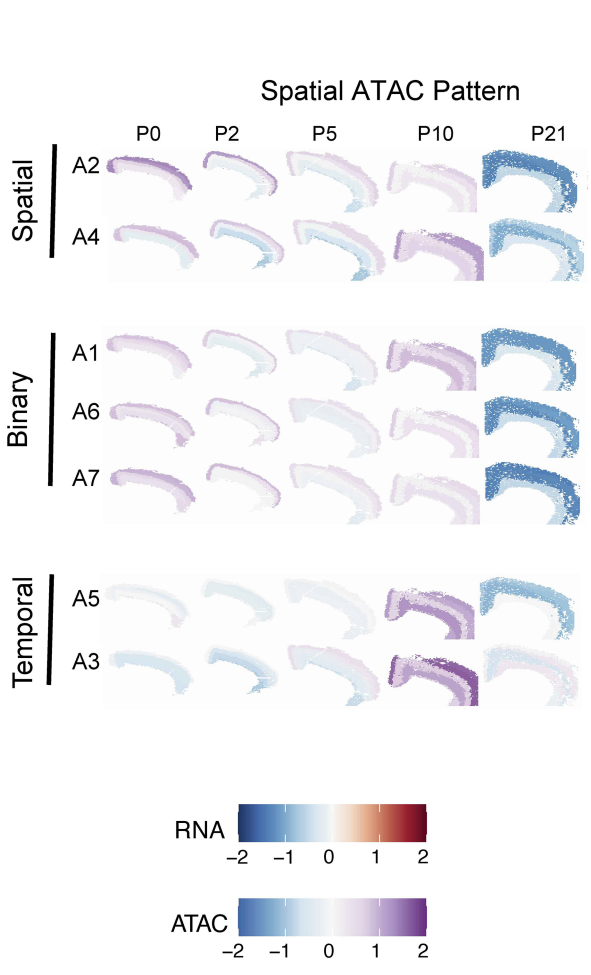

Extended Data Fig. 6 | Further analysis of developing mouse brain cortical layers. a, Schematic of the spatiotemporal regression model on mouse brain cortical layers. **b**, Different cell types in cortical layers (S1) from the spatial RNA data. **c**, Heatmaps of the 13 RNA clusters generated from the regression model (S1). **d**, Heatmaps of the 7 ATAC clusters generated from the regression model (S1). **e-f**, Spatial RNA (**e**) and ATAC (**f**) patterns generated from the regression model (S1).

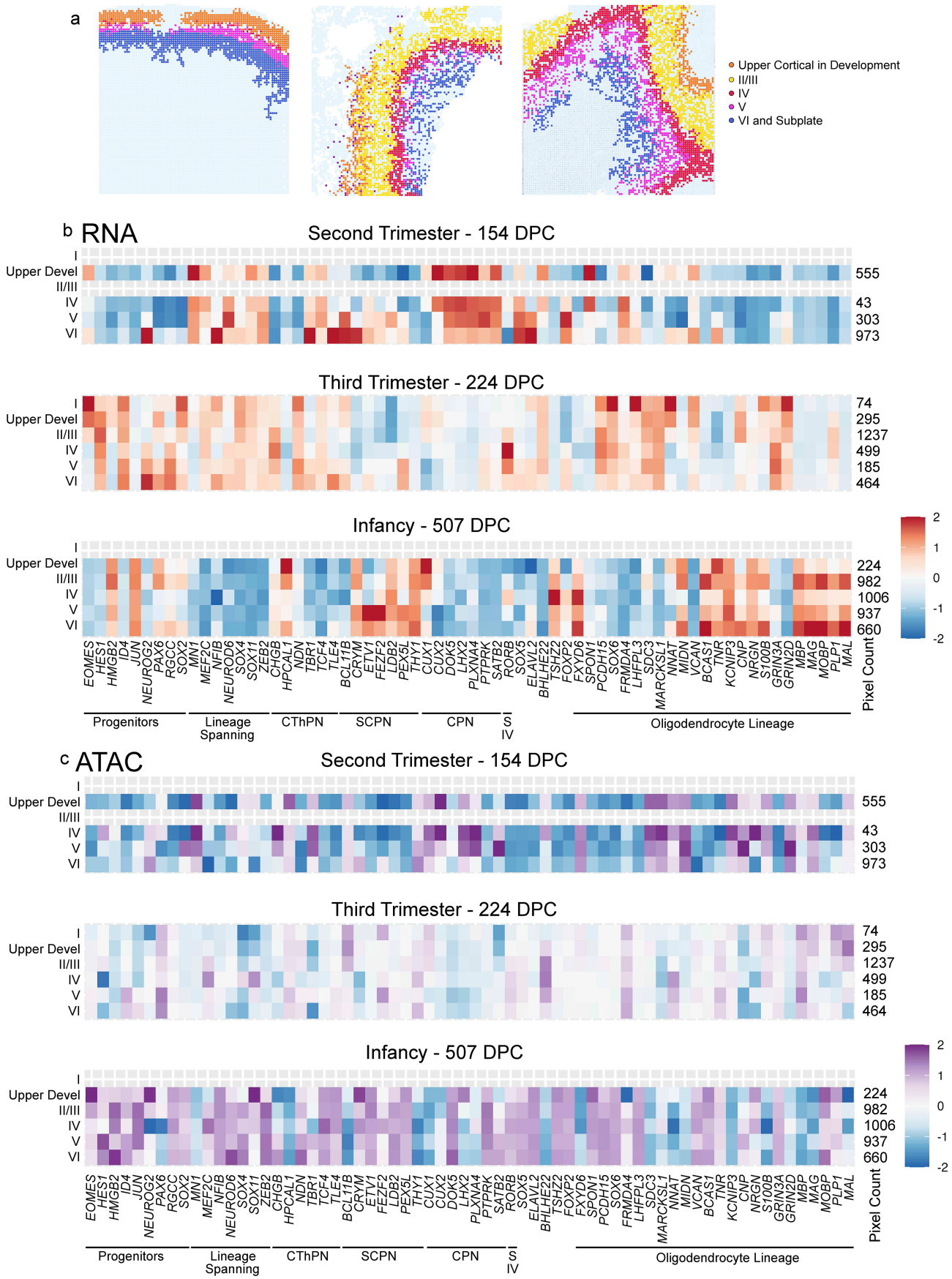

Extended Data Fig. 7 | Further analysis of developing human brain. a, Spatial deconvolution of developing human neocortex niches using MERFISH reference data[17]. **b-c**, Global heatmaps of RNA expression (**b**) and ATAC GAS (**c**) for all genes of focus. Upper Devel, cortical upper layer in development; S, stellate.

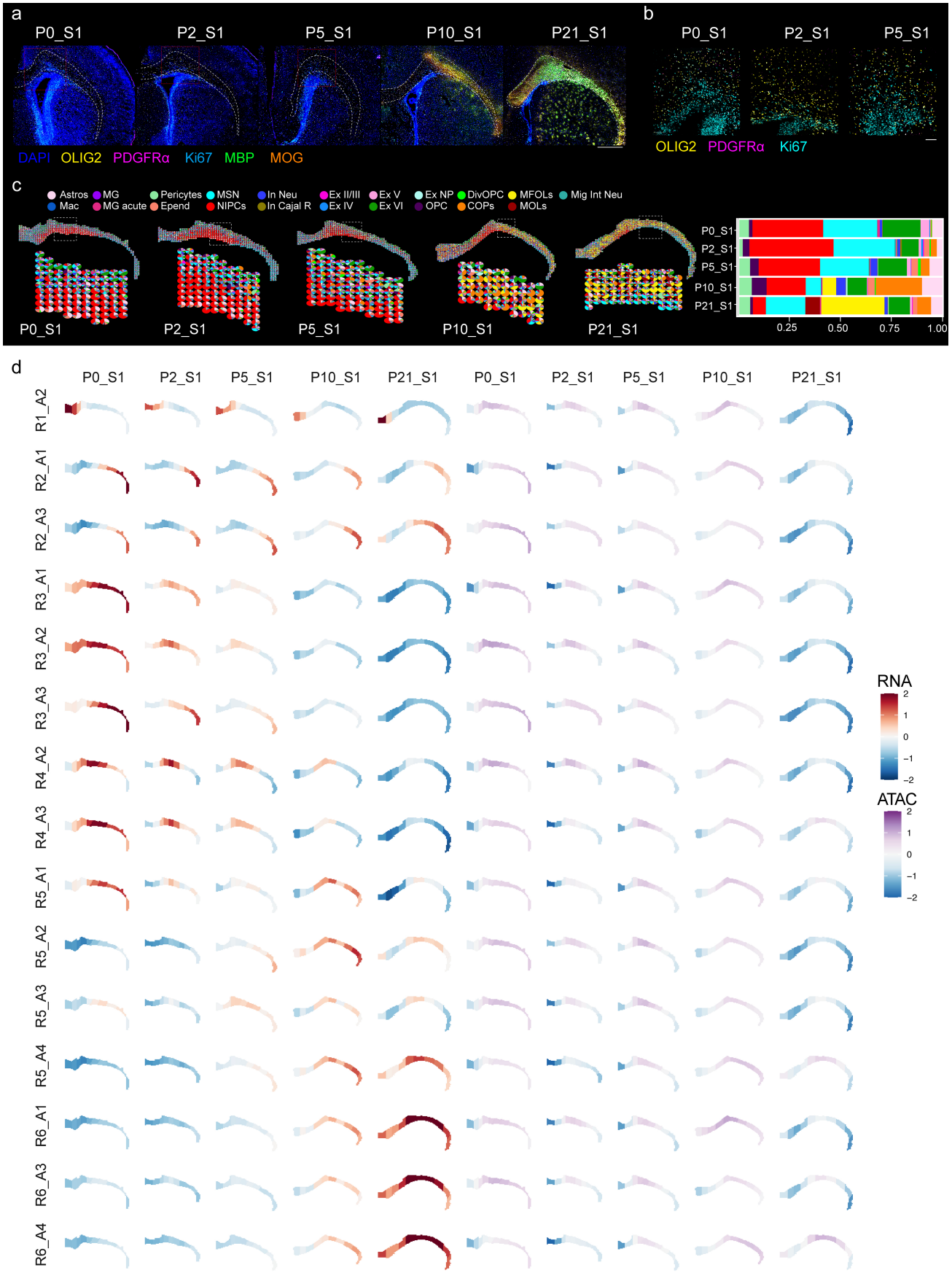

Extended Data Fig. 8 | Further analysis of developing mouse brain corpus callosum. a, CODEX images of the mouse brain corpus callosum from P0 to P21. Scale bar, 1 mm. **b**, Magnified images of the regions shown as the red dashed rectangles in **a** from P0-P5, respectively, with staining of OLIG2, PDGFRα, and Ki67. Scale bar, 800 μm. **c**, Different cell types in corpus callosum from the spatial RNA data. **d**, Spatial patterns of the 15 RNA & ATAC joint clustering.

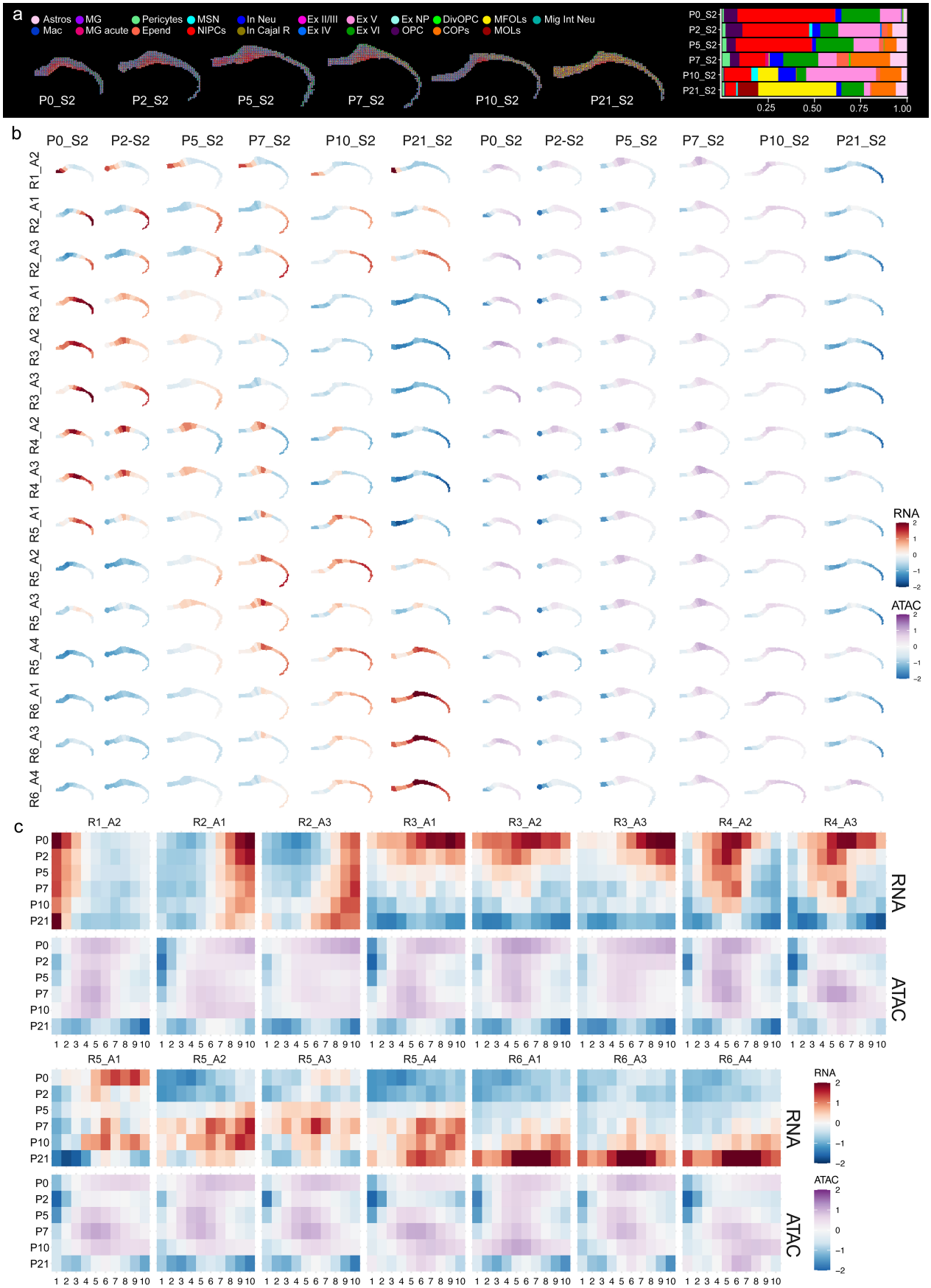

Extended Data Fig. 9 | Further analysis of developing mouse brain corpus callosum. a, Different cell types in corpus callosum from the spatial RNA data. **b**, Spatial patterns and heatmaps of the 15 RNA & ATAC joint clustering. **c**, Heatmaps of the 15 RNA & ATAC joint clustering from the regression model (S1 + S2).

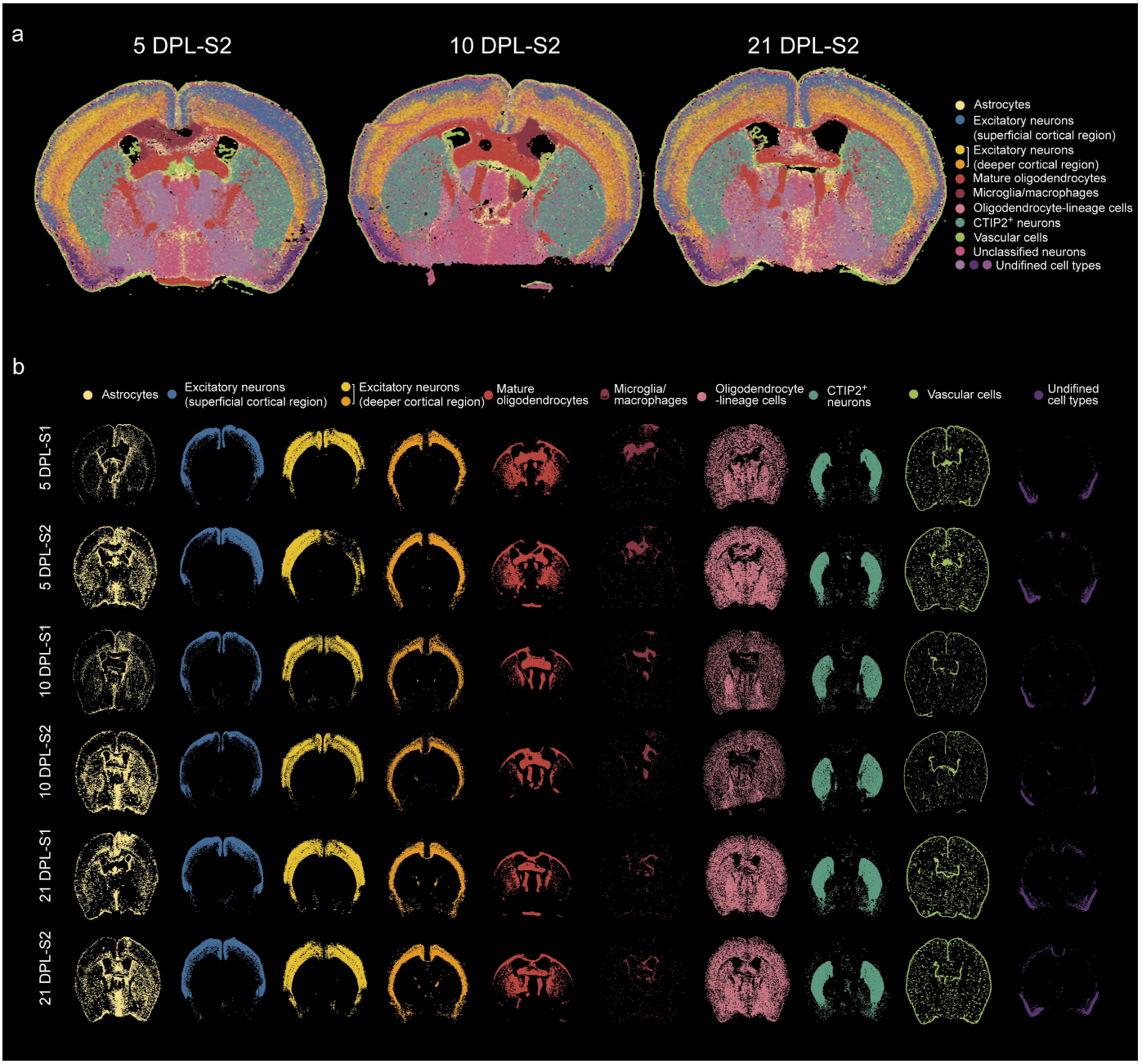

Extended Data Fig. 10 | Further analysis of CODEX images for LPC mouse brains. a, Seurat clustering of the CODEX images for replicates S2. **b**, Spatial map of the cell types from **a** and Fig. 4b.

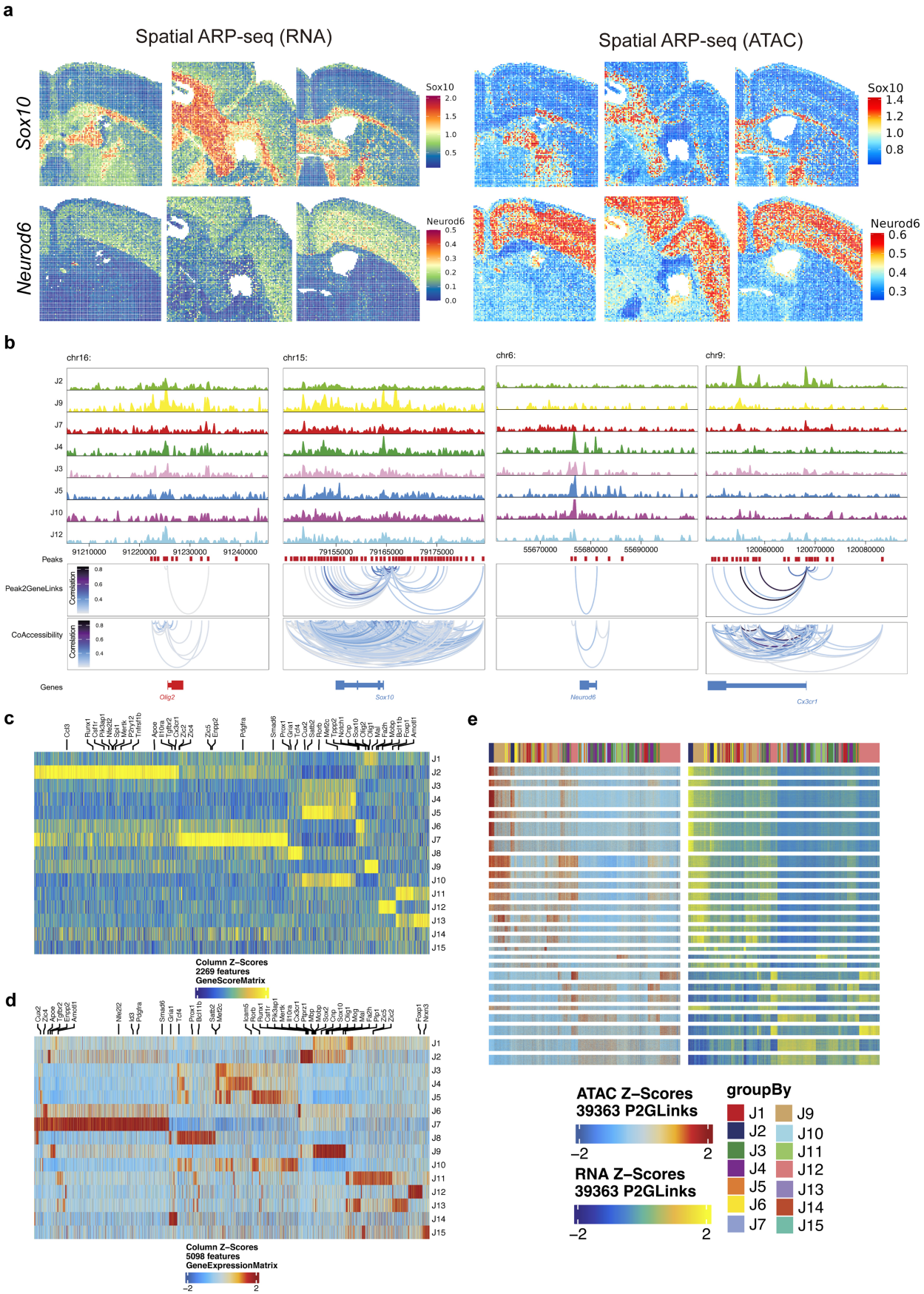

Extended Data Fig. 11 | See next page for caption.

Extended Data Fig. 11 | Further analysis of spatial ARP-seq for LPC mouse brains. a, Spatial mapping of gene expression (left) and ATAC GAS (right) for *Sox10* and *Neurod6*. **b**, Genome track visualization of marker genes with peak-to-gene links for distal regulatory elements and peak co-accessibility. **c**, Marker genes from each joint cluster in spatial ARP-seq in Fig. 4e. **d**, Marker GAS from each joint cluster in spatial ARP-seq in Fig. 4e. **e**, Heatmaps of peak-to-gene links in spatial ARP-seq in Fig. 4e.

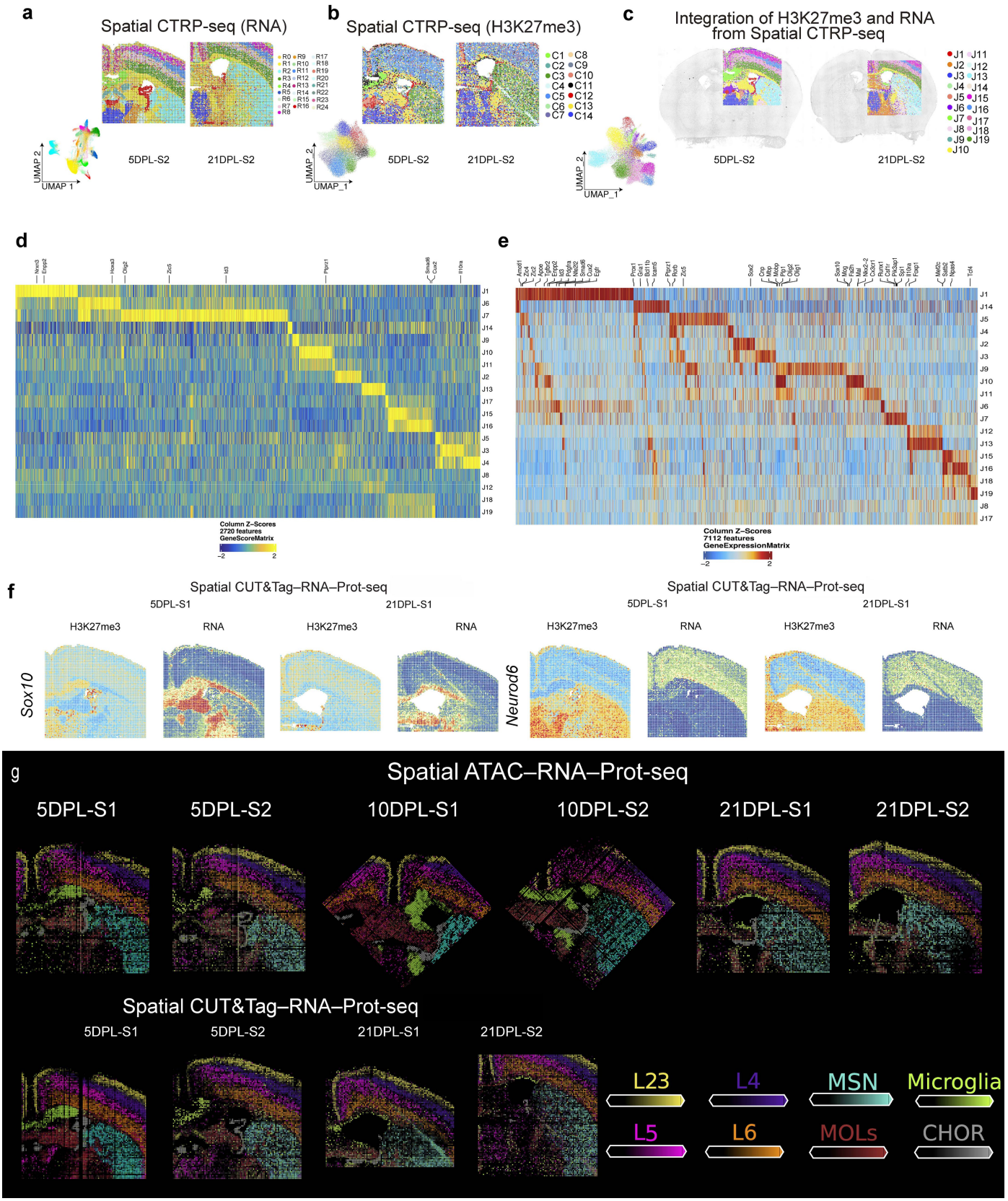

Extended Data Fig. 12 | Further analysis of spatial ARP-seq and spatial CTRP-seq (targeting H3K27me3) for LPC mouse brains. a-b, UMAPs and spatial distribution of RNA (**a**) and H3K27me3 (**b**) clusters in spatial CTRP-seq (S2). **c**, Integration of H3K27me3 and RNA data in spatial CTRP-seq (S2). **d**, Marker CSS from each joint cluster in spatial CTRP-seq in **c** and Fig. 4g. **e**, Marker gene expression from each joint cluster in spatial CTRP-seq in **c** and Fig. 4g. **f**, Spatial mapping of gene expression and CSS for *Sox10* and *Neurod6* in spatial CTRP-seq. **g**, Cell types[30,56] predicted by cell2location from all processed LPC mouse model brains in spatial ARP-seq and spatial CTRP-seq.

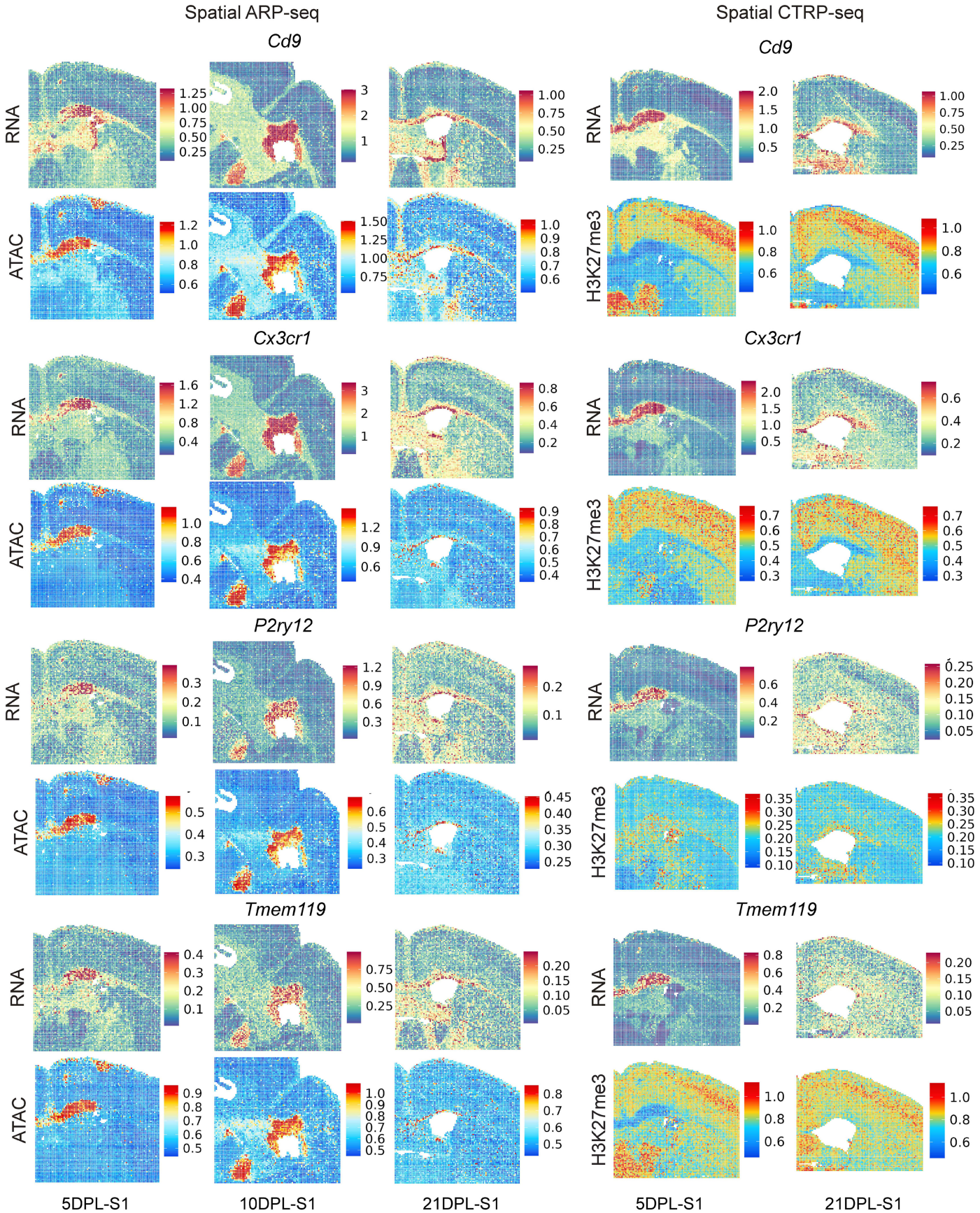

Extended Data Fig. 13 | Further analysis of spatial ARP-seq and spatial CTRP-seq (targeting H3K27me3) for LPC mouse brains. Spatial mapping of gene expression, GAS, and CSS for selected genes.

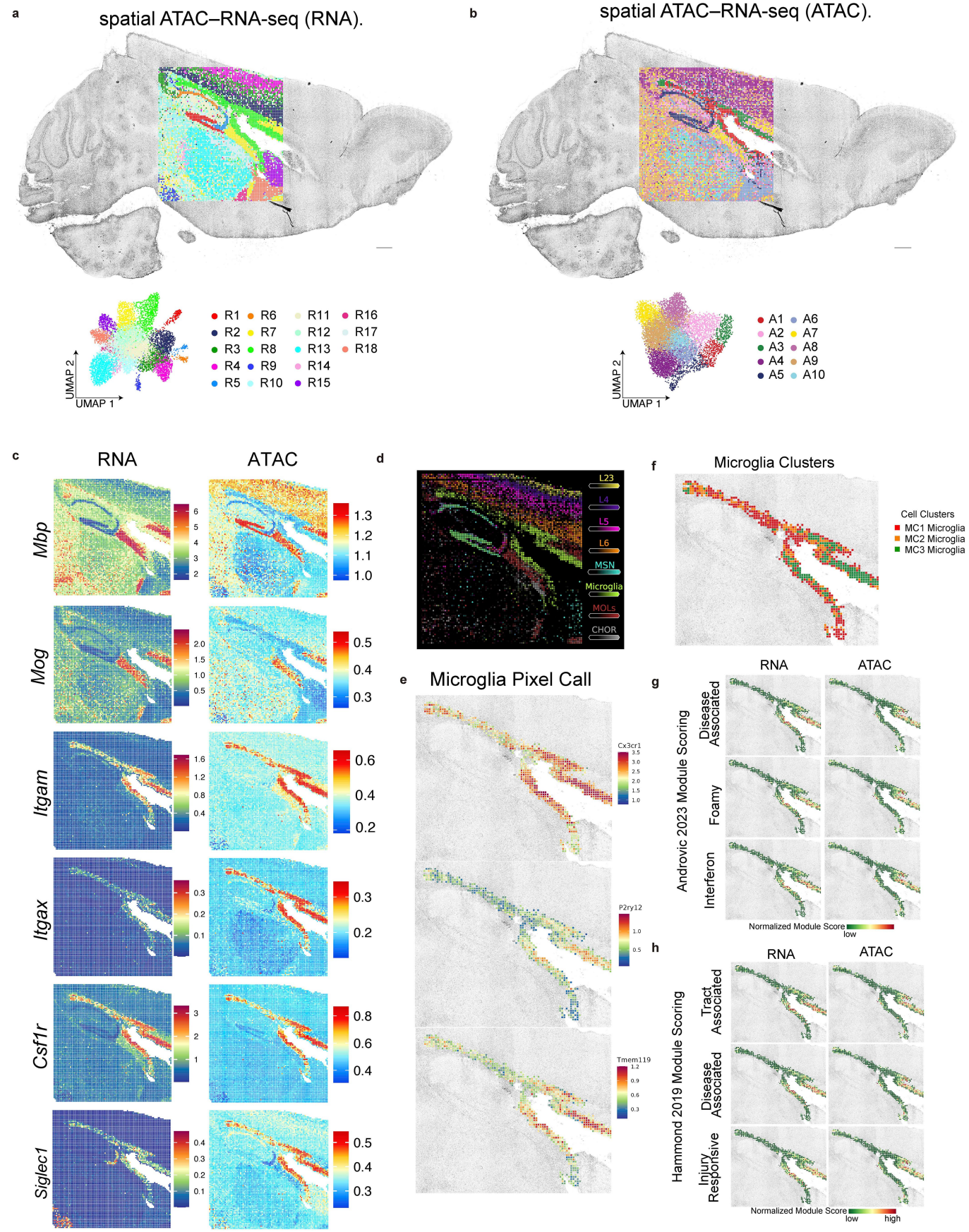

Extended Data Fig. 14 | See next page for caption.

Extended Data Fig. 14 | Further analysis for LPC mouse brains. a-b, UMAPs and spatial distribution of RNA (**a**) and ATAC (**b**) clusters from spatial ATAC–RNA-seq. **c**, Spatial mapping of gene expression and ATAC GAS for selected genes. **d**, Cell types[30,56] predicted by cell2location. **e**, Spatial mapping of gene expression for microglia-specific genes. **f**, Subclusters of microglia (MC1-MC3). **g**, Spatial module scores of disease-associated, foamy, and interferon microglial states based on RNA and ATAC data. Gene sets were based on a previous study[75]. **h**, Spatial module scores of disease-associated, tract-associated, and injury-responsive microglial states based on RNA and ATAC data. Gene sets were based on a previous study[76].

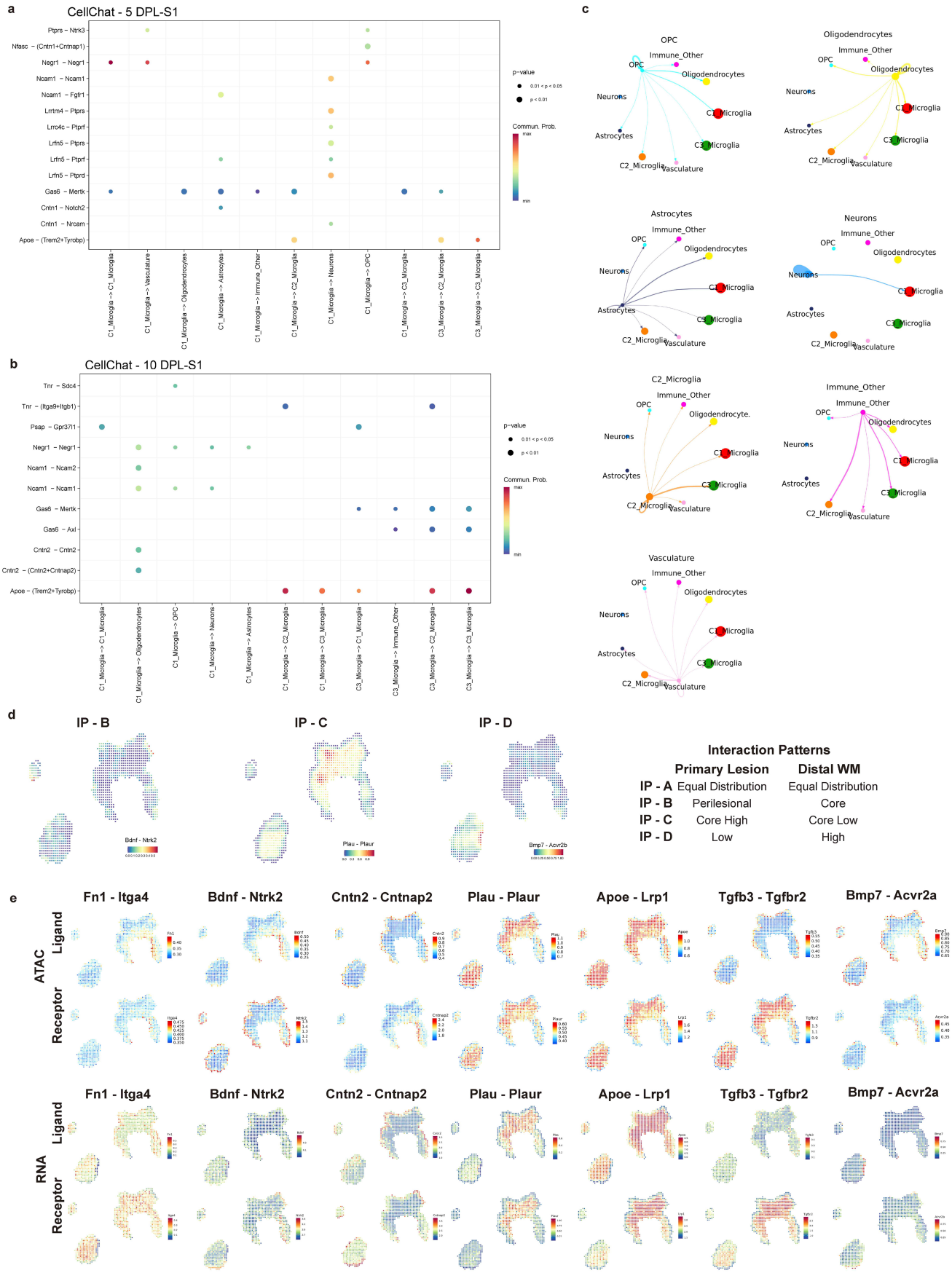

Extended Data Fig. 15 | See next page for caption.

Extended Data Fig. 15 | Further analysis for LPC mouse brains. a-b, CellChat dot plot showing representative ligand–receptor interactions among microglial subclusters (MC1–MC3) and other brain cell types at 5 DPL (**a**) and 10 DPL (**b**). Bubble colour represents communication probability, and bubble size indicates statistical significance ($p < 0.01$; $0.01 \leq p < 0.05$). Statistical significance was assessed using CellChat's built-in permutation test on communication probability (one-sided; alternative hypothesis: probability > 0). **c**, Communication networks of microglial subtypes and brain cell types, based on CellChat analysis. **d**, Representative spatial maps of ligand–receptor interaction showing regional enrichment within lesion-like compartments at 10 DPL. **e**, Spatial mapping of gene expression and ATAC GAS for the genes in **d** and Fig. 6m.

nature portfolio

Corresponding author(s): Rong Fan, Gonçalo Castelo-Branco

Last updated by author(s): Sep 19, 2025

Reporting Summary

Nature Portfolio wishes to improve the reproducibility of the work that we publish. This form provides structure for consistency and transparency in reporting. For further information on Nature Portfolio policies, see our Editorial Policies and the Editorial Policy Checklist.

Statistics

For all statistical analyses, confirm that the following items are present in the figure legend, table legend, main text, or Methods section.

n/a	Confirmed	
☐	☒	The exact sample size (*n*) for each experimental group/condition, given as a discrete number and unit of measurement
☐	☒	A statement on whether measurements were taken from distinct samples or whether the same sample was measured repeatedly
☐	☒	The statistical test(s) used AND whether they are one- or two-sided *Only common tests should be described solely by name; describe more complex techniques in the Methods section.*
☐	☒	A description of all covariates tested
☐	☒	A description of any assumptions or corrections, such as tests of normality and adjustment for multiple comparisons
☐	☒	A full description of the statistical parameters including central tendency (e.g. means) or other basic estimates (e.g. regression coefficient) AND variation (e.g. standard deviation) or associated estimates of uncertainty (e.g. confidence intervals)
☐	☒	For null hypothesis testing, the test statistic (e.g. *F*, *t*, *r*) with confidence intervals, effect sizes, degrees of freedom and *P* value noted *Give P values as exact values whenever suitable.*
☒	☐	For Bayesian analysis, information on the choice of priors and Markov chain Monte Carlo settings
☒	☐	For hierarchical and complex designs, identification of the appropriate level for tests and full reporting of outcomes
☐	☒	Estimates of effect sizes (e.g. Cohen's *d*, Pearson's *r*), indicating how they were calculated

Our web collection on statistics for biologists contains articles on many of the points above.

Software and code

Policy information about availability of computer code

Data collection	EVOS FL Auto 2 Software Revision 2.0.2094.0, Illumina NovaSeq 6000 System, Keyence BZ-X800 epifluorescence microscope, Akoya Biosciences PhenoCycler system
Data analysis	R 4.1, ArchR 1.0.1, Seurat 4.1, Cell Ranger ARC 2.0.2, Matlab 2020b, Signac 1.8, SpatialGlue 1.0, QuPath 0.5.1, FigR 1.0, clusterProfiler 4.0.5, cell2location 0.1.3 , mgcv_1.9 , Python 3.9, cellchat 2.1, NICHES 1.0.0, Cellpose 3.1 Scripts for data analysis were written in R and python with code available at Github (https://github.com/di-0579/spatial_tri-omics) and archived at Zenodo (https://zenodo.org/records/17121652)

For manuscripts utilizing custom algorithms or software that are central to the research but not yet described in published literature, software must be made available to editors and reviewers. We strongly encourage code deposition in a community repository (e.g. GitHub). See the Nature Portfolio guidelines for submitting code & software for further information.

Data

Policy information about availability of data

All manuscripts must include a data availability statement. This statement should provide the following information, where applicable:

- Accession codes, unique identifiers, or web links for publicly available datasets
- A description of any restrictions on data availability
- For clinical datasets or third party data, please ensure that the statement adheres to our policy

All raw and processed data have been deposited in the Neuroscience Multi-omic Data Archive (NeMO; https://assets.nemoarchive.org/col-1w5kt2k), and the mouse subset is also deposited in the Gene Expression Omnibus with accession code GSE308623. These datasets are available as a web resource and can be browsed within the tissue spatial coordinates in our own data portal: https://spatial-omics.yale.edu/.CODEX data have been deposited at Zenodo (https://zenodo.org/records/17121652).

The resulting fastq files were aligned to the human reference genome (GRCh38) (https://hgdownload.soe.ucsc.edu/goldenPath/hg38/chromosomes/) or mouse reference genome (GRCm38) (https://hgdownload.soe.ucsc.edu/goldenPath/mm10/chromosomes/). Published data for integration and quality comparison are available online: Atlas of gene regulatory elements in adult mouse cerebrum (http://catlas.org/mousebrain/#!/downloads); atlas of the adolescent mouse brain (http://mousebrain.org/adolescent/downloads.html); developing mouse brain data (https://www.ncbi.nlm.nih.gov/geo/query/acc.cgi?acc=GSE110823); mouse brain (https://assets.nemoarchive.org/dat-qwqfftg); CNS inflammation (https://www.ncbi.nlm.nih.gov/geo/query/acc.cgi?acc=GSE130119); and atlas of adult mouse brain (https://assets.nemoarchive.org/dat-qg7n1b0); FANTOM5 ligand–receptor database.

Research involving human participants, their data, or biological material

Policy information about studies with human participants or human data. See also policy information about sex, gender (identity/presentation), and sexual orientation and race, ethnicity and racism.

Reporting on sex and gender	Sex and gender were not used in any scenario as criteria for sample collection. All human samples are de-identified in this research.
Reporting on race, ethnicity, or other socially relevant groupings	No race, ethnicity, or other socially relevant groupings were performed in this study.
Population characteristics	We used de-identified tissue samples and no population characteristics other than age were used in this research.
Recruitment	De-identified tissue samples were collected with previous patient consent in strict observance of the legal and institutional ethical regulations. This was performed by the clinic and no recruitment criteria were used. This research don't take sex into consideration so the sex won't provide bias for this research.
Ethics oversight	Human Gamete, Embryo and Stem Cell Research Committee (Institutional Review Board) at the University of California, San Francisco; Institutional Review Board at the University of Maryland Brain & Tissue Bank

Note that full information on the approval of the study protocol must also be provided in the manuscript.

Field-specific reporting

Please select the one below that is the best fit for your research. If you are not sure, read the appropriate sections before making your selection.

☒ Life sciences ☐ Behavioural & social sciences ☐ Ecological, evolutionary & environmental sciences

For a reference copy of the document with all sections, see nature.com/documents/nr-reporting-summary-flat.pdf

Life sciences study design

All studies must disclose on these points even when the disclosure is negative.

Sample size	No directly relevant. No sample size calculation was performed. Samples sizes were chosen primarily based on experiment length, sample availability, and sequencing costs.
Data exclusions	No data were excluded from the study.
Replication	All attempts at replication were successful. At least two replicates have been done for each time point for developing and LPC mouse brains. Human tissue was processed once per stage.
Randomization	Randomization was performed to assign samples to time-point groups.
Blinding	Experimental blinding was implemented during retro-AAV-eGFP image analysis.

Reporting for specific materials, systems and methods

We require information from authors about some types of materials, experimental systems and methods used in many studies. Here, indicate whether each material, system or method listed is relevant to your study. If you are not sure if a list item applies to your research, read the appropriate section before selecting a response.

Materials & experimental systems

n/a	Involved in the study
☐	☒ Antibodies
☒	☐ Eukaryotic cell lines
☒	☐ Palaeontology and archaeology
☐	☒ Animals and other organisms
☒	☐ Clinical data
☒	☐ Dual use research of concern
☒	☐ Plants

Methods

n/a	Involved in the study
☒	☐ ChIP-seq
☒	☐ Flow cytometry
☒	☐ MRI-based neuroimaging

Antibodies

Antibodies used

Anti-H3K27me3 antibody (clone number: C36B11), 9733, Cell Signaling Technology;
Secondary antibody (Guinea Pig anti-Rabbit IgG (Heavy & Light Chain) Antibody), ABIN101961, Antibodies-Online;
Anti-PDGFRα antibody (clone number: EPR22059-270), ab234965, Abcam;
Anti-Olig2 antibody (clone number: EPR2673), ab220796, abcam;
Anti-APC antibody (clone number: EP701Y), ab239828, abcam;
Anti-Myelin Basic Protein antibody (clone number: EPR21188), ab230378, abcam;
Anti-Iba1 antibody (clone number: EPR16588) - BSA and Azide free, ab220815, abcam;
Anti-GFAP antibody (clone number: EPR1034Y) - BSA and Azide free, ab218309, abcam;
Anti-Ctip2 antibody (clone number: EPR23120-25) - BSA and Azide free, ab269367, abcam;
Anti-CUX1+CUX2 antibody (clone number: EPR26509-154) - BSA and Azide free, ab309140, abcam;
Anti-TBR1 antibody (clone number: EPR8138(2)) - BSA and Azide free, ab239000, abcam;
Anti-NeuN antibody (clone number: EPR12763) - BSA and Azide free, ab209898, abcam;
Anti-Myelin oligodendrocyte glycoprotein antibody (clone number: EPR22629-310) - BSA and Azide free, ab255266, abcam;
Anti-SATB2 antibody (clone number: EPNCIR130A) - BSA and Azide free, ab212177, abcam;
TotalSeq™-A Mouse Universal Cocktail, V1.0, AB_2910353 (BioLegend Cat. No. 199901);
TotalSeq™-A Human Universal Cocktail, V1.0, AB_2888692 (BioLegend Cat. No. 399907);
CD31 antibody (clone number: MEC13.3)–Akoya Biosciences, Cat# 4250001.
CD4 antibody (clone number: RM4-5)–Akoya Biosciences, Cat# 4250016.
CD8a antibody (clone number: 53-6.7)– Akoya Biosciences, Cat# 4250017
CD19 antibody (clone number: 6D5)–Akoya Biosciences, Cat# 4250014.
CD45R/B220 antibody (clone number: RA3-6B2)–Akoya Biosciences, Cat# 4450006.
CD11c antibody (clone number: N418) – Akoya Biosciences, Cat# 4550108.
Ki67 antibody (clone number: B56)–Akoya Biosciences, Cat# 4250019
CD11b antibody (clone number: M1/70)–Akoya Biosciences, Cat# 4450015
LY6G antibody (clone number: 1A8)– Akoya Biosciences, Cat# 4550110.
CD3 antibody (clone number: 17A2) —Akoya Biosciences, Cat# 4550109.
CD169 antibody (clone number: 3D6.112) –Akoya Biosciences, Cat# 4550100.

Validation

All antibodies used have been validated by the manufacturer.
Tri-Methyl-Histone H3 (Lys27) (C36B11) Rabbit mAb #9733, Cell Signaling Technology, citation: Nat Cancer 3(9):1071-1087 (2022); Nat Commun 13(1):5883 (2022); Cancer Discov 12(7):1760-1781 (2022), et al. Please refer to manufacturer's description: https://www.cellsignal.com/products/primary-antibodies/tri-methyl-histone-h3-lys27-c36b11-rabbit-mab/9733
Guinea Pig anti-Rabbit IgG (Heavy & Light Chain) Antibody - Preadsorbed, Antibodies-Online, According to the manufacturer's description: ABIN101961 is tested via ELISA to ensure that the titer against the antigen (Rb IgG) is above a certain threshold. We also test to make sure the titer against potentially cross-reactive human IgG, goat IgG, and mouse IgG is below a certain threshold. In addition, we test ABIN101961 against anti-guinea pig Serum, rabbit IgG, and rabbit serum in an immunoelectrophoresis assay. Please refer to manufacturer's description: https://www.antibodies-online.com/antibody/101961/Guinea+Pig+anti-Rabbit+IgG+Heavy++Light+Chain+antibody+-+Preadsorbed/
Anti-PDGFR alpha antibody [EPR22059-270] - BSA and Azide free, abcam. Please refer to manufacturer's description: https://www.abcam.com/en-us/products/primary-antibodies/pdgfr-alpha-antibody-epr22059-270-bsa-and-azide-free-ab234965
Anti-Olig2 antibody [EPR2673] - BSA and Azide free, abcam. Please refer to manufacturer's description: https://www.abcam.com/en-us/products/primary-antibodies/olig2-antibody-epr2673-bsa-and-azide-free-ab220796
Anti-APC antibody [EP701Y] - BSA and Azide free, abcam. Please refer to manufacturer's description: https://www.abcam.com/en-us/products/primary-antibodies/apc-antibody-ep701y-bsa-and-azide-free-ab239828
Anti-Myelin Basic Protein antibody [EPR21188] - BSA and Azide free, abcam. Please refer to manufacturer's description: https://www.abcam.com/en-us/products/primary-antibodies/myelin-basic-protein-antibody-epr21188-bsa-and-azide-free-ab230378
Anti-Iba1 antibody [EPR16588] - BSA and Azide free, abcam. Please refer to manufacturer's description: https://www.abcam.com/en-us/products/primary-antibodies/iba1-antibody-epr16588-bsa-and-azide-free-ab220815
Anti-GFAP antibody [EPR1034Y] - BSA and Azide free, abcam. Please refer to manufacturer's description: https://www.abcam.com/

en-us/products/primary-antibodies/gfap-antibody-epr1034y-bsa-and-azide-free-ab218309
Anti-Ctip2 antibody [EPR23120-25] - BSA and Azide free, abcam. Please refer to manufacturer's description: https://www.abcam.com/en-us/products/primary-antibodies/ctip2-antibody-epr23120-25-bsa-and-azide-free-ab269367
Anti-CUX1+CUX2 antibody [EPR26509-154] - BSA and Azide free, abcam. Please refer to manufacturer's description: https://www.abcam.com/en-us/products/primary-antibodies/cux1cux2-antibody-epr26509-154-bsa-and-azide-free-ab309140
Anti-TBR1 antibody [EPR8138(2)] - BSA and Azide free, abcam. Please refer to manufacturer's description: https://www.abcam.com/en-us/products/primary-antibodies/tbr1-antibody-epr81382-bsa-and-azide-free-ab239000
Anti-NeuN antibody [EPR12763] - BSA and Azide free, abcam. Please refer to manufacturer's description: https://www.abcam.com/en-us/products/primary-antibodies/neun-antibody-epr12763-bsa-and-azide-free-ab209898
Anti-Myelin oligodendrocyte glycoprotein antibody [EPR22629-310] - BSA and Azide free, abcam. Please refer to manufacturer's description: https://www.abcam.com/en-us/products/primary-antibodies/myelin-oligodendrocyte-glycoprotein-antibody-epr22629-310-bsa-and-azide-free-ab255266
Anti-SATB2 antibody [EPNCIR130A] - BSA and Azide free, abcam. Please refer to manufacturer's description: https://www.abcam.com/en-us/products/primary-antibodies/satb2-antibody-epncir130a-bsa-and-azide-free-ab212177
For all the abcam antibodies, the manufacturer's description is as follow: We have tested this species and application combination and it works. It is covered by our product promise.
CD31 antibody – Anti-Mu CD31(AKYP0002)-BX002—Atto 550 for PhenoCycler (Formerly CD31-BX002 (MEC13.3)—Atto 550-RX002), Akoya Biosciences, Cat# 4250001. Please refer to manufacturer's description : https://my.akoyabio.com/ccrz__ProductDetails?sku=4250001
CD4 antibody – Anti-Mu CD4(AKYP0041)-BX026—Atto 550 for PhenoCycler (Formerly CD4-BX026 (RM4-5)—Atto 550-RX026), Akoya Biosciences, Cat# 4250016. Please refer to manufacturer's description : https://my.akoyabio.com/ccrz__ProductDetails?sku=4250016
CD8a antibody – Anti-Mu CD8a(AKYP0044)-BX029—Atto 550 for PhenoCycler (Formerly CD8a-BX029 (53-6.7)—Atto 550-RX029), Akoya Biosciences, Cat# 4250017. Please refer to manufacturer's description : https://my.akoyabio.com/ccrz__ProductDetails?sku=4250017
CD19 antibody – Anti-Mu CD19(AKYP0033)-BX020—Atto 550 for PhenoCycler (Formerly CD19-BX020 (6D5)—Atto 550-RX020), Akoya Biosciences, Cat# 4250014. Please refer to manufacturer's description : https://my.akoyabio.com/ccrz__ProductDetails?sku=4250014
CD45R/B220 antibody – Anti-Mu CD45R/B220(AKYP0014)-BX010—Alexa Fluor™ 750 for PhenoCycler (Formerly CD45R/B220-BX010 (Ra3-6B2)—Alexa FluorTM 750-RX010), Akoya Biosciences, Cat# 4450006. Please refer to manufacturer's description : https://my.akoyabio.com/ccrz__ProductDetails?sku=4450006
CD11c antibody – Anti-Mu CD11c(AKYP0045)-BX030—Alexa Fluor™ 647 for PhenoCycler (Formerly CD11c-BX030(N418)—Alexa Fluor™ 647-RX030) (Replaces 4350013 CD11c-BX030 (N418)—Cy5-RX030), Akoya Biosciences, Cat# 4550108. Please refer to manufacturer's description : https://my.akoyabio.com/ccrz__ProductDetails?sku=4550108
Ki67 antibody – Anti-Hu/Mu Ki67(AKYP0052)-BX047—Atto 550 for PhenoCycler (Formerly Ki67-BX047 (B56)—Atto 550-RX047), Akoya Biosciences, Cat# 4250019. Please refer to manufacturer's description : https://my.akoyabio.com/ccrz__ProductDetails?sku=4250019
CD11b antibody – Anti-Mu CD11b(AKYP0040)-BX025—Alexa Fluor™ 750 for PhenoCycler (Formerly CD11b-BX025 (M1/70)—Alexa FluorTM 750-RX025), Akoya Biosciences, Cat# 4450015. Please refer to manufacturer's description : https://my.akoyabio.com/ccrz__ProductDetails?sku=4450015
LY6G antibody – Anti-Mu Ly6g(AKYP0039)-BX024—Alexa Fluor™ 647 for PhenoCycler (Formerly Ly6g-BX024(1A8)—Alexa Fluor™ 647-RX024) (Replaces 4350015 Ly6g-BX024(1A8)—Cy5-RX024), Akoya Biosciences, Cat# 4550110. Please refer to manufacturer's description : https://my.akoyabio.com/ccrz__ProductDetails?sku=4550110
CD3 antibody – Anti-Mu CD3(AKYP0035)-BX021—Alexa Fluor™ 647 for PhenoCycler (Formerly CD3-BX021(17A2)—Alexa Fluor™ 647-RX021) (Replaces 4350014 CD3-BX021(17A2)—Cy5-RX021), Akoya Biosciences, Cat# 4550109. Please refer to manufacturer's description : https://my.akoyabio.com/ccrz__ProductDetails?sku=4550109
CD169 antibody – Anti-Mu CD169(AKYP0015)-BX015—Alexa Fluor™ 647 for PhenoCycler (Formerly CD169-BX015(3D6.112)—Alexa Fluor™ 647-RX015) (Replaces 4350005 CD169-BX015(3D6.112)—Cy5-RX015), Akoya Biosciences, Cat# 4550100. Please refer to manufacturer's description : https://my.akoyabio.com/ccrz__ProductDetails?sku=4550100

Animals and other research organisms

Policy information about studies involving animals; ARRIVE guidelines recommended for reporting animal research, and Sex and Gender in Research

Laboratory animals	The present study followed some applicable aspects of the PREPARE planning guidelines checklist such as the formulation of the in vivo study, dialogue between scientists and the animal facility, and quality control of the in vivo components in the study. All animals were born, bred, and housed at Karolinska Institutet, Comparative Medicine Biomedicum animal facility (KMB). Mouse brain tissues (postnatal days P0, P2, P5, P7, P10, and P21) were obtained from a mouse line generated by crossing Sox10:Cre animals (The Jackson Laboratory mouse strain 025807) on a C57BL/6j genetic background with RCE:loxP (eGFP) animals (The Jackson Laboratory mouse strain 32037-JAX) on a C57BL/6xCD1 mixed genetic background. Females with a hemizygous Cre allele were mated with males lacking the Cre allele, while the reporter allele was kept in hemizygosity in both females and males. In the resulting Sox10:Cre-RCE:LoxP (eGFP) progeny the entire OL lineage was labelled with eGFP. None of the experimental animals in this study were subjected to previous procedures before enrollment in the study. All animals were free from mouse viral pathogens, ectoparasites endoparasites, and mouse bacteria pathogens. Mice were kept with the following light/dark cycle: dawn 6:00-7:00, daylight 7:00-18:00, dusk 18:00-19:00, night 19:00-6:00 and housing to a maximum number of 5 per cage in individually ventilated cages (IVC Sealsafe plus GM500, Tecniplast, Italy). General housing parameters such as relative humidity, temperature, and ventilation follow the European Convention for the Protection of Vertebrate Animals used for experimental and other scientific purposes treaty ETS 123, Strasbourg 18.03.1996/01.01.1991. Briefly, consistent relative air humidity of 55%±10, 22 °C and the air quality is controlled with the use of stand-alone air handling units supplemented with HEPA filtrated air. Monitoring of husbandry parameters is done using ScanClime® (Scanbur) units. Cages contained hardwood bedding (TAPVEI, Estonia), nesting material, shredded paper, gnawing sticks and card box shelter (Scanbur). The mice received a regular chow diet (CRM(P) SDS, United Kingdom and CRM(P), SAFE, Augy, France). Water was provided by using a water bottle, which was changed weekly. Cages were changed every other week. Cage changes were done in a laminar air-flow cabinet (NinoSafe MCCU mobile cage changing unit) provided with a HEPA H14 EN1822 filter (0.3 um particle size). Facility personnel wore dedicated scrubs, socks and shoes. Respiratory masks were used when working outside of the laminar air-flow cabinet. Both sexes were included in the study.

Wild animals	No wild animals were used in the study.
Reporting on sex	We don't take sex into consideration in this research. Animals of both sexes were used for experiments.
Field-collected samples	No field collected samples were used in the study.
Ethics oversight	All experimental procedures on animals were performed following the European directive 2010/63/EU, local Swedish directive L150/SJVFS/2019:9, Saknr L150, Karolinska Institutet complementary guidelines for procurement and use of laboratory animals, Dnr. 1937/03-640 and Karolinska Institutet Comparative Medicine veterinary guidelines and plans (version 2020/12/18). The procedures described were approved by the regional committee for ethical experiments on laboratory animals in Sweden (Stockholms Norra Djurförsöksetiska Nämnd, Lic. nr. 1995/2019 and 7029/2020).

Note that full information on the approval of the study protocol must also be provided in the manuscript.

Plants

Seed stocks	*Report on the source of all seed stocks or other plant material used. If applicable, state the seed stock centre and catalogue number. If plant specimens were collected from the field, describe the collection location, date and sampling procedures.*
Novel plant genotypes	*Describe the methods by which all novel plant genotypes were produced. This includes those generated by transgenic approaches, gene editing, chemical/radiation-based mutagenesis and hybridization. For transgenic lines, describe the transformation method, the number of independent lines analyzed and the generation upon which experiments were performed. For gene-edited lines, describe the editor used, the endogenous sequence targeted for editing, the targeting guide RNA sequence (if applicable) and how the editor was applied.*
Authentication	*Describe any authentication procedures for each seed stock used or novel genotype generated. Describe any experiments used to assess the effect of a mutation and, where applicable, how potential secondary effects (e.g. second site T-DNA insertions, mosiacism, off-target gene editing) were examined.*